SPARK CHAMBER ANALYSIS OF DI-KAON PRODUCTION NEAR THRESHOLD

by

DAVID CECIL MASON

A Thesis submitted for the Degree of

DOCTOR OF PHILOSOPHY

in the

UNIVERSITY OF LONDON

——oOo——

Department of Physics,
Imperial College,
London, S.W.7.

February, 1968.

ABSTRACT

An account is presented of an experiment performed to study the production of the ϕ meson in the reaction $\pi^- + p \rightarrow K^+ + K^- + n$ at beam momenta just above the ϕ threshold. The experiment was performed as part of a series of experiments designed to investigate the electron-positron decay mode of the isoscalar vector mesons.

A description of the apparatus and its performance, and of the techniques of analysis employed, is given. The detection of the three final state particles and the beam pion was achieved using an arrangement of scintillation counters, Cerenkov counters, and spark chambers. In the mode employed, the system was capable of a high K^+K^- effective mass resolution and a high collection efficiency. The system supplied enough information to allow the complete reconstruction of each event via geometry and kinematics analysis programmes.

The experimental distributions of the variables used to parametrize the events were compared with corresponding theoretical distributions generated by Monte Carlo methods according to a specific model. The experimental distributions were compiled from $\sim$ 250 events of the type $\pi^- p \rightarrow K^+K^- n$ having K^+K^- effective masses in the range 986-1050 MeV/c^2.

The analysis indicated that ϕ production dominated the K^+K^-n signal produced with K^+K^- masses in the mass region of the ϕ meson at the beam momenta considered. The results support the hypothesis of isotropic production and decay of the ϕ meson just above threshold, with a ϕ production cross-section proportional to the centre of mass final state momentum here.

Some discussion of the K^+K^- mass spectrum away from the ϕ mass region is also included.

CONTENTS

		Page
ABSTRACT		i
PREFACE		v
CHAPTER 1.	INTRODUCTION.	
1.1	The experiment as part of a series.	1
1.2	Theoretical motivations for a study of the leptonic decay modes of the neutral vector mesons.	2
1.3	Principles of the apparatus.	9
1.4	The need for an experiment to study ϕ production in π^-p interactions.	15
1.5	The ϕ meson.	18
1.6	Possible mechanisms for ϕ production in $\pi^-p \rightarrow \phi n$.	21
1.7	General outline of the ϕ production experiment.	23
CHAPTER 2.	THE BEAM.	
2.1	Design of the beam.	27
2.2	Calculation of beam parameters.	35
2.3	The momentum measurement - the hodoscope.	38
2.4	The momentum distribution in a hodoscope channel.	41
2.5	Shimming of bending magnet BM2.	41
2.6	Floating wire measurements.	44
2.7	Beam setting-up and performance.	48
2.8	Beam composition.	49
CHAPTER 3.	EXPERIMENTAL DESIGN AND PROCEDURE	
3.1	Principles of the event selection, and description of the apparatus involved.	53
3.2	The spark chamber arrangement, and the optical system.	60
3.3	Electronic event selection and photography - the neutron time of flight spectrum.	61
CHAPTER 4.	THE MONTE CARLO AND KINEMATIC FITTING PROGRAMMES	
4.1	The Monte Carlo programme.	65
4.2	Calculations involved in the Monte Carlo programme - experimental OKE events.	69
4.3	The kinematic fitting programme.	72
4.4	Testing the kinematics programme with the Monte Carlo programme.	77
4.5	Use of the Monte Carlo and kinematics programmes to simulate the experimental fits.	79

CHAPTER 5. THE RESPONSE OF THE APPARATUS.
5.1 Definition of parameters used. 82
5.2 The role played by the neutron counters in determining the response of the apparatus. 85
5.3 Examples of the Monte Carlo distributions. 94
5.4 Resolutions. 99

CHAPTER 6. MAINLY CONCERNING THE EXTRACTION OF DATA FROM THE PHOTOGRAPHS.
6.1 Scanning and measuring of the events. 101
6.2 Reconstruction and kinematic fitting of the events. 108
6.3 Ambiguous events. 115
6.4 Elimination of systematic errors. 117
6.5 Analysis of the fits obtained. 120
6.6 The non-K^+K^-n background, and its subtraction. 121
6.7 Constant factors in the cross-section calculations. 129

CHAPTER 7. THE RESULTS, AND A COMPARATIVE DISCUSSION.
7.1 Introduction. 140
7.2 Comparison of experimental and theoretical distributions. 143
7.3 Some other possibilities. 151
7.4 Estimation of the proportionality constant A from the yield curve. 154
7.5 The experimental p^* dependence of the ϕ production cross-section. 157
7.6 Comparison and discussion. 160
7.7 K^+K^- background analysis. 166

APPENDICES.
Appendix 1. The Momentum Distribution in a Hodoscope Channel. 173
Appendix 2. The Method of Least Squares. 182

ACKNOWLEDGEMENTS 188

REFERENCES 190

PREFACE

The experiment described in this thesis was performed at the Rutherford Laboratory proton synchrotron 'Nimrod' during 1966 by the Imperial College Spark Chamber/Counter Group in collaboration with a small team from the Rutherford Laboratory. The experiment naturally involved the work of many people, and, though I have tried to present a complete account of the experiment, I have dwelt mainly on those aspects of it with which I was most concerned. This explains the emphasis laid, in the thesis, on the design of the beam, the kinematic fitting programme, the scanning and measuring of the events, and the experimental analysis, and, on the other hand, the relatively brief consideration of the electronic logic system and the problems relating to it.

CHAPTER 1

INTRODUCTION

1.1 The experiment as part of a series

This thesis describes one experiment in a series of experiments carried out at the Rutherford Laboratory proton synchrotron 'Nimrod' by the Imperial College Counter Group and its collaborators, during the period 1963-1967. The series consisted primarily of a study of the electron-positron decay modes of the isoscalar vector mesons ω^0 and ϕ^0. It can be sub-divided as follows.

1. A study of the production of ω^0 mesons in the reaction $\pi^- + p \longrightarrow \omega^0 + n$ near threshold, and a measurement of the branching ratio $\omega^0 \longrightarrow e^+ + e^-$.

2.(a) A study of the reaction $\pi^- + p \longrightarrow K^+ + K^- + n$ near threshold, in order to investigate the production of ϕ^0 mesons in this energy region using a negative pion beam. ($\phi^0 \rightarrow K^+ + K^-$ is the dominant ϕ^0 decay channel).

(b) A measurement of the branching ratio $\phi^0 \rightarrow e^+ + e^-$ using ϕ^0 mesons produced in the reaction $\pi^- + p \rightarrow \phi^0 + n$.

This thesis describes the experiment listed as 2(a) above i.e. ϕ production in $\pi^- p$ interactions near threshold. Although the

experiment can be considered as a separate entity, and discussed outside the context of the series, the basic reason for doing the experiment was to obtain information necessary for the rest of the series, and the experimental procedure adopted was strongly biased towards this end. Therefore it is within the framework of the series that the experiment is treated here. In accordance with this way of thinking, the chief theoretical arguments motivating such a study of these rare leptonic decay modes, are set out in summary form below. Points of theoretical interest that the individual experiment might clarify are discussed later.

1.2 Theoretical motivations for a study of the leptonic decay modes of the neutral vector mesons

The chief theoretical motivations for investigation of the leptonic decay modes of the neutral vector mesons seem at present to be as follows (see also ref.(1)): (a) this study would provide a method of measuring the vector meson-photon coupling strength in the region of large time-like momentum transfer, so that present knowledge of the nucleon structure could be enlarged; (b) as far as the isoscalar vector mesons ω and ϕ are concerned a measurement of their coupling to the photon can be related to the subject of ω -ϕ mixing on the SU_3 symmetry scheme, and would allow a test of the various models proposed to represent the SU_3 symmetry-breaking interaction which causes the mixing; (c) such a study might provide

a valuable test of the validity of quantum electrodynamics;

(d) the study would also test the concept of A-parity.

(a) The suggestion by Yukawa in 1935 that mesons could account for nuclear forces implied the existence of a meson cloud around the proton that would extend out to a distance of about a mesonic Compton wavelength. Direct measurement of the meson charge radius by electron-proton scattering studies showed that the charge distributions were too narrow to be explained by the interaction of a single pion, however. This led to the proposal that the existence of hypothetical mesons whose mass was greater than that of the pion could provide an explanation of the observed structure, and soon afterwards the presently known vector mesons ρ , ω , ϕ were discovered. It has become popular[2] to try to explain the nucleon form factors in terms of the vector mesons with the same quantum numbers as the gamma ray. Figure 1.1 shows the proposed Feynman diagrams for electron(muon)-proton scattering and nucleon-antinucleon annihilation into lepton-antilepton pairs. Since isotopic spin is a good quantum number for the vector mesons, it is assumed that the isovector and isoscalar form factors can be expressed in terms of the isovector and isoscalar vector mesons. Thus it is assumed for example that the isoscalar form factor G_s is of the form:

Fig. 1.1.

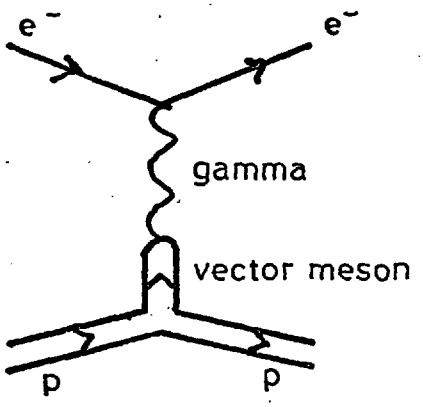

1). Electron - proton scattering

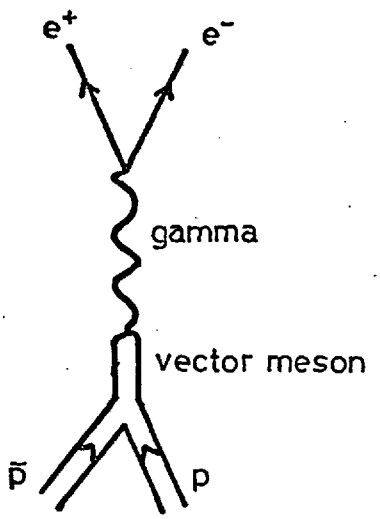

2). Nucleon - antinucleon annihilation

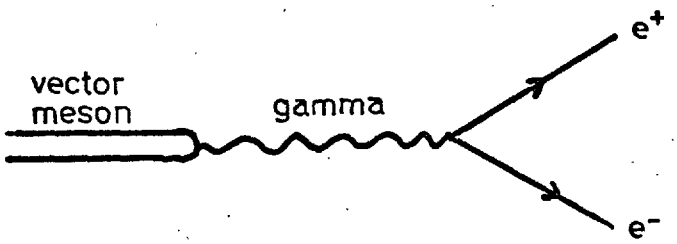

3). Leptonic decay of vector meson

$$G_s = \sum_i \frac{e}{2} \cdot \frac{g_{v_i nn}}{\gamma_{v_i}} \cdot \frac{M_i^2}{M_i^2 - q_i^2} \qquad \ldots. \; 1.1$$

Here M_i is the mass of the i-th isoscalar vector meson, $g_{v_i nn}$ is the coupling strength of this meson to the nucleons, and q_i^2 is its squared momentum transfer. In practice the behaviour of Gs can be described using just the known mesons ω and ϕ.(3) The constant γ_{v_i} is a measure of the coupling of the vector meson to the gamma ray. It can be determined by measuring the decay rate of the vector meson into lepton pairs. This occurs via a virtual photon (see Fig.1.1), i.e.

$$(V \rightarrow l^+ + l^-) = \frac{\alpha^2}{12} \cdot M_v \cdot \left| \frac{\gamma_v^2}{4\pi} \right|^{-1} \cdot \left| 1 + \text{order of} \left| \frac{M_l}{M_v} \right|^4 \right| \quad ..1.2$$

(α is the fine structure constant). This information would make it possible to determine the vector meson-nucleon coupling constants, by fitting equation 1.1 to the form factors known, say, from electron-proton scattering experiments. These coupling constants could then be compared with estimates from strong interaction experiments.

b) The concept of $\omega - \phi$ mixing in the SU_3 symmetry scheme was invoked to explain the apparent failure of the Gellman-Okubo mass formula to predict the mass of the I = 0 member of the vector meson octet.(4) This was predicted to lie at 930 MeV/c^2, 150 MeV/c^2 above the ω^o

mass, and 90 MeV/c^2 below the ϕ mass. This anomaly was explained by postulating that SU_3 was an exact symmetry only for the very strong interactions, and was broken by the so-called semi-strong interactions. The SU_3-breaking interaction was then supposed to cause a mixing of the $I = 0$ octet component (ψ_8, mass m_8) and the vector singlet state (ψ_1, mass m_1) to form the physical states ω and ϕ. These physical states were expressed as linear combinations of the octet and singlet states.

$$\begin{aligned} \omega &= \cos\theta . \psi_1 + \sin\theta . \psi_8 \\ \phi &= -\sin\theta . \psi_1 + \cos\theta . \psi_8 \end{aligned} \qquad \ldots 1.3$$

where θ was defined as the mixing angle. Dashen and Sharp[5] proposed that the mass operator in the $I = Y = 0$ subspace spanned by ψ_1, ψ_8 was given by a matrix of the form

$$\begin{vmatrix} \psi_8|M|\psi_8 & \psi_8|M|\psi_1 \\ \psi_1|M|\psi_8 & \psi_1|M|\psi_1 \end{vmatrix} \qquad \ldots 1.4$$

They attributed the failure of the Okubo mass formula to its taking into account only the diagonal elements of this mass matrix. They then assumed the diagonal element $\psi_8|M|\psi_8$ gave the mass predicted by the Okubo mass formula for the $I = 0$ octet member; using this, and the physical masses of ϕ and ω, they obtained a value of $+40^\circ$ for the mixing angle.

An experimental check of this result was possible by making an independent determination of the octet and singlet parts of the physical particles. This was possible because the photon cannot couple directly to the singlet state, whereas it is allowed to couple to the octet state. On the Dashen-Sharp scheme, the state ψ_8 was supposed coupled to the conserved hypercharge current with strength f_y ; the photon was coupled to this current with strength $\frac{e}{2}$. The coupling of ω and ϕ to the photon could then be represented as

$$\gamma_\omega = -\sin\theta . f_y . \frac{e}{2} . m_\omega^{\ 2} \quad ; \quad \gamma_\phi = -\cos\theta . f_y . \frac{e}{2} . m_\phi^{\ 2} \quad \ldots 1.5$$

Determination of $\Gamma(\omega \rightarrow 1^+ + 1^-)$ and $\Gamma(\phi \rightarrow 1^+ + 1^-)$ would therefore give a value for θ and f_y (see equation 1.2), and thus allow a test of the model used to represent the symmetry-breaking interaction.

This model is not unique, and several authors have proposed others.[6][7] These models seem to fall into two types. The first type assumes the SU_3 symmetry-breaking effects are due to non-zero off-diagonal matrix elements in the 'bare' mass matrix M_o between ψ_1 and ψ_8, and is called a 'mass-mixing' model[7] (e.g. the Dashen-Sharp model). The second type assumes the bare mass matrix M_o is diagonal, but the SU_3 symmetry is broken by certain current operator terms. This type has been called a 'current-mixing' model.[7]

The important point is that the validity of each model can be tested by a measurement of the above decay widths. The higher symmetries which evolved from SU_3 (SU(6), U(12)), went further than SU_3, and were able to predict a value for θ without invoking any model. Such a measurement would also test these theories.

(c) Investigation of these leptonic decay modes might also give valuable information about the limits of validity of present-day quantum electrodynamics and/or the possible non-electromagnetic structure of the muon.[8,2] Quantum electrodynamics regards the electron and muon as being identical in their interactions, the only difference between them being one of mass. These leptonic decays occur in the region of large time-like momentum transfer, which makes them especially valuable since they test the theory at small distances, where deviations from the theory seem most likely, and where relatively few corroborative experiments have been performed. If the electron and muon are treated as Dirac particles, we get from equation 1.2

$$R_V = \frac{(V \rightarrow \mu^+ + \mu^-)}{(V \rightarrow e^+ + e^-)} \approx 1 \qquad \ldots 1.6$$

the small difference from unity being due to the additional phase space for the electron decay. This assumes the vertices γee and $\gamma\mu\mu$ have identical properties at c.m.s. lepton energies $\sim m_V$.

However, if, for example, the muon were to have some anomalous interaction, the ratio R_v might be very different from unity.[9]

(d) The measurement would also be expected to throw light on the concept of A-parity, formulated by Bronzan and Low[10] in 1963 to explain some anomalies in boson interactions, in particular the long π^0 lifetime, the η branching ratios, and the low rate of $\phi \longrightarrow \rho + \pi$. They suggested a multiplicative quantum number, 'A-parity' non-conservation of which would reduce a transition rate by a factor of ~100. Unambiguous assignments of A to π , η , (-) and to γ , ρ , ϕ (+) could be made on the basis of observed rates. The relatively fast $\omega \rightarrow 3\pi$, 8 MeV partial width, implied A = -1 for the ω. This would inhibit by a factor of about 100, the $\omega\gamma$ vertex, but allow the $\phi\gamma$ vertex, thus suppressing the leptonic decay mode of the ω relative to that of the ϕ.

1.3 Principles of the apparatus

(For a more detailed account of this topic, see Ref.(11)).

The reaction studied in our experiments[12,13] is

$$\pi^- + p \longrightarrow z^0 + n \qquad \ldots 1.7$$

Here z^0 describes a particle, or system of particles, having a nett charge (Q), baryon number (B) and strangeness (S) of zero, and with allowed values of total isospin of 0, 1, 2. Since Q = S = B = 0, the z^0 system also has observable eigenvalues of the charge conjugation (C) and G-parity operators.

In our experiments, negative pions of known momentum and direction are allowed to interact in a hydrogen target. Neutrons produced in the above reaction are detected by neutron counters placed downstream of the hydrogen target (see Figure 1.2). Anti--coincidence counters placed in front of the neutron counters veto charged particle triggers. The time of flight of the neutron between the target and the neutron counter it entered is measured, thus giving the momentum of the neutron; the direction of the neutron is also measured, this being fixed within certain limits by the dimensions and position of the neutron counter concerned.

The effective mass of the z^0 system is given by

$$M_z^2 = (E_\pi + M_p - E_n)^2 - (\bar{p}_\pi - \bar{p}_n)^2 \qquad \ldots 1.8$$

where the quantities E_i, M_i, $\bar{p}_i$ are respectively the energy, mass and momentum of the particle i , all measured in the laboratory frame, where the proton is considered at rest.

This becomes

$$M_z^2 = (E_\pi + M_p - E_n)^2 - p_\pi^2 - p_n^2 + 2p_\pi p_n \cos\theta_{\pi n} \qquad \ldots 1.9$$

Here $\theta_{\pi n}$ is the angle between neutron and pion. It can be seen that measurement of the momentum vectors of the pion and the neutron, as described above, thus leads directly to a measurement of M_z. This method of measuring M_z is known as the 'missing-mass' method,

Fig. 1. 2. Basic apparatus

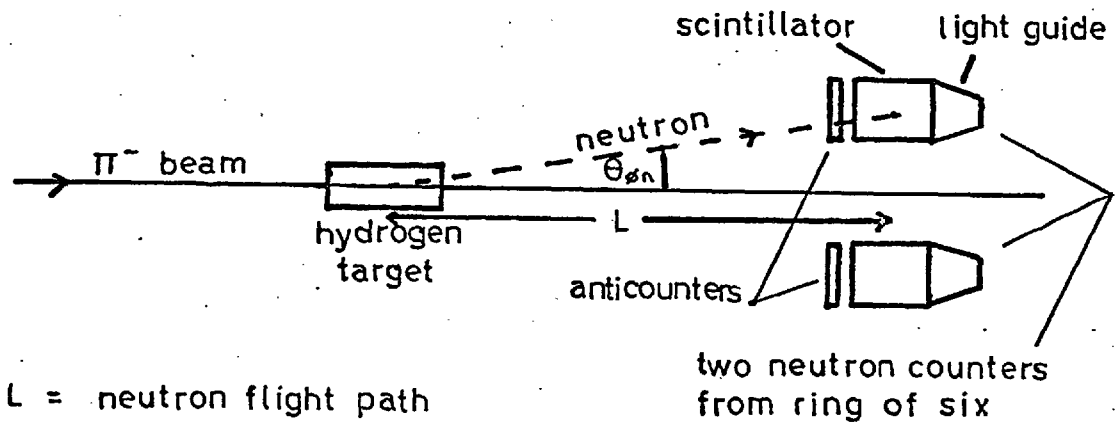

Basic experimental arrangement (not to scale)

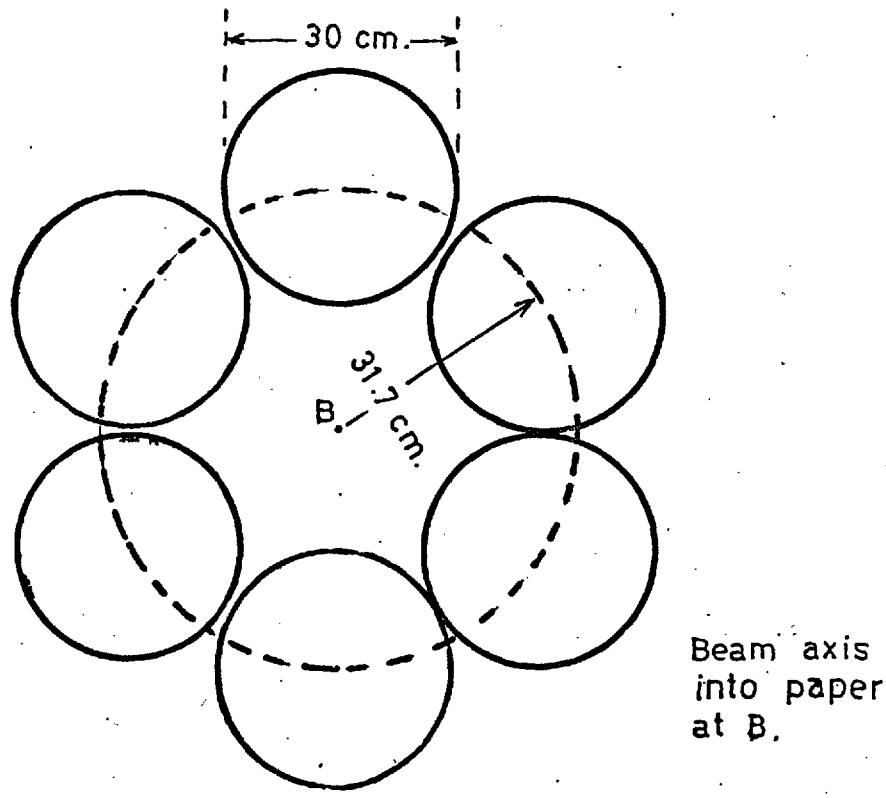

Ring of neutron counters

since M_z can be evaluated without making measurements on the constituent particles of the z^o system. The missing-mass method is a powerful yet relatively simple way of looking for new particles and resonances in the mass spectrum of the z^o system, as has been adequately demonstrated by the experiments of Maglic et al.[14] at CERN. It has the advantage that only one particle in the final state has to be detected and have its momentum measured, and it is thus very well suited to counter and spark chamber systems (which in turn allow for high precision experiments). A disadvantage in practice is that the data obtained often suffer strong experimental biases, and this makes it difficult to extract total cross-sections and angular distributions.

The missing-mass method is to be contrasted with the effective mass method of searching for unstable particles, in which the mass of the z^o system is determined from measurements made on its decay products. This is, however, usually difficult to do with a spark chamber/counter arrangement if there are more than two particles in the final state, and the technique is mainly used in bubble chamber experiments (an exception is the large magnetic spark chamber system).

In our experiments we study resonance production near the reaction threshold. In order to do this, six neutron counters of cylindrical shape are arranged symmetrically about the beam axis, downstream

of the hydrogen target, in the manner shown in Fig.1.2. This allows collection of neutrons with angles of ~ 2-6° to the beam axis in the laboratory, the exact angular range covered depending on the neutron flight path (L) employed; this arrangement also gives almost complete azimuthal coverage.

There are two main advantages of working in the threshold region. Firstly, it is possible to obtain good mass resolution for the z^0 system in this region, obviously desirable when studying narrow resonances such as the ϕ and ω mesons. That this is so can be seen by examining the partial derivatives of equation 1.9.

$$\frac{1}{2}\frac{\partial M_z^2}{\partial p_\pi} = -\beta_\pi (E_n - M_p) + p_n \cos\theta_{\pi n}$$

$$\frac{1}{2}\frac{\partial M_z^2}{\partial p_n} = -\beta_n (E_\pi + M_p) + p_\pi \cos\theta_{\pi n} \qquad \ldots 1.10$$

$$\frac{1}{2}\frac{\partial M_z^2}{\partial \theta_{\pi n}} = -p_\pi p_n \sin\theta_{\pi n}$$

where β_i is the velocity of particle i. It is seen that a condition for $\partial M_z^2/\partial\theta_{\pi n} = 0$ occurs when $\theta_{\pi n} = 0$; the condition for $\partial M_z^2/\partial p_n = 0$ is $\beta_n = \frac{p_\pi \cos\theta_{\pi n}}{E_\pi + m_p}$.

If $\theta_{\pi n} = 0$, this becomes $\beta_n = \frac{p_\pi}{E_\pi + M_p} = \beta_c$

where β_c is the velocity of the $\pi^- p$ centre of mass (c.m.s.)

system in the laboratory. The two conditions $\theta_{\pi n} \sim 0$ and $\beta_n \sim \beta_c$ are both satisfied near threshold, thus good mass resolution for the z^o system can be obtained in this region.

The second advantage of working near threshold is that a high neutron collection efficiency can be obtained for a given solid angle coverage by neutron counters in the laboratory. This is because, just above threshold, the neutrons are kinematically confined to a narrow forward cone in the laboratory; unless the reaction is strongly peripheral this is not true for pion momenta far above threshold. Thus our neutron counter arrangement collects ~ 75% of the neutrons produced, in the region of maximum collection efficiency.

The resonance production cross-section is likely to have a particularly simple dependence near the reaction threshold. The production cross section can be written as

$$\sigma = \frac{1}{\text{Flux}} \cdot T_{if}^{2} \cdot \rho \qquad \ldots 1.11$$

where T_{if} is the Lorentz invariant matrix element linking initial and final states, and ρ is the Lorentz invariant two body phase space density of states factor. The Lorentz invariant flux is $\propto P_i^x E$, and $\rho \propto P_f^x/E$; here E is the c.m.s. energy, and P_i^x (P_f^x) is the c.m.s. initial (final) state momentum.

Then–

$$\sigma \propto \frac{T_{if}^{\ 2}}{E^2 p_i^x} \cdot p_f^x \qquad \ldots. \ 1.12$$

p_f^x varies rapidly near threshold, while T_{if}, E, and p_i^x are all slowly varying in this region. Thus, close to threshold 1.12 can be approximated to

$$\sigma = A\, p_f^x \qquad \ldots. \ 1.13$$

where A is a constant.

The final state c.m.s. production angular distribution is also likely to have a simple form. This is because the final $z^o n$ system is produced with such a low c.m.s. momentum that it must almost certainly be predominantly S-wave, given that the strong interaction forces can extend only over a pionic wavelength or so.

From equation 1.13, the main disadvantage of working near threshold is apparent – the resonance production cross-section is likely to be relatively low close to threshold, and goes to zero at threshold itself. This factor offsets the high collection efficiency in the actual yield of neutrons that can be collected.

1.4 The need for an experiment to study Ø production in $\pi^- p$ interactions

The first experiment in the series, that of the measurement of the $\omega^o \longrightarrow e^+ + e^-$ branching ratio, was performed during

1964-5. In this experiment,[1,12] missing masses in the region of the ω were selected using the neutron counters as described in the last section. The electron and positron from the ω^0 decay were recognized by the fact that they shower in lead. The hydrogen target was enclosed on two sides by spark chamber/lead plate sandwiches. Photographs of events with the correct missing mass were then scanned for events where both the electron and positron produced the characteristic showers. On the basis of three good $\omega^0 \rightarrow e^+ + e^-$ events, the branching ratio for $\omega^0 \rightarrow e^+ + e^-$ was found to lie between the limits $(0.5\text{-}6.0) \times 10^{-4}$ (95% confidence limits). This was in good qualitative agreement with theoretical expectation.[1,15] The observation of the decays also showed the $\omega \rightarrow \gamma$ interaction was allowed, so that the ω was not a pure SU_3 singlet state. There was no disagreement between this result and those from other, less accurate, experiments.[16]

On the basis of the $\omega - \phi$ mixing hypothesis, the branching ratio for $\phi \rightarrow e^+ + e^-$ was now likely to be $\sim 1 \times 10^{-3}$. The higher branching ratio was, however, offset by the difficulty of producing ϕ's in $\pi^- p$ interactions. The channel $\pi^- p \rightarrow \phi n$ is difficult to recognize in a bubble chamber, and at the time of the original proposal to measure the $\phi \rightarrow e^+ + e^-$ branching ratio, there was no published evidence on it, though it seemed clear that in general ϕ production with pions was anomalously low compared

to ω production. ϕ mesons were normally studied using a negative kaon beam. However, the Steinberger group[17] had clear evidence of ϕ production in $p + \bar{p} \rightarrow K^+ + K^- + \pi^+ + \pi^-$, and Abolins et al.[18] had some evidence in $\pi^+ + p \rightarrow K^+ + K^- + \pi^+ + p$ at 3.5 GeV/c. These workers found a ratio of ω to ϕ production of about 60. Assuming that the cross-sections for ϕ and ω production both varied linearly with the final state c.m.s. momentum near threshold (see equation 1.13), the value of the linearity constant A for ϕ production was estimated at ~ 0.1 $\mu bar_n/MeV/c$, using this factor of 60 and the value of A measured from the ω experiment. The original estimates for the $\phi \rightarrow e^+ + e^-$ experiment were based upon this number for A for ϕ production, and it became clear that serious doubt would have to be cast upon the feasibility of the $\phi \rightarrow e^+ + e^-$ experiment if A was a factor of two or more lower than the estimated value.

It was therefore decided to perform a separate experiment to study ϕ production in $\pi^- p \rightarrow \phi n$ near threshold, in particular to estimate A. The process actually studied was $\pi^- p \rightarrow K^+ + K^- + n$, since $\phi \rightarrow K^+ + K^-$ is the dominant decay channel. The final estimate of A therefore required a knowledge of the partial width for this decay.

1.5 The ϕ meson

The ϕ meson was discovered by Bertanza et al.[19] at the Brookhaven National Laboratory using a K^- beam at 2.24 GeV/c, in a hydrogen bubble chamber experiment. They discovered the existence of a resonance in the $K\bar{K}$ system at ~ 1020 MeV/c^2, of width < 20 MeV/c^2. Shortly afterwards its quantum numbers were determined independently by groups at Brookhaven and UCLA.[20] The ϕ was found to decay predominantly into $K^+ K^-$ and $K_1^o K_2^o$, but never into $K_1^o K_1^o$. Observation of the $K_1^o K_2^o$ decay mode showed that ϕ had odd spin (J), negative parity (P), and negative C-parity (assuming it decayed into $K\bar{K}$ via strong interactions, borne out by its narrow width). These assignments follow from the relations

$$CP\,(K^o\bar{K}^o) = + \qquad CP\,(K_1^o K_2^o) = (-1)^{J+1}$$
$$C\,(K^+K^-) = P\,(K^+K^-) = (-1)^J \qquad \ldots\ldots 1.14$$

Comparison of the three $\Sigma\, K\bar{K}$ final states showed that the isospin (I) was zero, and that G was odd ($G=-(-1)^I$), since no $\phi^{\pm}$ was seen in the reactions $\Sigma^{\pm} K^{\pm} K^o$, and the triangle inequality

$$(\sigma_{\Sigma^+\varphi^-})^{1/2} + (\sigma_{\Sigma^-\varphi^+})^{1/2} > 2(\sigma_{\Sigma^o\varphi^o})^{1/2} \quad \ldots 1.15$$

was violated by more than five standard deviations. The G parity assignment was in agreement with the absence of the $\pi^+\pi^-$ decay mode.

The spin was determined by using the dependence upon spin of the quantity

$$\beta_J = \frac{\Gamma(\phi \rightarrow K_1^o K_2^o)}{\Gamma(\phi \rightarrow K^+K^-)} \qquad \ldots. 1.16$$

In the absence of a K^+K^o mass difference, and charge effects, this ratio is independent of J. The spin dependence of β_J arises from the different angular momentum and Coulomb barriers appropriate to the $(K_1^o K_2^o)$ and (K^+K^-) systems. A J = 1 assignment was found to be highly favoured over J = 3. This observation was also borne out by analysis of the decay angular distribution of the ϕ.

The quantum numbers of the ϕ are now established[21] as $I^G(J^P)\ C = 0^-(1^-) -$. The present values[21] of the ϕ mass and width are listed as 1018.6 $\pm$ 0.5 MeV/c^2, and 4.0 $\pm$ 1.0 MeV/c^2 respectively, and the main decay branching ratios as

$$\begin{aligned} \phi &\longrightarrow K^+K^- && 48 \pm 3\% \\ &\longrightarrow K_1^o K_2^o && 40 \pm 3\% \qquad \ldots 1.17 \\ &\longrightarrow \pi^+\ \pi^-\ \pi^o \text{ (including } \rho\pi\text{)} && 12 \pm 4\% \end{aligned}$$

As discussed previously, the ϕ meson fits into the $J^P = 1^-$ meson nonet on the SU_3 symmetry scheme, and is considered a mixture of the nonet's isoscalar octet and singlet states on the $\omega - \phi$ mixing theory.

One puzzling aspect of the ϕ is its lack of decay into $\rho\pi$.

Phase space calculations indicate this decay mode should dominate, but in practice it is suppressed by at least a factor of 3. Also, ϕ production in $\pi^- p$ interactions seems surprisingly low compared to ω production; in both cases only ρ exchange is allowed in the t channel. Both these apparent anomalies could result from a low $\phi\rho\pi$ coupling.

Bronzan and Low have explained this on A-parity arguments; since $A_{\phi,\rho} = +1$ and $A_{\pi} = -1$, $\phi \rightarrow \rho\pi$ and $\phi \rightarrow 3\pi$ are forbidden if A is a good quantum number. Another interpretation is given by the ω-ϕ mixing theory discussed previously. This accommodates suppression of the $\phi \rightarrow \rho\pi$ decay mode, saying the ω and ϕ mix in such a way that one of them has a much stronger interaction with 3 pions than the other. Glashow[22] has expressed the $\omega\rho\pi$ and $\phi\rho\pi$ couplings in terms of the ω-ϕ mixing angle θ, the coupling (g) of the vector octet to itself and the pseudoscalar octet, and the coupling (f) of the vector singlet to the vector octet and the pseudoscalar octet. The physical couplings are then linear combinations of g, f

$$\begin{aligned} G_{\omega\rho\pi} &= g\cos\theta + f\sin\theta \\ G_{\varphi\rho\pi} &= -g\sin\theta + f\cos\theta \end{aligned} \qquad \ldots\ 1.18$$

It can be seen that it is possible for $G_{\phi\rho\pi} << G_{\omega\rho\pi}$ on this scheme. This does not explain, however, why in practice the ϕ meson turns out to be the uncoupled state. Explanations of this exist,[23] but are not considered here.

1.6 Possible mechanisms for ϕ production in $\pi^- p \rightarrow \phi n$

Feynman diagrams for the possible single exchange mechanisms for ϕ production in $\pi^- p \rightarrow \phi n$ are shown in Fig.1.3.

Only ρ exchange is permitted in the t channel. From parity conservation at the meson vertex, the $\rho\pi$ system in the rest frame of the ϕ must be in a P wave angular momentum state. This angular momentum state is further constrained to the state Y_1^0 if the quantization direction is chosen to lie along the pion direction in the ϕ rest frame. The ϕ cannot then be produced in the $|J, J_z\rangle = |1, 0\rangle$ state, since the Y_1^0 state will not couple to the $|1, 0\rangle$ spin state of the ρ. The kaons from the ϕ decay must therefore be produced in the $Y_1^{\pm 1}$ state, which leads to a decay angular distribution of the form $\sin^2\theta_\phi$, (where θ_ϕ is the angle between the pion direction and one of the kaons in the ϕ rest frame).

In the s and u channels, $I = \frac{1}{2}$, $S = 0$, baryon exchange is allowed: this includes nucleon and $I = \frac{1}{2}$ π-N resonance exchanges. However, since we work so close to threshold, the final ϕn angular momentum state produced in our experiment will be almost certainly predominantly S-wave. If the ϕn state is restricted to $I = 0$ only, the quantum numbers $I(J^P)$ of allowed exchange particles in the S channel can be fixed to $\frac{1}{2}(\frac{1}{2}^-)$, $\frac{1}{2}(3/2^-)$. Nucleon exchange is therefore forbidden. Higher order allowed diagrams could incorporate N (1525)($\frac{1}{2}(3/2^-)$) exchange,

Fig. 1.3. Allowed Ø production diagrams.

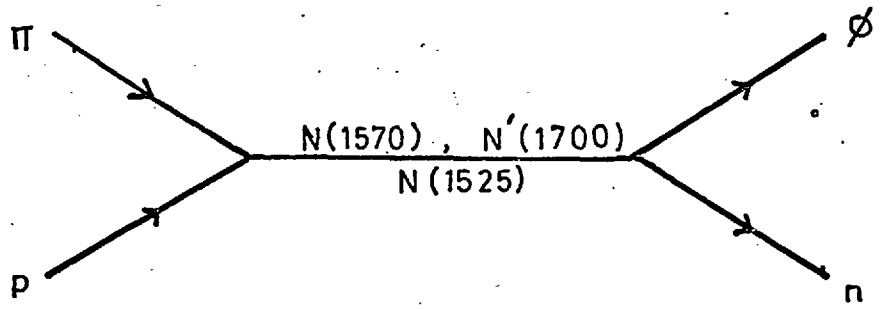

S Channel ($l_{\phi n} = 0$ restriction)

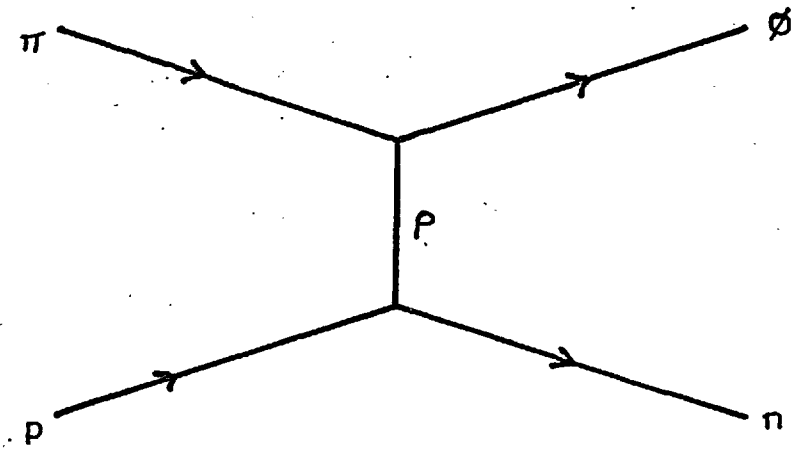

T Channel

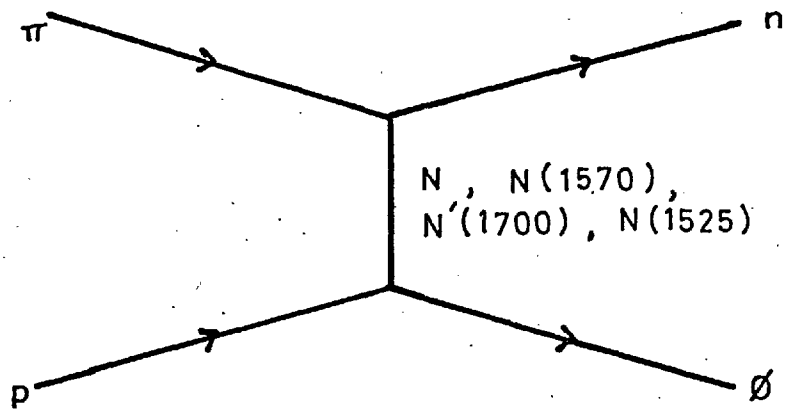

U Channel

and N (1570) and N'(1700) ($\frac{1}{2}(\frac{1}{2}^-)$) exchange.

In the u-channel, it is not obvious that any such restriction could be applied, so that nucleon exchange would probably be dominant in this channel, as the πN resonances are farther from the physical region.

Just above threshold, the first-order terms of ρ exchange and nucleon exchange in the crossed channels would occur at approximately the same distance from the physical region. Because of this, it is possible that the actual production mechanism cannot be explained using a single exchange diagram.

1.7 General outline of the ϕ production experiment

The apparatus designed to study ϕ production near threshold was a modified form of the basic 'missing-mass spectrometer' arrangement shown in Fig.1.2. In addition to the detection of the neutron with the neutron counters, detection of the K^+K^- system was also required.

The threshold for the reaction $\pi^- p \rightarrow K^+K^- n$ ($p_\pi = 1.49$ GeV/c) is close to the $\pi p \rightarrow \phi n$ threshold ($p_\pi = 1.56$ GeV/c). As a result, the kaons from the ϕ decay have little kinetic energy in the ϕ rest frame, and for beam momenta just above ϕ threshold, go forwards in the laboratory. This fact was utilised in the design of the apparatus. A diagram of the apparatus is shown in Fig.3.1; a detailed description will be given in Chapter 3. The dikaon pair, emitted forwards in the laboratory, was

detected by the arrangement of scintillation counters at E. The arrangement demanded that two charged particles should arrive simultaneously from the hydrogen target. If this condition occurred coincidentally with a beam particle interacting in the target, and a neutron being detected by a neutron counter, photographs were taken of the charged kaon tracks in a bank of spark chambers surrounding the scintillator arrangement E. These pictures were later scanned according to certain criteria which could be satisfied by a true dikaon pair. From the pictures satisfying these criteria, the angles of the kaons in the laboratory were measured. The input pion momentum, and the time of flight and direction of the neutron, were also recorded, so that for each event the only unknowns were the two kaon momenta. The events were then fitted to the hypothesis $\pi^- p \rightarrow K^+K^- n$ in a kinematic fitting programme.

Various backgrounds were able to simulate $\pi p \rightarrow \phi n$ in the electronic trigger employed. However, it turned out that these could all be virtually eliminated by careful design of the apparatus, and by using suitable scanning criteria (this is discussed further in Chapter 3). The $K^+K^- n$ background in this channel was, of course, not affected by these devices. At the outset, it was not clear what contribution should be expected from this. Because the $K\bar{K}$ threshold was so close, the phase space volume available was small. On the other hand, there was

evidence of a $K_1^oK_1^o$, S-wave enhancement near the $K\bar{K}$ threshold.[24] This was supposed the manifestation of a G = +1 $K\bar{K}$ state, which might be seen in our experiment in its K^+K^- mode. These uncertainties about the K^+K^-n background implied that the mass range covered around the ϕ should be large enough to see the ϕ in the $K\bar{K}$ mass plot as a bump on a more slowly-varying background; a mass range $\sim \pm 25$ MeV/c^2 about the ϕ mass was thought sufficient for this. The mass resolution expected ($\sim \pm 5$ MeV/c^2) would be sufficient to see the ϕ, if it was produced, within this range.

In the experimental analysis, theoretical events were generated on a computer using a Monte Carlo programme, which simulated exactly the processes a real event would undergo - its generation in the hydrogen target, its collection and measurement by the apparatus, and finally, its fitting to the $\pi^-p \rightarrow K^+K^-n$ hypothesis. This programme generated $\phi \rightarrow K^+K^-$, and K^+K^- background events, according to certain models (these are discussed later). The effects on the experimental distributions of the biases and resolution due to the apparatus were automatically included in this process. Theoretical distributions compiled from the Monte Carlo events could then be compared with their experimental counterparts, thereby testing the models used.

In this way it was hoped to study ϕ production near threshold; apart from allowing us to make the necessary

cross-section measurements, it might also be possible to see how the ϕ was being produced in this reaction near threshold. There was also a chance that we could investigate the $K\bar{K}$ threshold enhancement. However, any statement we might make about this would probably be weak; previous studies[24] had shown it was produced preferentially in the low momentum transfer regions (< 0.3 $(GeV/c)^2$), hardly reached in our experiment, and even if it was produced, it might be strongly contaminated with ϕ and non-resonant K^+K^- background over our mass range.

CHAPTER 2

THE BEAM

2.1 Design of the beam

The negative pion beam used for the experiment was designed to operate over a small momentum range, 1.3-1.8 GeV/c, centred on 1.56 GeV/c, when the accelerator was operating at 7 GeV primary proton energy. The basic requirements of the beam were that it should give a high yield, and a reasonably large momentum bite, over this range. The beam was produced from a machine target of copper, 1 x 1 cm^2 in cross-section, and 10 cm long. The target was situated in a machine octant, so that the machine 'fringe' field considerably influenced the motion of particles from the target. The effect of this field on secondary particles produced in the target has been calculated by Whiteside,[25] and some of his results, for negative particles, are summarized below.

Consider first the radial (horizontal) plane (Fig.2.1). The target is supposed situated on the central radius R_o (R_o = 18.78 m), which is near the centre of the good field region of the machine. The machine field acts for effectively a distance R_e = 2m outside this radius. A particle having a given momentum P, and production angle α , will emerge from the fringe field at a definite radial position, given by θ_e, in a direction which makes an angle ϕ_e

Fig. 2.1. Coordinate system in radial plane

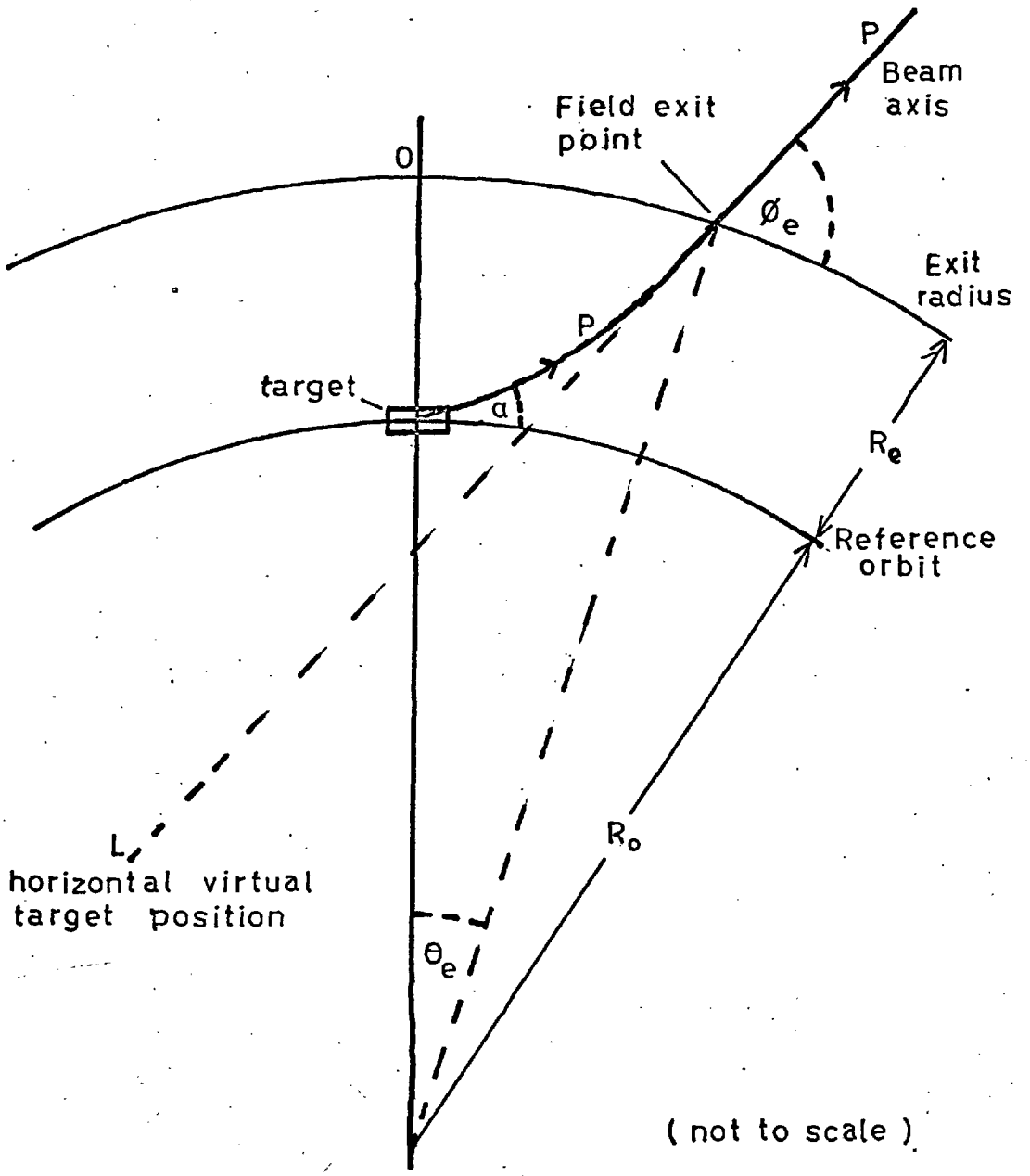

with the tangent to the fringe field at the exit position, as shown in Fig.2.1. Therefore each point on the θ_e v ϕ_e plot of Fig.2.2 will have an associated α and p value. Lines of constant α, and lines of constant p, are shown on the plot. From the plot can be seen -

a) the fringe field acts as a strong disperser of momentum in the horizontal plane. For fixed α, an increase in momentum decreases ϕ_e and increases θ_e.

b) the fringe field acts as a focussing system in the horizontal plane; lines of constant momentum have, to a good approximation, $\phi_e(\alpha) = \phi_e(-\alpha)$, though these trajectories have different θ_e values. The fringe field, however, defocusses in the vertical plane.

These effects lead to certain advantages of negative beams from mid-octant targets, over beams from targets in straight sections.

a) It is possible to work at zero production angle, where the secondary pion yield is expected to be highest.

b) Angular acceptance can be greater than from a target in a straight section. The reasons for this are that it is usually possible to place the first component of a beam channel nearer the target, and that the radial focussing in the fringe field can outweigh the vertical defocussing.

Fig. 2.2. Exit directions in θ_e v. ϕ_e coordinates (after Whiteside).

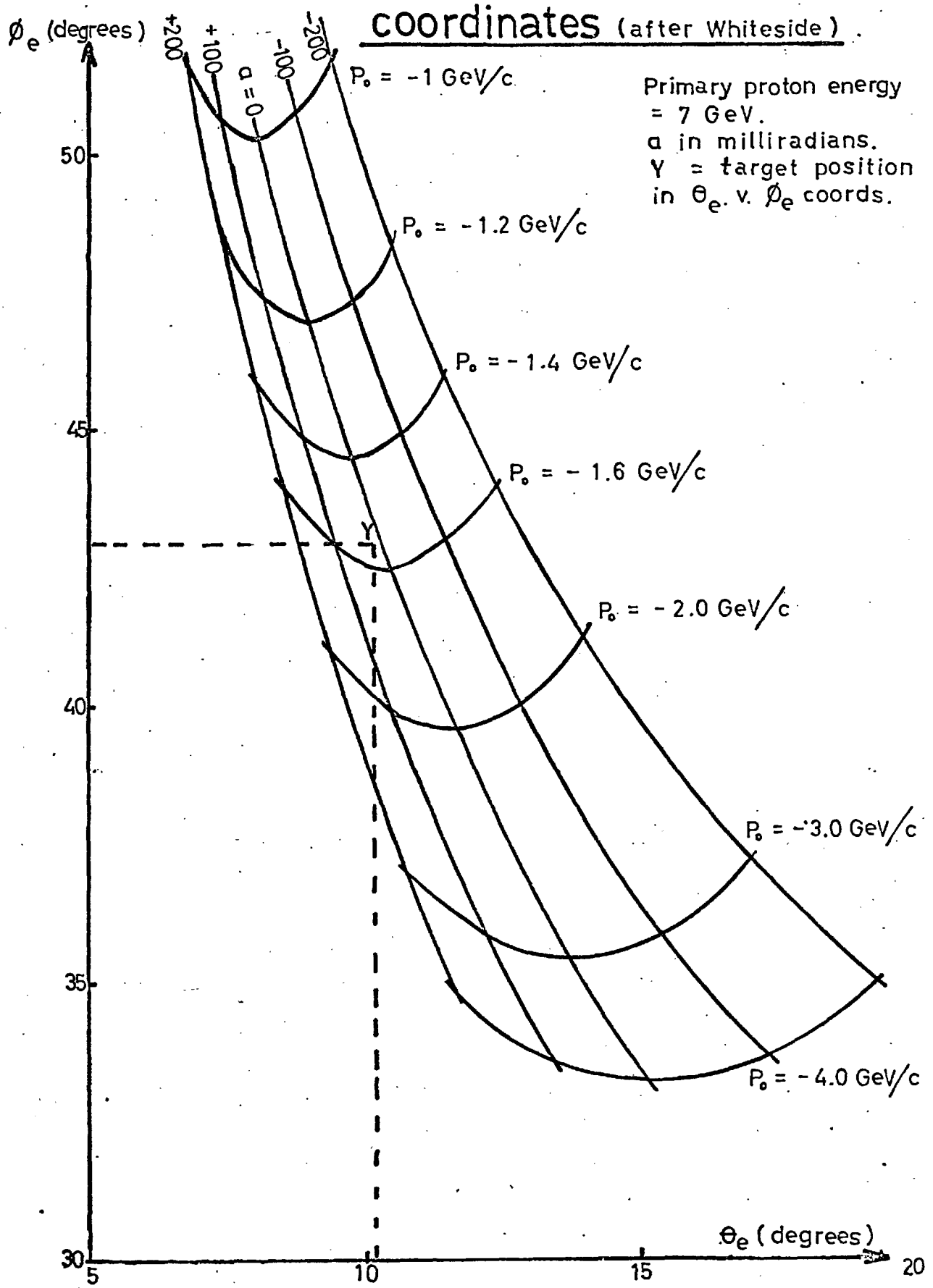

The disadvantage is that the range of negative momenta is limited to 20-30%, due to the finite range of ϕ_e values accepted by the beam channel because of the machine dispersion, though it may be extended by varying the circulating proton beam momentum i.e. varying the machine field. This lack of flexibility, together with the dependence on machine field level, are disadvantages not shared by beams using targets in straight sections. For the ϕ production experiment, however, it was decided to accept this limitation, in order to obtain a high flux.

It should be noted that positive particles tend to be swept into the machine by the machine field, rather than out of it, so that only negative particles could enter the beam channel.

A diagram of the beam is shown in Fig.2.3. The position and direction of the initial part of the beam channel was determined from the θ_e v ϕ_e plot of Fig.2.2. Since we required particles of zero production angle, and a central design momentum p_o of 1.56 GeV/c, ϕ_e and θ_e were chosen as 42.9° and 10.15° respectively (this actually gave $\alpha = +10$ mrad). A quadrupole doublet, consisting of a pair of type II quadrupoles,[26] was placed at the entrance to the beam channel, as close as possible to the machine. The first element of the doublet, Q1, was made vertically focussing to collect as much flux as

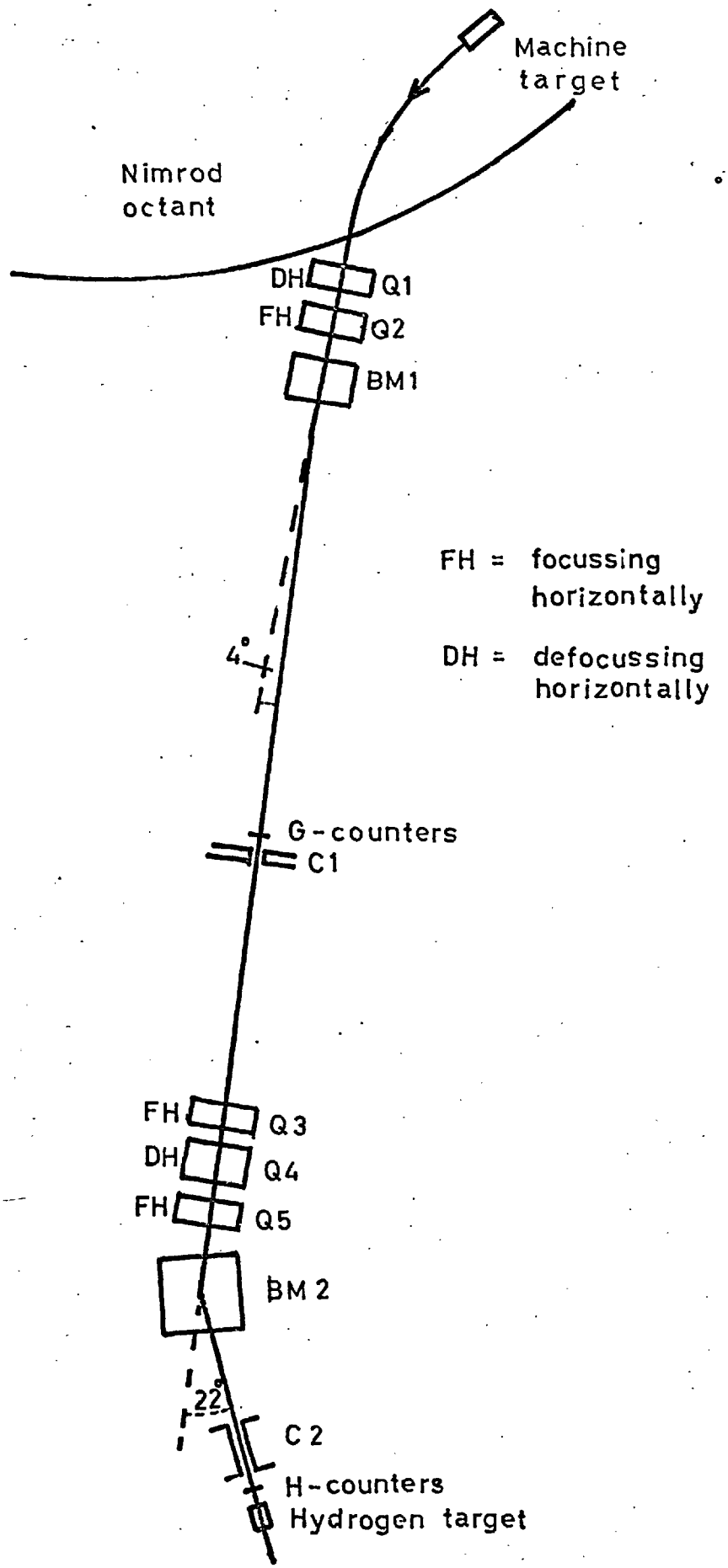

Fig. 2.3. The Beam. (approximately to scale)

possible, since the particles leaving the fringe field were diverging rapidly, due to the vertical defocussing of the fringe field. The doublet focussed the beam, in both horizontal and vertical planes, to a lead collimator C1 10 m. downstream. This collimated the beam horizontally, having a 5 cm vertical slit at its centre.

Immediately following the doublet was a type IV[26] bending magnet BM1. This magnet introduced a 4° bend into the beam axis, and thereby increased the dispersion already caused by the machine. Its basic function, however, was to act as a 'momentum-selecting' magnet. From the θ_e v ϕ_e plot, it can be seen that particles of a momentum different from p_o emerge, at a fixed θ_e, with a different value for ϕ_e. However, by suitable adjustment of the BM1 field, the target image of any momentum entering the beam channel could be brought coincident with the C1 collimator slit, thereby overcoming this difficulty. Only the narrow band of momenta which fell on this slit was then able to traverse the second stage of the beam.

The second stage of the beam was used to measure the momentum of particles emerging from the collimator slit. It also cancelled to a large extent the dispersion introduced in the first stage. Particles from the collimator C1 were focussed (horizontally and vertically) onto the hydrogen target by means of a quadrupole triplet, using a type II bending magnet (BM2) to

deviate the beam through 22° into the hydrogen target. The triplet consisted of a type I quadrupole (Q4) flanked on either side by a type II quadrupole (Q3, Q5). Q3 centre was 5.3 m downstream from C1 collimator. The triplet was operated symmetrically i.e. the outer quadrupoles had the same field gradient. The beam was diverging faster horizontally than vertically after it had traversed the C1 collimator, so the outer quadrupoles were made horizontally focussing, and the inner vertically focussing. The advantage of using a triplet here was that the magnification between the images at hydrogen target and collimator could be made close to unity in both planes, while at the same time preserving the acceptance in the second stage. A doublet would have tended to give a high horizontal magnification, and this was already fairly large at the collimator.

A second lead collimator C2, of length 1 m., cross-sectional area $1 \times 1\ m^2$, and with an 8 cm diameter hole cut in it for the beam to pass through, was positioned just in front of the hydrogen target. The effect of this was to reduce the number of stray particles at the target associated with the beam, but outside the beam itself. These particles would otherwise have increased the background counting rates of the various scintillation counters grouped near the beam axis, and produced background tracks in the spark chambers away from the beam axis. The collimator did not affect the true beam particles.

2.2 Calculation of beam parameters

Calculations of the various beam parameters were made using the standard computer programmes TRAMP and IPSO FACTO,[27] in conjunction with the Whiteside results on the fringe field effects. The focussing (or defocussing) effect of the fringe field was represented mathematically by considering the fringe field to produce a virtual image of the target inside the machine on the extrapolation of the beam axis, in both horizontal and vertical planes (see Fig.2.1). The field gradients of the quadrupole elements in the beam were matched to the foci for the design momentum, using TRAMP.

Data on the beam parameters is set out below.

	Horizontal plane	Vertical plane
Distance of virtual target image from exit point O	13.4 m.	2.35 m.
Magnification of virtual image	5.3	0.4
Nett magnification of target image at C1 collimator	2.3	2.33
Nett magnification of target image at hydrogen target	2.6	2.4

Horizontal momentum dispersion by fringe field, in plane of virtual image	+2.8 cm/1% momentum increase
Nett horizontal dispersion at C1 collimator	+1.9 cm/1% momentum increase
Nett horizontal dispersion at the hydrogen target	+0.35 cm/1% momentum increase

The total solid angle acceptance of the beam as a function of momentum is shown in Fig.2.4. The plot also shows the phase space 'acceptance polygons' in the virtual machine target phase space (entrance phase space), in both the horizontal and vertical planes (which are treated separately in the phase space calculations). In the displacement-divergence phase space (for one plane) appropriate to any point along the beam axis, the corresponding aperture limits (in that plane) are represented by a pair of vertical lines. Transformed back through the system, these generally appear as a pair of tilted parallel lines in the entrance phase space. Any particle whose initial phase point lies between the lines will pass through the relevant aperture. If the aperture lines of all the elements are transformed back to the entrance, a set of parallel line pairs, tilted at various angles, is obtained in the entrance phase space. For systems of finite acceptance, the lines will define an innermost polygon, within which all phase points represent particles which would traverse the system unscathed. The boundary lines of the polygon then show the apertures limiting acceptance ofthat momentum. The total solid angle accepted at that momentum can be obtained from a combination of the areas of the acceptance polygons in both the horizontal and vertical planes.

Fig. 2.4.

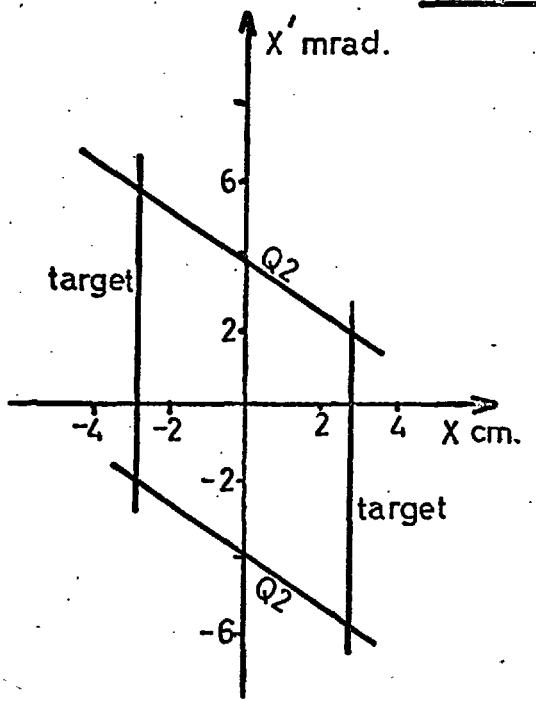

Horizontal acceptance polygon for p_0 momentum

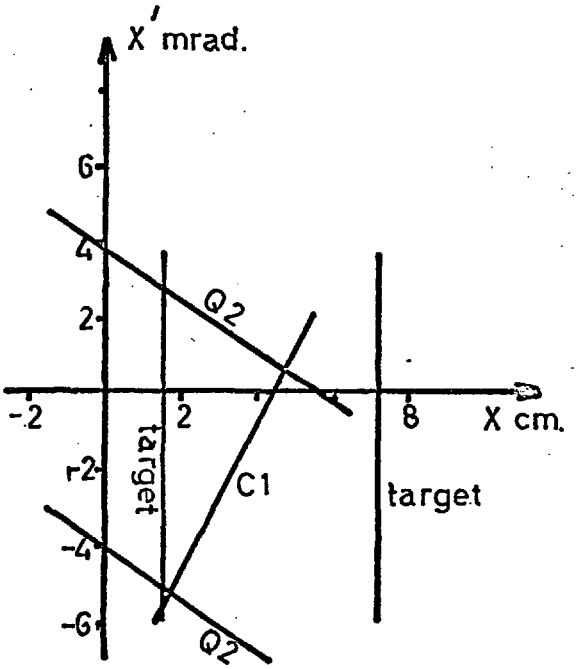

Horizontal acceptance polygon for $p_0 + 1.5$ % momentum

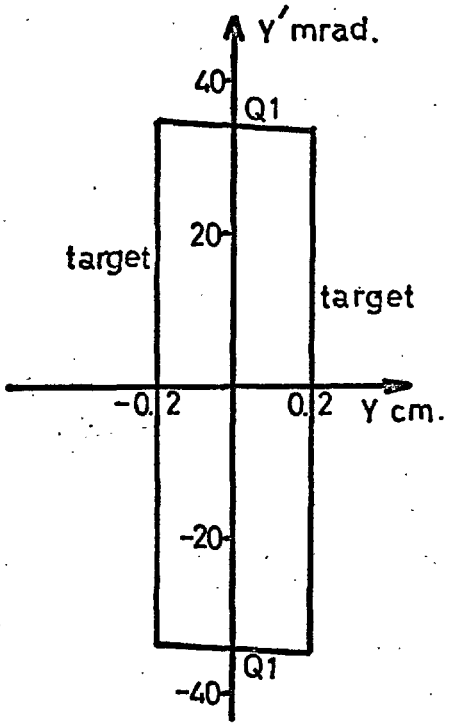

Vertical acceptance polygon for p_0 momentum

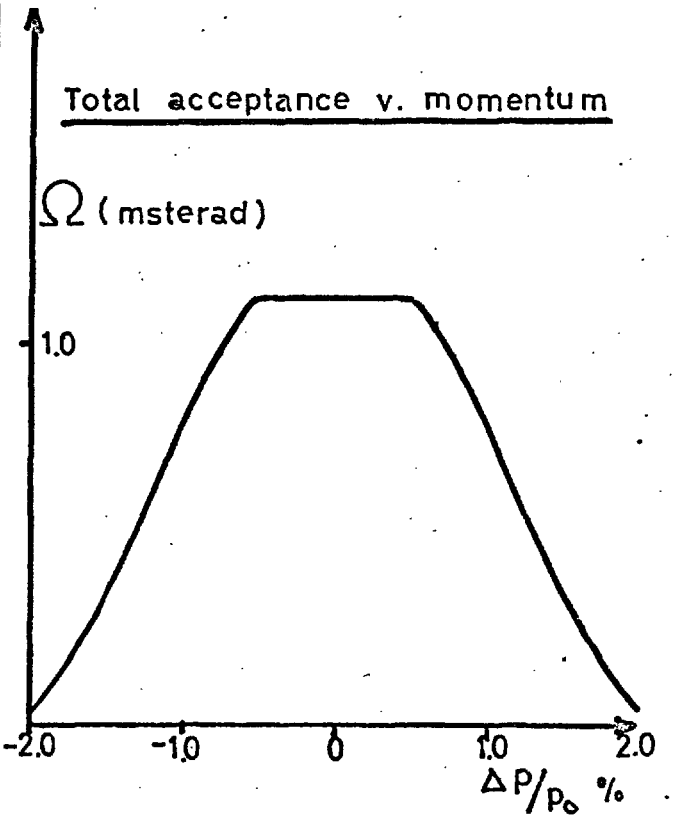

In our case, it can be seen that the acceptance in the vertical plane was limited by Q1 aperture only (and of course the virtual target edges) for the central momentum, p_o. The vertical acceptance was in fact independent of momentum over a $p_o + 2\%$ to $p_o - 2\%$ momentum range, so that variations in the graph of total solid angle acceptance against momentum are due to variations in horizontal acceptance. In the horizontal plane, the acceptance for p_o momentum was limited only by Q2 aperture. The horizontal acceptance was constant for $\frac{1}{2}\%$ change in momentum in either direction, but then became limited by the C1 collimator as shown. This momentum 'bite' was deemed sufficient for our purposes, though making C1 wider would have increased it, until eventually elements in the second stage of the beam would have begun to limit the bite.

The divergence of the beam at the hydrogen target was kept relatively small ($< \sim 14$ mradian horizontally, $< \sim 7$ mradian vertically) partly in order to keep the beam away from scintillation counters placed near the beam axis downstream of the hydrogen target.

2.3 The momentum measurement - the hodoscope

The momentum measurement of the pion in the second stage of the beam was accomplished using a hodoscope of scintillation counters. Six vertical 'finger' counters (called G-counters, of dimensions 0.8 cm horizontally, 4 cm vertically, 0.3 cm thick)

were placed side by side without overlap across the beam (but slightly staggered along the beam axis), as near as possible to the C1 focus (~ 20 cm upstream), so that they almost completely filled the 5 cm C1 aperture; a second group of 4 counters (H-counters, of dimensions 0.88 cm horizontally, 6.5 cm vertically, 0.3 cm thick), was similarly placed about 20 cm upstream of the hydrogen target focus, so that the two groups were at conjugate points of the triplet lens system (see Fig.2.5). The momentum of a particle could be obtained by measuring its horizontal position relative to the beam axis in both the G-counter plane and the H-counter plane (by noting the particular hodoscope counter that had fired in each plane), and by knowing the dispersion introduced between the G and H counters by BM2. Because this measurement was made very near a focus in both cases, the momentum measurement did not demand a knowledge of the particle's divergence in either counter plane, and from this it also follows that the measurement would not be much affected by scattering of the particle in the scintillator fingers. The width of the individual G-counters was matched to that of the H-counters (so that the image of a G-counter in the H-counter plane was the same width as the H-counter), knowing the magnification between the G- and H-counter planes.

The momentum of the particle was therefore defined, within the resolution, by the particular GH combination it triggered.

Fig. 2.5.

Arrangement of hodoscope counters

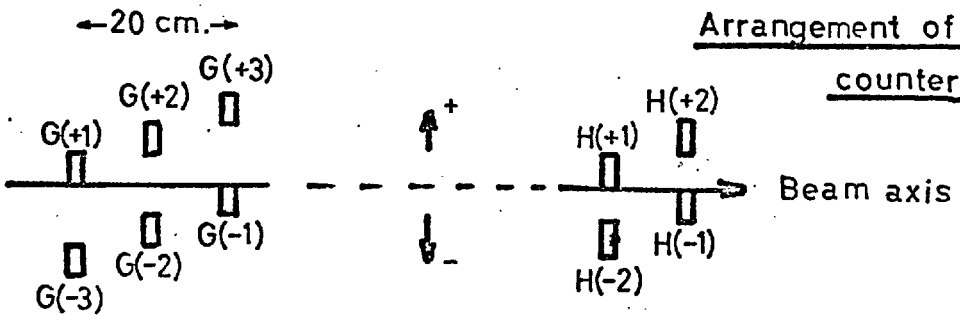

The GH combinations of each momentum channel

Momentum channel	Counter combination
2	G(+3)H(+2)
3	G(+2)H(+2) + G(+3)H(+1)
4	G(+1)H(+2) + G(+2)H(+1) + G(+3)H(-1)
5	G(-1)H(+2) + G(+1)H(+1) + G(+2)H(-1) + G(+3)H(-2)
6	G(-2)H(+2) + G(-1)H(+1) + G(+1)H(-1) + G(+2)H(-2)
7	G(-3)H(+2) + G(-2)H(+1) + G(-1)H(-1) + G(+1)H(-2)
8	G(-3)H(+1) + G(-2)H(-1) + G(-1)H(-2)
9	G(-3)H(-1) + G(-2)H(-2)
10	G(-3)H(-2)

Used

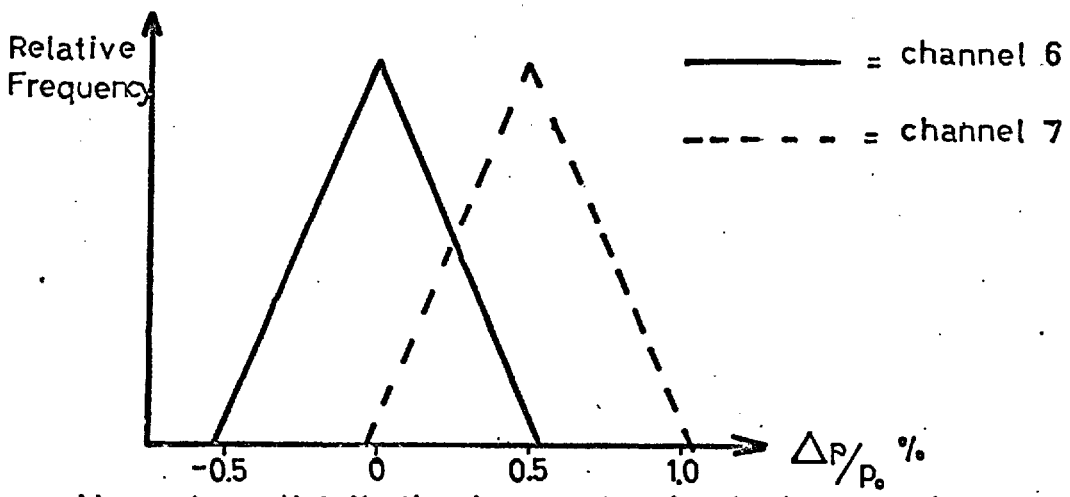

Momentum distribution in neighbouring hodoscope channels

There were in fact 24 different GH combinations, but as many of these measured in the same momentum range, there were only 9 distinct momentum 'channels' (numbered 2-10 in Fig.2.5). Only 4 of these channels were actually used in the experiment viz. channels 4-7 inclusive, channel 6 being the central channel.

2.4 The momentum distribution in a hodoscope channel

Due principally to the finite widths of the hodoscope counters, the momentum of particles in a single hodoscope channel was not unique, but characteristically distributed over a certain range of momenta. The momentum distribution of the particles in a particular hodoscope channel was taken as having the shape of an isoceles triangle whose full width at half height was $(0.55 \pm 0.02)\%$ in momentum, with the central momentum for that channel at the apex position of the triangle (see Fig.2.5). The separation between the central momenta of neighbouring hodoscope channels was taken as 0.5%. The momentum distribution in a hodoscope channel was an important quantity in the experimental analysis, and therefore this subject has been fairly extensively discussed in Appendix A.

2.5 Shimming of bending magnet BM2

The momentum measurement would have been made rather inaccurate if the quantity $\int \underline{B}.\underline{dl}$, taken along the various theoretical trajectories allowed for the particles in the magnet BM2, varied by a large amount across the cross-sectional area of the beam

in the magnet (here $\underline{B}$ is the BM2 field, $\underline{dl}$ an element of the particle trajectory). In this case, particles of the same momentum (p) emerging from a point in the G-counter plane, could not be made to form a point image in the H-counter plane, since particles having different entry points to the magnet would suffer different horizontal bends (the bending angle $\phi = 300 \int \underline{B}.\underline{dl}/p$). Variations in $\int \underline{B}.\underline{dl}$ between different theoretical trajectories were measured using a long thin search-coil and a servofluxmeter, and these variations were then minimised by shimming the poleface ends of the magnet in the necessary places. The long edges of the coil followed the shape of the theoretical particle trajectory (see Fig.2.6) over the non-zero field region. The width of the coil was small (2 cm) and constant, so that the flux through the coil was proportional to $\int \underline{B}.\underline{dl}$ over the trajectory i.e.

$$\oint_{\text{area}} \underline{B}.\underline{da} = w \int_0^l \underline{B}.\underline{dl} \qquad \ldots\ldots 2.1$$

since the cross-sectional area of the coil $a = wl$ (l = coil length, w = width).

The coil was constructed by A. Duane. It was mounted on a wooden board, and could be moved about in the magnet volume to cover all the theoretical trajectories allowed over the cross-section area of the beam at BM2 (18 cm horizontally, 8 cm vertically). Before making $\int \underline{B}.\underline{dl}$ measurements with this

Fig. 2.6. Shimming of BM2

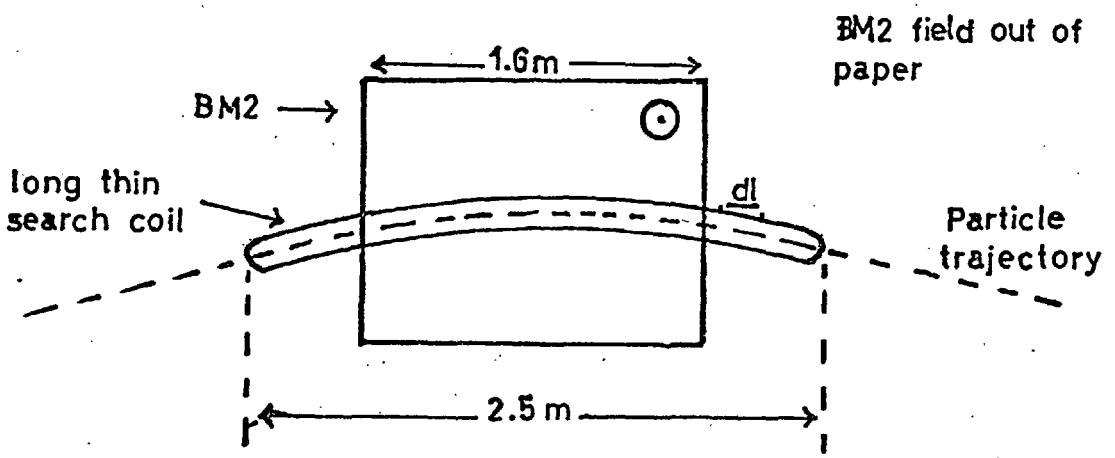

Plan View

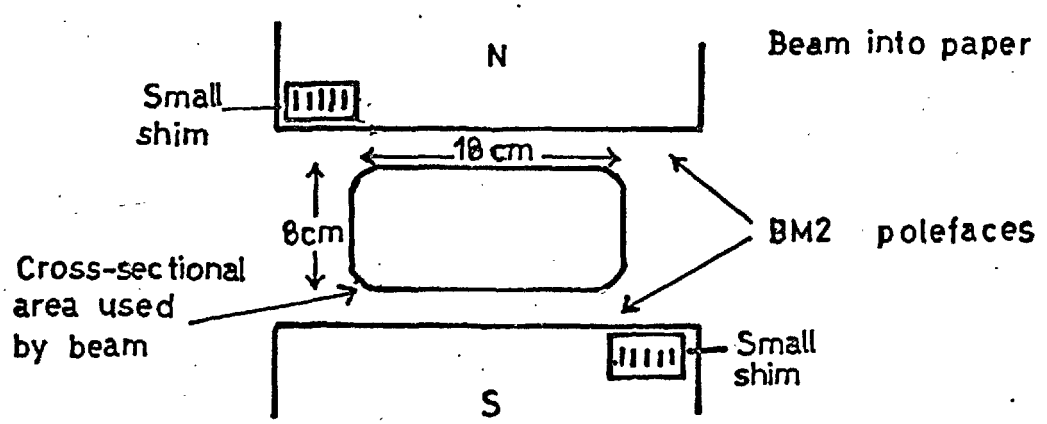

End View

long coil, a small search coil was used to check the uniformity of the field B itself over the central horizontal plane of the magnet. This field distribution had previously been made uniform to 0.01% at a somewhat lower field by A.Duane, using long steel shims placed inside the magnet. This uniformity was found to hold at the fields required for the present experiment, so the long coil was then used to obtain uniform $\int \underline{B}.\underline{dl}$ by attaching small steel shims, where necessary, to the poleface edges at the corners of the magnet volume (Fig.2.6), to increase the effective length of the magnet near entry points along whose associated theoretical trajectories $\int \underline{B}.\underline{dl}$ was low. In this way a flux linkage uniformity was obtained such that the horizontal width of the image at the H-counters, of a point source at the G-counters was < 1.5 mm, small compared to the H-counter width (8.8 mm). This was so over the whole range of field strengths necessary for this experiment.

2.6 Floating Wire measurements

In order to find the absolute momentum of a particle as accurately as possible, the second stage of the beam, where the momentum measurement occurred, had first to be calibrated using a known momentum. Therefore a series of 'floating wire' measurements was made on the second stage of the beam. The 'floating wire' can be thought analogous to a particle of known

momentum by virtue of the fact that a wire under tension (T gm) and carrying a current (i amp) will take up the same trajectory along the beam as a particle of momentum p (MeV/c). The analogue equation is:

$$p = 2.941 \frac{T}{i} \qquad \ldots\ldots 2.2$$

The wire was 'floated' through the second stage of the beam between two reference points on the beam axis, one at the C1 collimator, the other at the hydrogen target (see Fig.2.7). It was fixed at the collimator point, and passed over a pulley about 1 m in front of the hydrogen target reference point. The tension was produced by a weight on the wire at the pulley. For fixed triplet and BM2 currents, and a fixed analogue momentum, the wire would take up different stable trajectories depending on the position of the pulley in the horizontal plane. The extrapolation of these trajectories beyond the pulley intersected at the position of the focus.

By adjusting the bending magnet and triplet currents, the extrapolated wire trajectories could be made to pass through the hydrogen target reference point for all horizontal positions of the pulley. These currents then corresponded to those necessary to focus and bend the particles of that momentum from C1 reference point to the hydrogen target reference point. This procedure was repeated for various

Fig. 2.7. The 'floating wire' arrangement

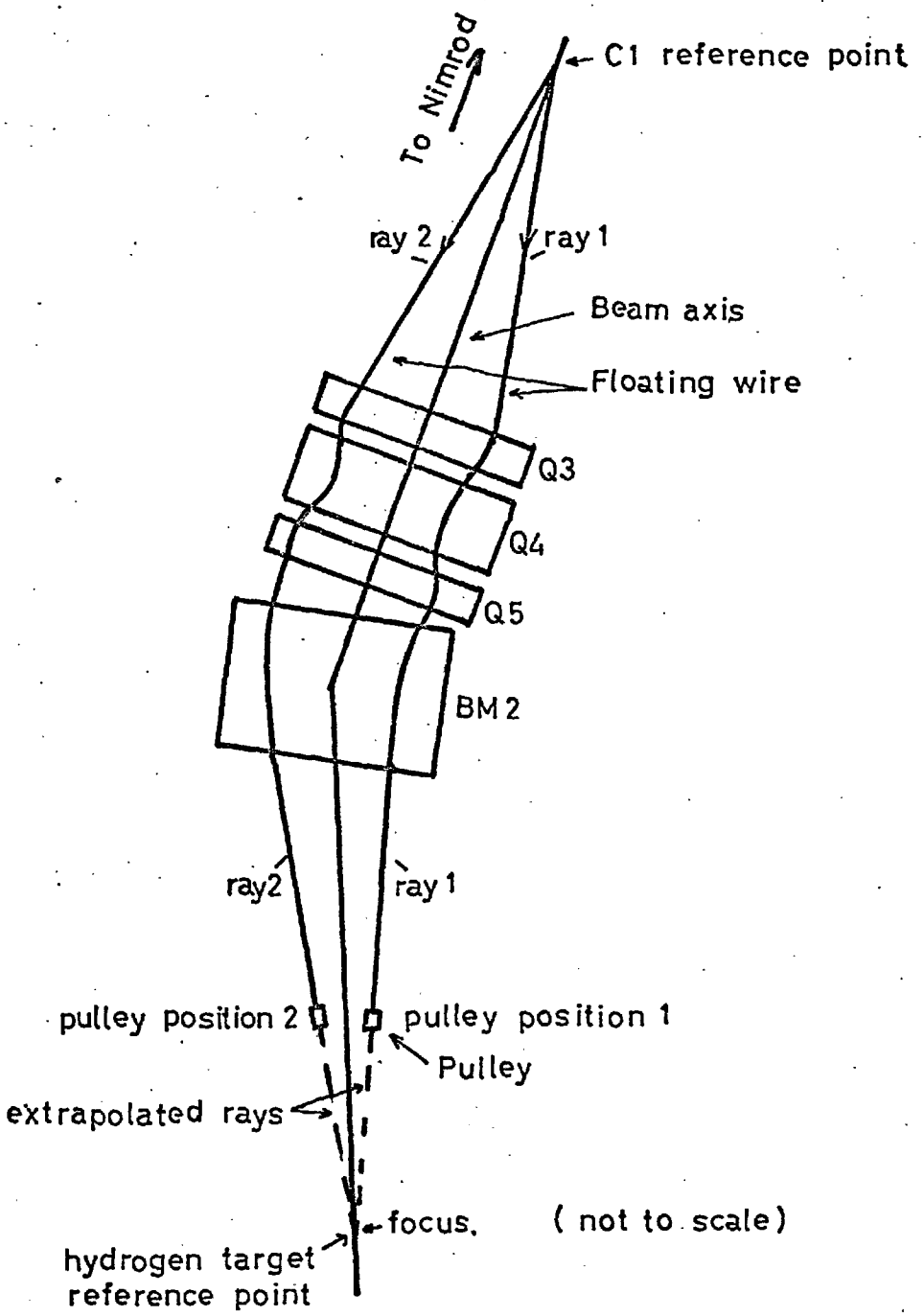

momenta between 1.48 and 1.62 GeV/c, the range to be used in the ϕ experiment.

The error in the absolute value of the analogue momentum due to errors in the tension and wire current was $\pm$ 0.15%. In practice, BM2 current was used to define the absolute central momentum of the beam at a particular instant, using the floating wire calibration in reverse. The error introduced into the value of this momentum by the inaccuracy of the wire analogue momentum was smaller than the error due to hysteresis in the BM2 magnet ($\pm$0.25%, making the total error $\pm$0.3%). Hysteresis effectively destroyed the unique relationship between $\int \underline{B}.\underline{dl}$ over the BM2 field (which determined the absolute central momentum directly), and the BM2 current. This effect could have been avoided to a large extent by measuring the BM2 field instead of its current, but it was not possible to obtain a suitable measuring instrument, either during these measurements, or during the data-taking.

The triplet was also required to focus the beam vertically between the two reference points, but this was not attempted in the floating wire measurements, and the wire was kept on the beam axis vertically. The measurements were used to construct a curve of I_3/p against I_4/p for the triplet (I_3 was the current in Q3, Q5, I_4 the Q4 current). Every

point on this curve represented possible I_3, I_4 values for a horizontal focus to be achieved at the target reference point, but with the I_3, I_4 values for the additional condition of a vertical focus at this point unknown. These currents were found during the setting-up of the beam.

Much of the apparatus used during these measurements was provided by A. Duane.

2.7 Beam Setting-Up and Performance

Under normal operating conditions, the beam was set up for a particular central momentum, by first adjusting the BM2 current to that required for this momentum by the floating wire calibration. The quadrupoles were then focussed for this momentum, and finally BM1 was 'optimized', so that the image of the central momentum was symmetric about the beam axis at the G and H counters. This was deemed to be the case when the counting rates in channels 5 and 7 of the hodoscope, on either side of the central channel, were equalized by BM1 adjustment.

However, in the initial beam setting-up, at the design momentum, the quadrupoles were first set at the approximate currents given by the TRAMP programme, and BM2 current was taken from the floating wire calibration; BM1 was then roughly optimized. The triplet was then focussed vertically by

adjusting I_3, I_4, according to the graph taken during the floating wire measurements, until the coincidence counting rate between two horizontal strip counters, on the beam axis at C1 collimator and the hydrogen target respectively, became a maximum. The doublet, already roughly focussed, was then adjusted to provide a focus horizontally and vertically at C1 collimator, again using horizontal and vertical strip counters.

The beam profile at the hydrogen target was roughly gaussian-shaped, with a full width at half height (FWHH) in both planes of 3 cm. At the C1 collimator, the vertical profile had a FWHH of 3 cm. These results were in reasonable agreement with the TRAMP predictions. The ratios of the counting rates in the different GH combinations of a particular hodoscope channel were in good agreement, both for channel 6 and channel 4, with the same ratios calculated from the IPSO FACTO programme. The ratio of the total count rates in channels 4 and 6 also agreed with the theory.

The total yield of particles in the 4 central hodoscope channels used (~2% momentum bite) was $\sim 8 \times 10^4$ particles for every 10^{11} protons hitting our machine target.

2.8 Beam Composition

The beam used consisted mainly of pions, muons and electrons, less than 1% of it being kaons and antiprotons.

The percentage of pions in the beam at 1.58 GeV/c was found using a gas Cerenkov counter, as a threshold device. The beam was made to pass through 3 counters S_1, C, S_2 as shown (Fig.2.8). The Cerenkov counter contained Arcton 13 gas at a certain pressure, which could be varied. The variable ε (p) was defined as the ratio of the counting rates S_1CS_2/S_1S_2 at a fixed gas pressure p. The curve of ε (p) v. pressure, obtained at a given momentum is shown in Fig.2.8. Electrons could be detected with the gas at atmospheric pressure. On raising the pressure, the thresholds for Cerenkov light production, first by muons, then by pions, were successively passed through.

The percentage of pions in the beam was found by estimating the percentage of muons and electrons, and subtracting from 100%. The efficiency of the counter for one type of particle at a given pressure, was a function of the excess pressure of the gas above the Cerenkov threshold pressure for that particle. The dependence of this efficiency upon excess pressure was first estimated for pions, from the data above the pion threshold, and this dependence was then used for electrons and muons. For the electron fraction, the value of a point on the ε (p) v. p. curve just below the muon threshold was corrected for the effect of uncorrelated random coincidences between S_1. S_2 and C,

Fig.2.8. Čerenkov pressure curve for 1.58 GeV/c particles

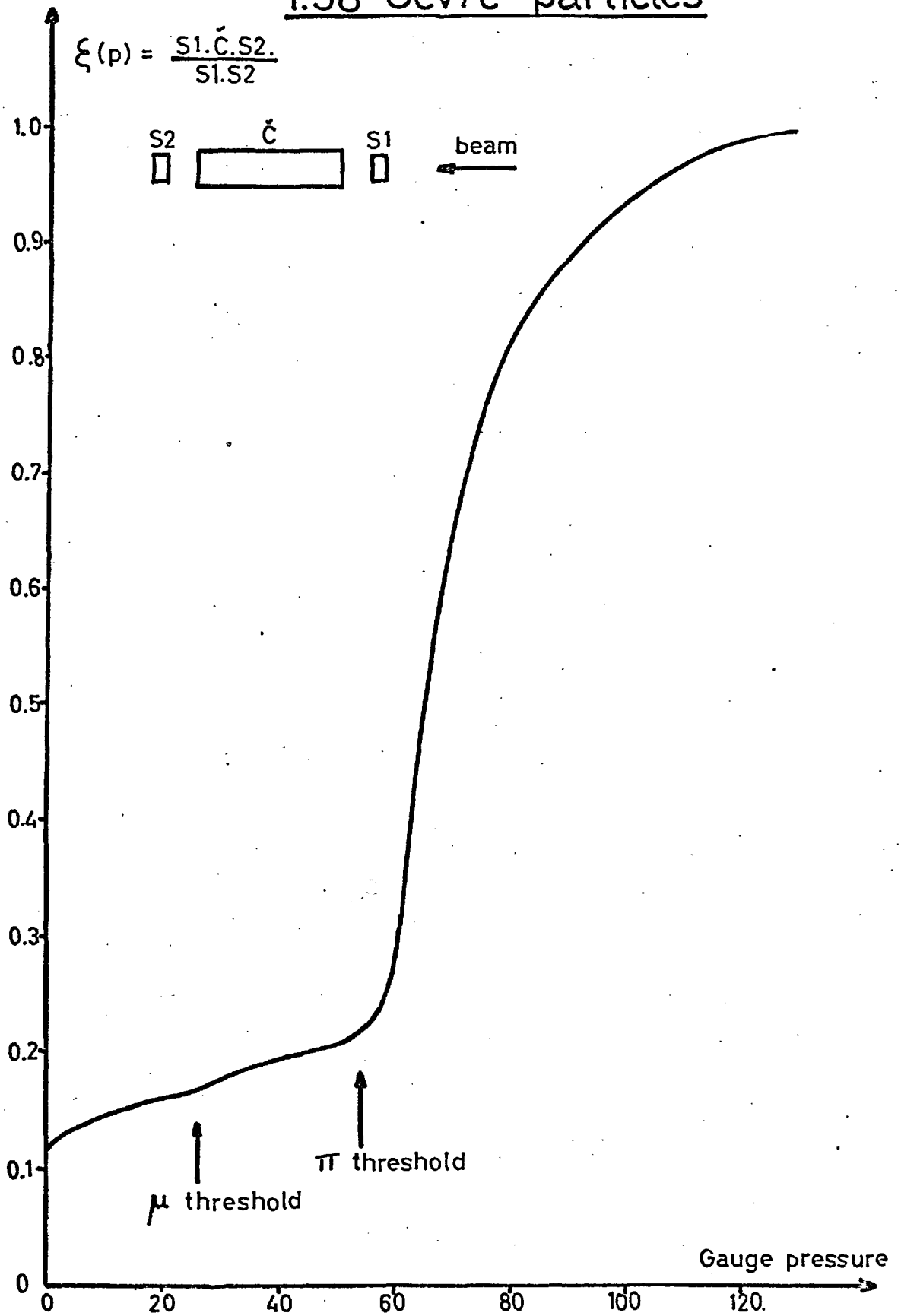

and also for δ-ray production in C by pions and muons (this was found to be negligible). Having a knowledge of the electron excess pressure, and therefore the efficiency for electrons at this point, the corrected $\varepsilon(p)$ value could be used to find the electron fraction. A similar process was adopted for the muons, using a point just below the pion threshold. In this way, the pionic content of the beam was found to be $(78 \pm 4)\%$.

CHAPTER 3

Experimental Design and Procedure

3.1 Principles of the event selection, and description of the apparatus involved

The experimental arrangement which was adopted for the ϕ production experiment is shown in Fig.3.1. It was designed principally by I.U. Rahman, who also designed the electronic logic system which controlled the experimental data-taking.[28] Basically, it consisted of an arrangement of scintillation (and Cerenkov) counters with which events of the type $\pi^- p \rightarrow K^+K^- n$, produced in a liquid hydrogen target, could be electronically selected from events due to other processes, over a small missing-mass range about the ϕ meson mass. When a $K^+K^- n$ event was detected by the apparatus, the electronic logic system caused a photograph to be taken of the tracks of the K^+K^- pair in an optical spark chamber arrangement, and also made measurements of the kinematic parameters of the event. The objective aimed at in the design of this counter arrangement was the maximisation of the number of $\pi p \rightarrow K^+K^- n$ events per beam particle detected near the ϕ threshold by the apparatus, while at the same time the electronic event selection rate due to background processes

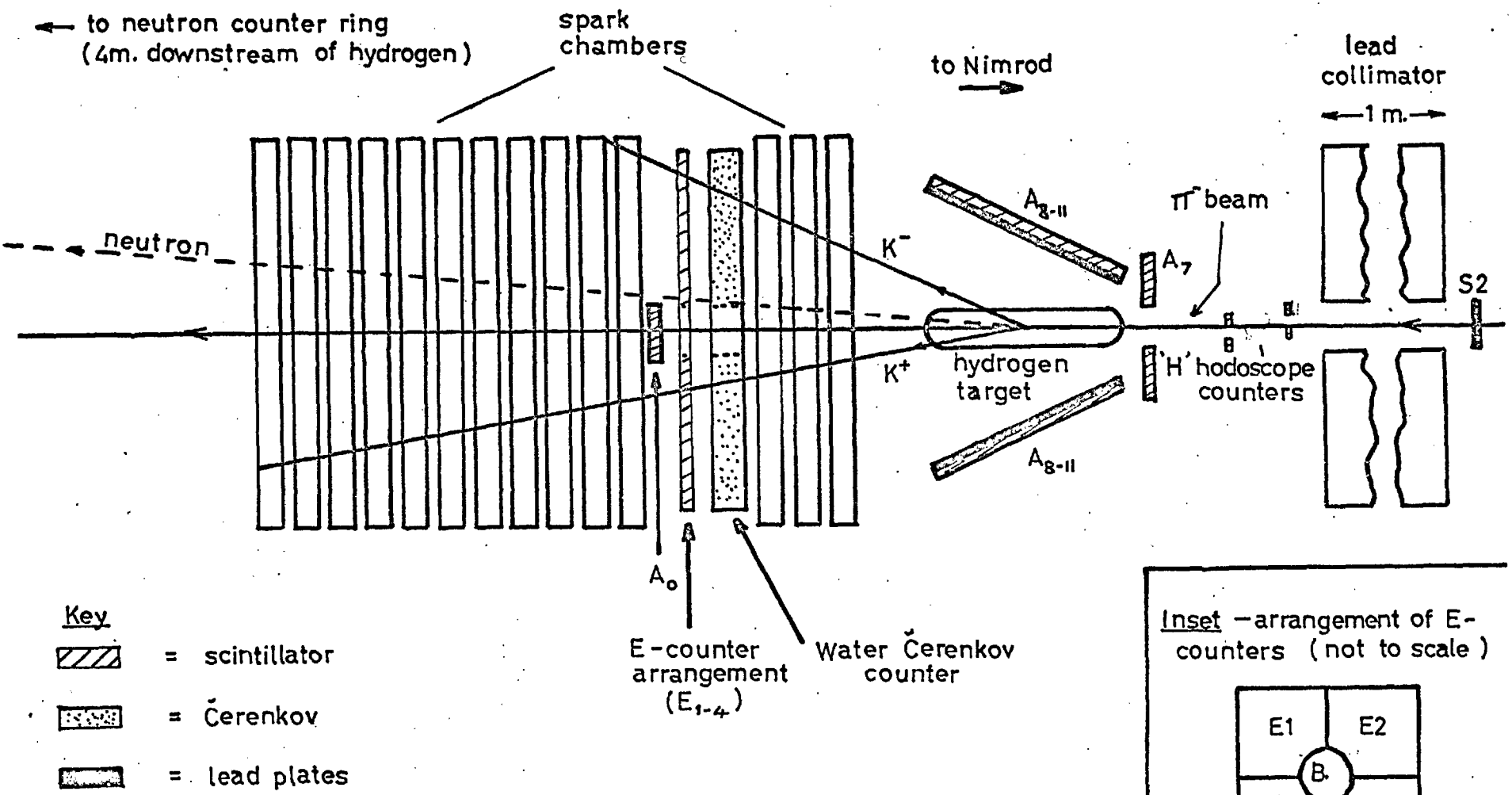

Fig.3.1. Diagram of apparatus

approximately to scale (~1:10)

simulating $\pi p \rightarrow K^+K^-n$ events was kept as low as possible.

The beam entered a target of liquid hydrogen through the counter S_2 (used in the measurement of the neutron time of flight), and the H-counters of the hodoscope. The anti-coincidence counter A_7 just in front of the target had a 6 cm diameter circular hole in it to allow true beam particles to pass through. In the electronic logic system a beam particle (in the i-th hodoscope channel) was defined by the satisfaction of the logic condition $S_2 P \pi_i \bar{A}_7$ $(i = 4,5,6,7)$. Another veto counter A_o, situated in the beam behind the target, could be used to determine whether or not a beam particle had interacted in the target. A beam particle was defined as having interacted in the target, if the logic condition $S_2 P \pi_i \bar{A}_7 \bar{A}_o$ was fulfilled.

In the target, the liquid hydrogen was contained in an 0.01" thick melinex cylinder of length 32.3 cm and diameter 6.5 cm., with its axis coincident with the beam axis. The cylinder was contained in a cylindrical vacuum vessel made of 1/16" thick duralumin, with melinex end-windows, each 0.005" thick. The space between the inner and outer cylinders was filled with several layers of thin aluminium foil, which, in conjunction with the high vacuum that was maintained in this space, thermally insulated the target.

Neutrons from the reaction $\pi^- p \rightarrow K^+ K^- n$ were detected by the ring of six neutron counters described previously, situated 4m downstream of the target, on the beam axis. Each neutron counter consisted of a cylinder of scintillator 30 cm long, 30 cm in diameter, viewed along the (negative) beam direction by a 58 AVP photomultiplier, through a lucite light guide. The neutron counters detected neutrons with angles to the beam between 2.3° and 6.5° in the laboratory frame. The neutron counter face size, and the neutron flight path chosen, ensured that the uncertainty in the missing mass measurement due to the uncertainties in the neutron angle and time of flight measurements, was comparable with the uncertainty in the mass due to the finite beam momentum resolution, while at the same time this choice gave a good solid angle coverage. In front of each neutron counter N_i was a veto counter $A_i (i=1-6)$, covering the neutron counter face, and designed to veto charged particles entering the neutron counter. Detection of a neutral particle (not necessarily a neutron) by the neutron counters was indicated by the condition $(N_1 + N_2 + \ldots + N_6)(\overline{A_1 + A_2 + \ldots + A_6})$ being fulfilled.

70 cm downstream of the target was an arrangement of scintillation counters, consisting of four similar counters (E-counters), each of which was shaped like a square of side

30 cm, with a quarter circle cut out of one edge. They were arranged as shown in Fig.3.1, so that they formed a square of side 60 cm, with a circle of 8 cm diameter cut in the centre to let the beam through. The K^+K^- pair from the $\pi p \rightarrow K^+K^-n$ reaction was detected by a coincidence of any two of these four counters (the kinematics of the reaction was such that it was almost impossible for both kaons to go through the same E-counter). These counters could be made rather small, because the kaons, produced with little transverse momentum, made angles which were usually less than 25° to the beam axis in the laboratory. As a result, the solid angle subtended by these counters at the target could be made small enough to make it very difficult for the reaction $\pi p \rightarrow \pi^+\pi^-n$ to trigger the system, as the opening angle of the $\pi^+\pi^-$ pair from this reaction would be generally $> 60^\circ$. Thus one potentially serious background process was virtually eliminated.

This process, as it happened, was of a type which, whilst it could have been eliminated afterwards by suitable scanning criteria, or kinematic fitting, nevertheless would have increased the camera trigger rate in the data- taking, thereby wasting film, and complicating the subsequent analysis of the photographs. In practice, random coincidences and non-hydrogen events contributed to this type of background.

However, potentially the most serious non-K^+K^-n background process was $\pi^- p \rightarrow \pi^+ \pi^- \pi^0 n$; here the $\pi^+ \pi^-$ pair might have triggered the E-counters, while the π^0 might not have been detected. It was important to reduce this, not only to lower the camera trigger rate, but also because the $\pi^+ \pi^-$ pair could easily simulate a K^+K^- pair in the chambers on the photographs taken; the $\pi^+ \pi^-$ pair would have a vertex in the hydrogen, and a similar opening angle to the K^+K^- pair, so that it could conceivably satisfy the kinematic fit hypothesis $\pi p \rightarrow K^+K^-n$. This meant that a non-$K^+K^-n$ background could contaminate the final K^+K^- mass plot, and the angular distributions.

Two devices to reduce this background (and also backgrounds involving many (>3) final state pions) were therefore incorporated into the counter system.

a) Firstly, a Cerenkov counter (C) was placed immediately in front of the E-counters, between them and the target as shown in Fig.3.1. This was a square of side 60 cm, again with a circular hole in the centre to let the beam through. It was 5 cm thick along the beam axis, and was filled with water, as the Cerenkov medium. This was viewed by twelve 56 AVP photomultipliers, six above it, and six below. The inside walls were painted with white diffusing paint to increase light collection. The advantage of this counter was that it

could considerably reduce background of the type involving fast pions e.g. $\pi^- p \rightarrow \pi^+ \pi^- \pi^0 n$. Since the pions would generally be fast enough to produce Cerenkov light, whilst the vast majority of kaons would not be, using this counter as a veto would cut down these triggers considerably without affecting the K^+K^-n signal.

b) Secondly, a 'box ' of four scintillation counters (A_i, i = 8-11), was placed around as much of the hydrogen target as possible, without shielding any parts of the E-counters from the kaons (see Fig.3.1). The inside face of each counter was lined with a lead sheet, 0.6 cm thick, to form a lead-scintillator sandwich arrangement. The purpose of the lead was to convert the gamma rays from π^0 decay, occurring, for example, in the $\pi^+ \pi^- \pi^0 n$ background, so that these counters in veto would further reduce this background. They would also be effective in vetoeing events where many pions were produced.

In the electronic logic system, a K^+K^- pair was defined by the condition $E_m . E_n . \bar{C} . (\overline{A_8+A_9+A_{10}+A_{11}})$, where m,n =1-4, and $m \neq n$. That is, the K^+K^- pair was defined by a coincidence between any two of the four E-counters, without an associated pulse from the Cerenkov counter, or any of the four counters forming the 'box' surrounding the target.

3.2 The spark chamber arrangement, and the optical system

The spark chambers were used to enable us to investigate, in the scanning process, the cause of the E-counter trigger, and to allow us to measure precisely the directions of the (kaon) tracks. The spark chambers used in this system were all 4-gap modules, with $\frac{1}{4}$" gap thickness, and a useful cross-sectional area of 60 x 60 sq.cm. Their construction and mode of operation have been previously described.[29] Three chambers were placed normal to the beam axis between the target and the Cerenkov counter as shown (Fig.3.1). The kaons passed through little matter before traversing these chambers, so all measurements made on the kaon tracks were made in these first three chambers. Further spark chambers, placed downstream of the A_0 counter, were used to investigate the influence of the fairly considerable amount of matter in the Cerenkov-E-counter system, on the K^+K^-n signal (this is described later).

The chambers were viewed in two directions, which, if the beam axis is taken as the positive x direction, can be considered the negative y, and positive z directions, of a right-handed Cartesian coordinate system. The two views were combined by a mirror system so that they could be photographed by a single camera, the two images produced lying side by side on the film.

The mirror system, designed by J.P. Horsey, is shown in Fig. 3.2. The design employed ensured that the path lengths of the light from the chamber volume to the camera were approximately the same for both views. The camera used, and its associated electronics, are described fully in reference (28). The film used was Ilford Tri-X.

3.3 Electronic event selection and photography - the neutron time of flight spectrum

The reaction $\pi^- p \longrightarrow K^+K^-n$ was finally defined in the electronic logic system by the satisfaction of the condition

$$(S_2 P_{\pi i} \bar{A}_7).\bar{A}_o.(E_m.E_n.\bar{C}.(\overline{A_8+A_9+A_{10}+A_{11}})).((N_1+N_2 \ldots N_6).(\overline{A_1+\ldots A_6}))$$

An important additional constraint on the electronic trigger was that only events having neutron times of flight lying within a certain range were photographed (i.e. a neutron time of flight 'gate' was imposed on the trigger). This was done in order to reduce background on the pictures, and was possible because the K^+K^-n events only occupied a certain time range.

The time of flight of the neutron, t, was determined by measuring, a) the relative delay t_1 between the pulse due to the input pion in S_2, and the pulse due to the neutron in neutron counter N_i; b) the similar delay, t_o, that would result from a particle (produced by the input pion) travelling at the velocity

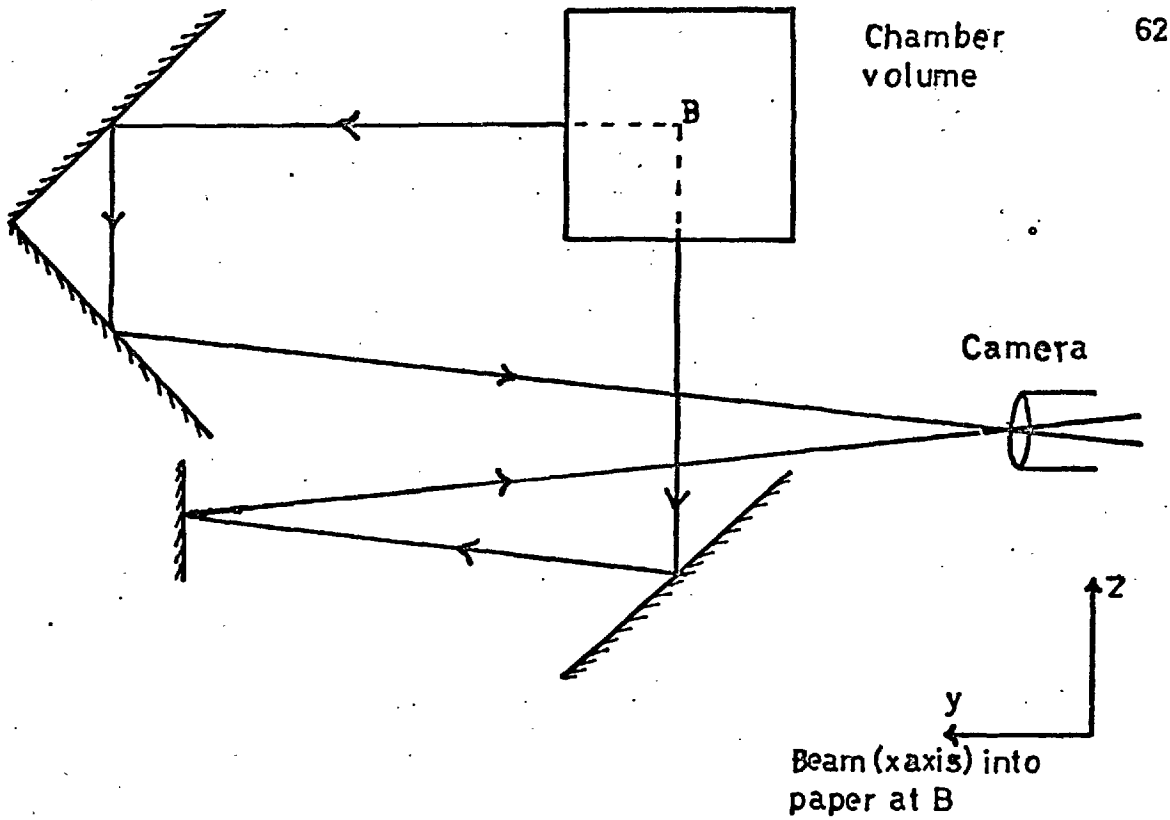

Fig. 3.2. Sketch of mirror system

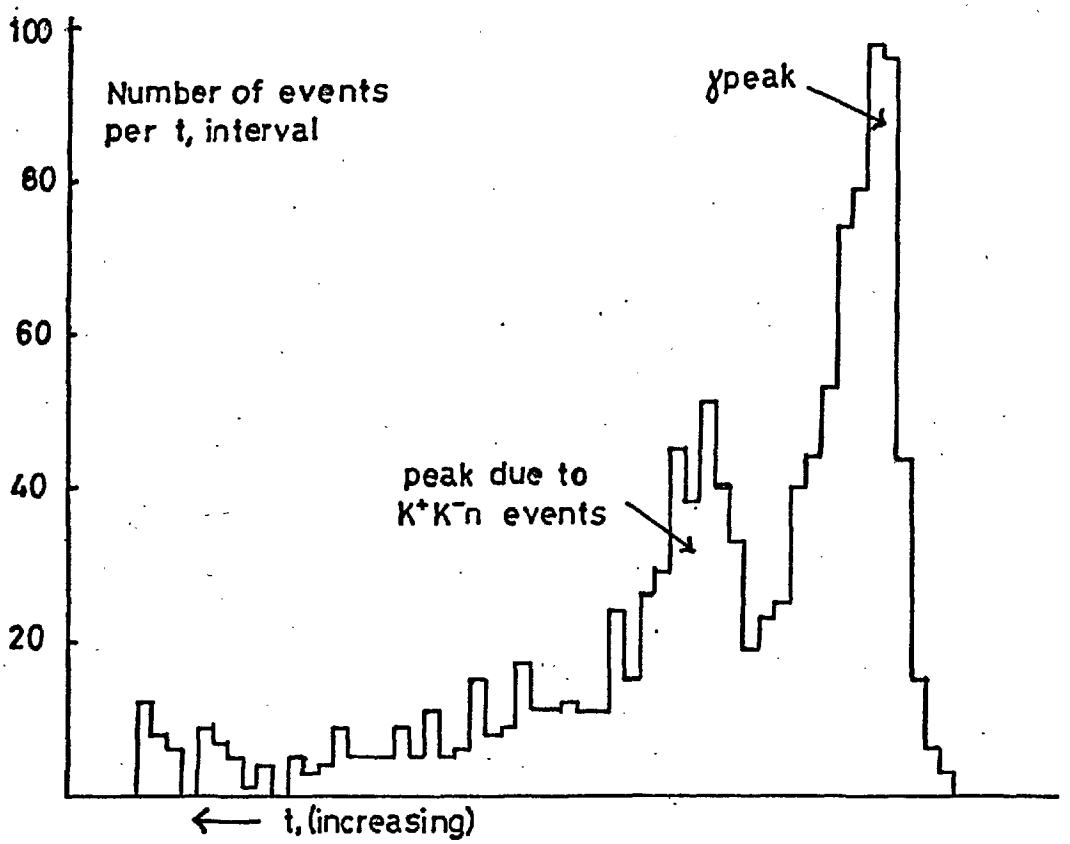

Fig. 3.3. Neutron time of flight spectrum

of light c between the target and N_i, and c) the distance L travelled by the neutron between the points of interaction in the target and N_i.

Then:

$$t = \frac{L}{C} + (t_1 - t_o) \approx t_1 - \text{constant} \qquad \ldots 3.1$$

if we neglect the small lengths of the target and N_i compared to the neutron flight path L, and also the angular spread of neutrons entering N_i. The method of timing used is described in reference (11). A typical neutron time of flight spectrum (frequency of (digitized) t_1, versus t_1) obtained using the (ungated) electronic selection trigger at a momentum just above ϕ threshold, is shown in Fig.3.3. It exhibits a characteristic sharp peak at a time corresponding to that of a particle travelling at the speed of light between the target and N_i; this was produced mainly by gamma rays, and is called a 'γ peak'. There is also a wider, smaller peak at longer times, produced by neutrons from the K^+K^-n reaction; this bump sits on a smoother background. The amount of background in the time range of the K^+K^-n events, is seen to be about the same as the total K^+K^-n signal at this beam momentum, where the amount of K^+K^-n collected was at a maximum.

For the event photography, the neutron time of flight gate

used was set around the K^+K^-n bump. The gate was actually kept rather wide during the electronic data-taking - all neutrons from the K^+K^-n events, and many of the 'γ peak' events, were accepted - but was reduced during the scanning procedure.

When the full trigger condition above was satisfied, the spark chambers were pulsed, and a photograph of the spark chambers taken. Pulsed flash lamps illuminated a fiducial system in each spark chamber view, and digitized information about the event, displayed on Nixie tubes, was also photographed. The information recorded included the hodoscope channel of the input pion, the neutron counter triggered, and the neutron time of flight, for that particular event.

CHAPTER 4

The Monte Carlo and Kinematic Fitting Programmes

4.1 The Monte Carlo Programme

The processes which occur in nature from the initial generation of a $\pi^- p \rightarrow K^+ K^- n$ event to its final detection by the apparatus (or otherwise) can be idealized by a series of choices. Each choice involves the choosing of a value for one of the parameters describing the event, from the probability distribution of that parameter. If the probability distributions are known, and can be expressed mathematically, it is possible to simulate this natural process on a computer. If all the probability distributions are not known, as in this case, the unknown ones can be replaced by a model.

The simulation method used here is the Monte Carlo method. On this method, each choice of a parameter is performed by generating a pseudo-random number from a probability distribution which is identical to that of the parameter. A single event, which involves a series of these choices, then has definite values for the parameters describing it. Whether or not the event will be 'detected' by the apparatus depends on these parameters. By generating many such events by this statistical

process, one effectively performs an integration over all the relevant parameters which takes into account their probability distributions, and the boundary conditions imposed (by the apparatus, etc.). This is precisely what occurs in nature, so that the method can be thought of as a simulation of nature.

The final observed frequency distribution of each parameter (i.e. its original probability distribution suitably 'weighted' during the integration) can then be built up statistically, from the detected events, for those parameters whose original distributions were fixed by the model. The Monte Carlo observed distributions for these parameters can then be compared with the corresponding experimental distributions. Differences between the distributions are then directly attributable to differences between the simulating model and nature. This method of comparing Monte Carlo and experimental results, to test the Monte Carlo model, formed the basis of our experimental analysis.

The Monte Carlo programme used was the slightly modified version of a programme written by Dr. W.G. Jones.[11] The programme was able to generate $\pi^- + p \rightarrow z^0 + n$ events, in which the z^0 system was taken as a Breit-Wigner resonance which decayed into a K^+K^- pair, according to a specified model,

which described the production and decay processes. Various forms of model could be employed. The simplest model used in practice, for example, described the z^0 system as being produced isotropically in the c.m.s., with a production cross-section proportional to the c.m.s. final state momentum, and with the z^0 system decaying isotropically into the K^+K^- pair in its rest frame; more complex models were also used. The programme could also generate $\pi^- p \rightarrow K^+K^- n$ events according to a phase space model.

In the generation the momentum of the input pion was taken from a triangular probability distribution, the full width at half height being that calculated in Appendix 1. The input pion was allowed to interact at any position in the target, all positions being equally probable. Allowance was made for the energy lost by the pion in the hydrogen it had traversed before interacting. It was also allowed to have a small angle to the beam axis.

After generation, the interaction of the final state particles of the event with the apparatus was investigated. A neutron was regarded as detected if its trajectory intersected a section through the centre of the neutron counter perpendicular to the beam axis. This implies that we assumed that the efficiency of the neutron counters was constant for

all neutron energies, and was uniform over the neutron counter faces. These assumptions, however, seemed justified in practice (see section 6.7).

After undergoing Coulomb scattering and energy loss due to ionization in their passage through the target, both kaons were subjected to a series of tests. The programme asked (in the order given) - a) were the kaons likely to go into the Cerenkov counter? b) If they were likely to, did they decay in flight before reaching the counter? c) If they entered the counter without decaying, were they fast enough to veto themselves by producing Cerenkov light? d) If they did not veto themselves, did they stop or interact in the Cerenkov counter?

In events where both kaons emerged from the Cerenkov counter unscathed, the kaons were subjected to scattering and energy loss due to their passage through the counter, then the programme asked e) were the kaons likely to go into the E-counters? f) If they were likely to, did they decay in flight between the Cerenkov and E-counters? g) If they entered the E-counters without decaying, did they stop or interact in the E-counters? h) If they successfully passed through the E-counters, did their (eventual) decay products trigger any of the veto counters in the system?

Events satisfying all these tests - events in which the neutron was detected, in which both kaons emerged from the E-counters unscathed, and where no kaon decay product veto occurred - were classified as OKE events.

4.2 Calculations involved in the Monte Carlo programme - experimental OKE events

This section explains how certain parameters which were used in the Monte Carlo programme were calculated. It is necessary to first digress somewhat to explain the importance of these calculations.

In order to be able to compare experimental and Monte Carlo distributions, and to make a quantitative estimate of the ϕ production cross-section, it was necessary to compare a certain class of Monte Carlo K^+K^-n events with a similar class of experimental events. The purest class which also gave good statistics, contained events satisfying all the tests listed previously i.e. events in the OKE class. At present, the OKE class is a Monte Carlo concept only, and it is necessary to define an experimental OKE event. An experiment event, having satisfied the scanning criteria, and having been fitted satisfactorily to the hypothesis $\pi p \rightarrow K^+K^-n$ in the geometry/kinematics programme, acquired OKE status if a continuation of each kaon track seen in the first 3 chambers, was seen in the spark chambers downstream

of the E-counters. In addition, it was required that any change in direction of the tracks as the kaons traversed the Cerenkov-E-counter system, should be less than 10°. This ensured that the experimental OKE class did not become contaminated with events from another class. For example, an event where a K^{+} stopped in the E-counter, producing a μ^{+} which continued into the downstream chambers, would have been classified in some lower class than OKE by the Monte Carlo programme; under the latter constraint, it would also have been rejected from the experimental OKE class (unless the μ^{+} went into the forward 10° cone, which is unlikely). 10° was used as the cut-off in order not to reject events that had merely suffered a small angle Coulomb scattering in the counter system.

Therefore, certain parameters governing losses of events from the OKE class in the Monte Carlo programme, had to be known as accurately as possible in order to compare quantitatively OKE events from Monte Carlo and experiment. The most important losses of OKE events were due to a) kaons decaying in flight between the target and E-counters; b) kaons stopping in the Cerenkov and E-counters; c) kaons suffering nuclear interactions in the Cerenkov and E-counters.

The parameter governing (a) was simply the kaon lifetime,

which is accurately known. For the calculation of (b) in the programme, the range tables of reference (30) were used. To find the range in composite materials (in our case, the water in the Cerenkov, and the material of the scintillator), the energy loss per g.cm^2 of the composite material, $\frac{1}{\rho}\frac{dE}{dx}\Big|_{comp.}$, was calculated from the tabulated values of $\frac{1}{\rho}\frac{dE}{dx}$ for each element in the composition, using the formula given in reference (30). The range in the composite material was then found from a numerical integration of $\frac{1}{\rho}\frac{dE}{dx}\Big|_{comp.}$.

Data for calculating the effect of (c) was taken from reference (31). The interaction length calculated was for interactions where no charged particle went into the forward 10° cone. This was to allow for the 10° cut-off for Coulomb scattering of OKE events previously mentioned. The cross-section for K^+ interactions (in water and scintillator) was found to be rather small (~ 1/3 geometric) and roughly independent of momentum over our range of kaon momentum (P_k = 300-650 MeV/c). The K^- cross-section, however, was taken as being momentum dependent, varying linearly between ~1.5 geometric at the lowest kaon momentum, to ~0.7 geometric at the highest.

It was estimated that an uncertainty of ~ 4% would

result in the value of the ϕ production cross-section, as a result of the uncertainties involved in the calculations of (a), (b), and (c).

There were many processes involved in the real experiment which were not included in the Monte Carlo simulation, because they were considered independent of the kinematic parameters of the event (in some cases this was an approximation, valid because the effect was small). Instead, the effect of these processes was included in an overall normalization factor at the end. These processes are not described here (owing to some of them demanding a knowledge of the scanning, measuring, and kinematic fitting of the event), but will be considered in section 6.7.

4.3 The kinematic fitting programme

Any event purporting to be $\pi^- p \rightarrow K^+ K^- n$ should be able to satisfy the condition that both energy and momentum must be conserved in the process. A particle i can be specificied by its mass M_i, momentum p_i, and direction, given by the angles θ_i and ϕ_i defined in Fig.4.1. Conservation of energy and momentum can be translated into four equations, three for momentum conservation along each axis, and one for energy conservation.

Fig. 4.1. Definition of angles

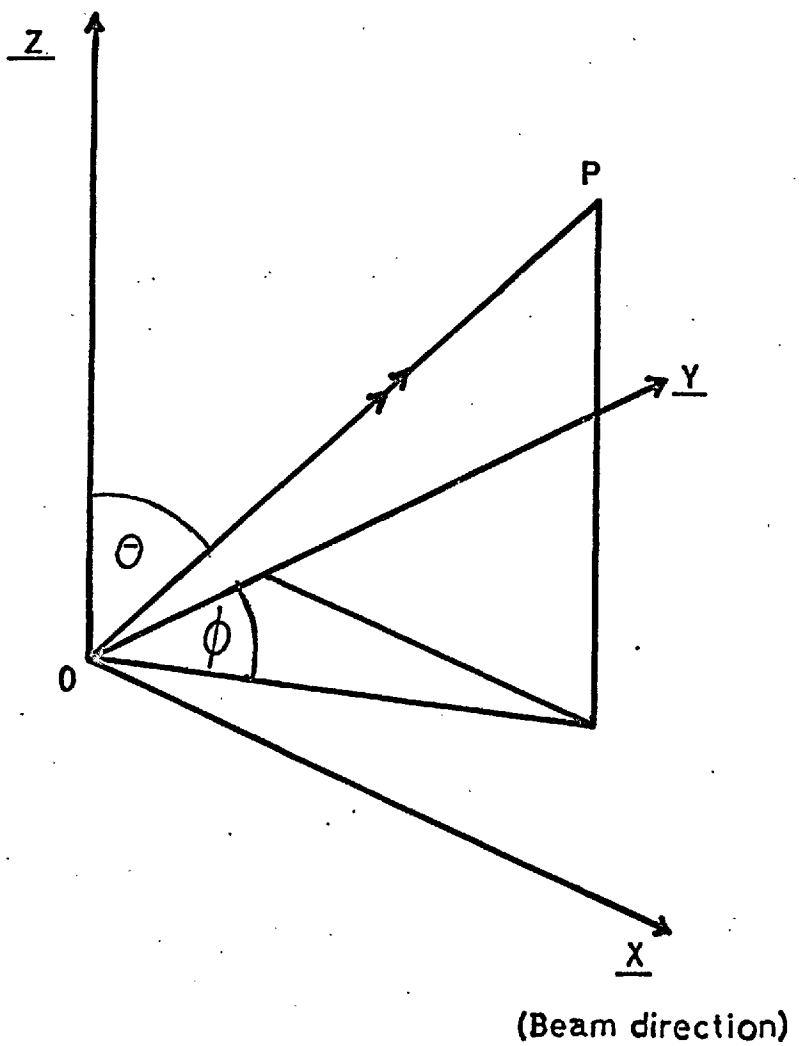

0P = direction of particle

If we work in the laboratory frame -

$$\sum_{i=1}^{4} f_i \, p_i \sin\theta_i \cos\phi_i = 0 \qquad \ldots 4.1$$

$$\sum_{i=1}^{4} f_i \, p_i \sin\theta_i \sin\phi_i = 0 \qquad \ldots 4.2$$

$$\sum_{i=1}^{4} f_i \, p_i \cos\theta_i = 0 \qquad \ldots 4.3$$

$$\sum_{i=1}^{4} f_i \sqrt{(p_i^2 + M_i^2)} - M_p = 0 \qquad \ldots 4.4$$

Index i runs from 1 to 4, since in this process there are four particles (π , n, K^+, K^-) with non-zero momentum in the laboratory frame. f_i is a factor which is -1 for initial state particles, +1 for final state particles; M_p is the proton mass.

In the case of an event where all the parameters are known, these equations will in general not be satisfied. This is because each parameter is subject to errors and uncertainties introduced by the apparatus or measurer. However, statistical methods exist, according to which, if small adjustments are made in a certain way to the <u>measured</u> values of the parameters, the <u>adjusted</u> values of the parameters can be made to satisfy the conservation equations. Furthermore, it can be proved that, using these methods, the values of the

adjusted parameters so calculated, represent the most likely estimates of the true values of these parameters. Such a statistical method (called a fitting process) can be employed whenever there is overdeterminacy i.e. whenever there are more equations linking a set of parameters, than there are unknowns among the parameters. In this case, we can have up to three unknowns before it is no longer possible to subject the parameters to a fitting process. However, the fewer unknowns, the more tightly constrained the system becomes.

The kinematics programme written for use in our experimental analysis was required to fit the measured events to the single hypothesis $\pi^- p \rightarrow K^+ K^- n$. The kinematic information available for each event was the momentum vectors of both the pion and the neutron, and the direction cosines of both kaons (all measured in the laboratory frame). The only unknown quantities were then the momenta of the two kaons, so that the fit in our case was a two-constraint one (number of constraints = number of equations - number of unknowns).

The method of least squares was the statistical method employed as the basis of the kinematic fitting. The mathematical basis of the method is given in Appendix 2.[32] The basic operation performed was the minimization of the

variable

$$\chi^2 = \sum_{i=1}^{10} \frac{(m_i - m_i^{o})^2}{\sigma_i^2}$$

under energy and momentum constraints (i.e. equations 4.1-4.4). Index i runs over all the measured parameters. m_i^{o} is the initial measured value of variable i, while m_i is the adjusted value obtained when χ^2 is minimised and the constraint equations satisfied. σ_i^2 is the estimated variance of the variable i. Since the constraint equations are non-linear, the minimisation process was iterative. The initial errors σ_i on the measured variables were assumed uncorrelated. However, correlations did exist, and because of this the errors on the corrected variables could generally be reduced from their initial estimated values (see Appendix 2).

The least squares method demands that the variables used in the fit should be normally distributed. The θ and ϕ angles (see Fig.4.1) were taken as the normal variables which described the direction of each particle (in the frame specified). The reason for this choice was the collimation in the forward x direction of the initial and all the final state particles, because of the proximity of the reaction threshold. As a result, this choice ensured that small changes in a particle's direction did not cause wild variations

in its ϕ value. (This might have occurred if the z axis of Fig.4.1 had been taken as the beam direction). The momentum magnitude of each particle was also considered as normally distributed, with the exception of the neutron, where the time of flight was taken as normally distributed instead.[11] The main approximations involved in this formalism were that, in practice, θ and ϕ for the neutron were not really distributed normally, since the distributions of these parameters were limited by the finite dimensions of the neutron counter. Also, the input pion momentum was distributed triangularly rather than gaussianly, as discussed in Appendix 1. (The position of the event vertex in the hydrogen could be calculated from the kaon tracks on the event photograph, so that the effect on this momentum distribution of the pion energy loss in the target before interaction could be eliminated).

4.4 Testing the kinematics programme with the Monte Carlo programme

As stated in the previous section, the kinematic parameters of the event would not all be normally distributed in practice. However, if the parameters were all normally distributed, the resulting fitted events would be required to satisfy certain theoretical conditions. This fact was used to test that the kinematics programme was working correctly, using events generated by the Monte Carlo programme.

The test was carried out by first adding a small deviation to the <u>true</u> value of each of the (ten) 'measured' kinematic parameters of a Monte Carlo event. The deviation was, in each case, chosen randomly from a normal distribution of zero mean. The event, so 'smeared', was then fitted to $\pi^- p \rightarrow K^+ K^- n$ by the kinematics programme, in the normal 2-constraint fit. The variance of the normal distribution used to 'smear' the value of the parameter i, was the same as the variance for parameter i used in the fitting process. Because these variances were made equal, the events fitted in this way had to satisfy the following theoretical requirements:

1) The χ^2 distribution of the fitted events should be the same as the theoretical χ^2 curve for two degrees of freedom (this implied also that the mean value of χ^2 for the fitted events should be 2).

2) The 'stretch functions' for the measured parameters, defined as $S(m_i) = \dfrac{m_i - m_i^o}{\sigma(m_i - m_i^o)}$, should be normally distributed, with unit variance and zero mean.

3) The variance $\sigma^2(m_i)$ on the i-th <u>fitted</u> parameter, and the variance $\sigma^2(m_i - m_i^o)$ on the correction $(m_i - m_i^o)$ to that unfitted parameter, (both calculated during the fit),

should be related to the original estimated variance $\sigma^2(m_i^o)$ by the relation

$$\sigma^2(m_i^o) = \sigma^2(m_i) + \sigma^2(m_i - m_i^o) \qquad \ldots 4.5$$

(this is a special case of equation A2.21)

The conditions were found to be well satisfied by the fitted Monte Carlo events.

4.5 Use of the Monte Carlo and kinematics programmes to simulate the experimental fits

The last section of this chapter describes how the Monte Carlo programme was used in conjunction with the kinematics programme to complete the Monte Carlo simulation of the experimental event which fitted K^+K^-n. So far only the 'collection' of the Monte Carlo event by the apparatus has been described. To complete the simulation, the procedure of the last section was repeated, in a modified form.

The Monte Carlo event was now made to simulate an experimental event exactly, by introducing small deviations into the true values of the parameters of the Monte Carlo event, in the same way as these deviations were introduced into the true parameters of the experimental event, due to the apparatus only being able to measure to a certain accuracy (i.e. the resolution of the apparatus was applied to the Monte Carlo event before it was fitted to $\pi p \rightarrow K^+K^-n$). Thus, in the

fit of a Monte Carlo event, the estimates of the neutron's θ and ϕ angles were taken to be the θ and ϕ angles of the centre of the neutron counter which had been triggered. Similarly, the estimate of the pion momentum at the front of the target was taken to be the central momentum of the particular hodoscope channel concerned. Normally distributed deviations were introduced, in a random way, into the (true) neutron time of flight, and into the (true) θ and ϕ angles of the pion and each kaon. The variance of the distribution used in the 'smearing' of the i-th normally distributed parameter, was the same as the variance used for this parameter in the fitting process.

The Monte Carlo events fitted in this way in fact differed only slightly from the theoretical expectations of section 4.4.

In all the later comparisons of Monte Carlo and experimental results made during the experimental analysis, the effect of the resolution of the apparatus was applied to the Monte Carlo OKE events, in the manner described above.

The normal variances (and their estimated accuracies) used in the above fitting process, are given in Table 4.1. These values were also the ones used in the fitting of the experimental events. The estimate of the neutron time of flight variance was taken from reference (11). The variance of the

kaon angles was determined mainly by the measuring accuracy attainable on the scanning table, and that of the pion angles by the divergence of the beam. Reasonable variances were assumed for the non-normally distributed parameters; the exact values used for these were not very critical, however, since small changes in them would affect the Monte Carlo and experimental results in the same way.

Table 4.1

Parameter name	Standard deviation	Estimated Accuracy
Neutron time of flight	0.83 nsec	10%
Kaon θ and ϕ angles	0.015 rads†	~20%
Pion θ and ϕ angles	0.008 rads	~20%
Pion momentum*	4.5 MeV/c	
Neutron θ and ϕ angles*	0.025 rads	

* (normal distribution only approximates to the true distribution)

† see section 6.2 for the calculation of this number.

CHAPTER 5

The Response of the Apparatus

Before investigating the response to be expected from the apparatus, it is necessary to first define certain parameters. These definitions follow below.

5.1 Definition of parameters used

We studied the system

$$\pi^- + p \longrightarrow z^o + n$$

where the z^o system was comprised of, or decayed into, a K^+K^- pair. The situation in the overall centre of mass system (c.m.s.) is shown in Fig.5.1(a). The direction of the z^o system in this frame was specified by the angles θ^* and ϕ^*. The direction of the neutron was then given by

$$\theta^*_n = \pi - \theta^* \qquad \ldots 5.1$$

$$\phi^*_n = \pi + \phi^* \qquad \ldots 5.2$$

p^* was the final state momentum (of both the neutron and the z^o system) in this frame.

The kinematic variables of the K^+K^- pair were defined in the rest frame of the z^o system. As shown in Fig.5.1(b), p_ϕ, θ_ϕ, ϕ_ϕ, defined the momentum vector in this frame of the kaon which was the faster in the laboratory. In the diagram, the $\hat{\underline{x}}'$ direction is the input pion direction, and

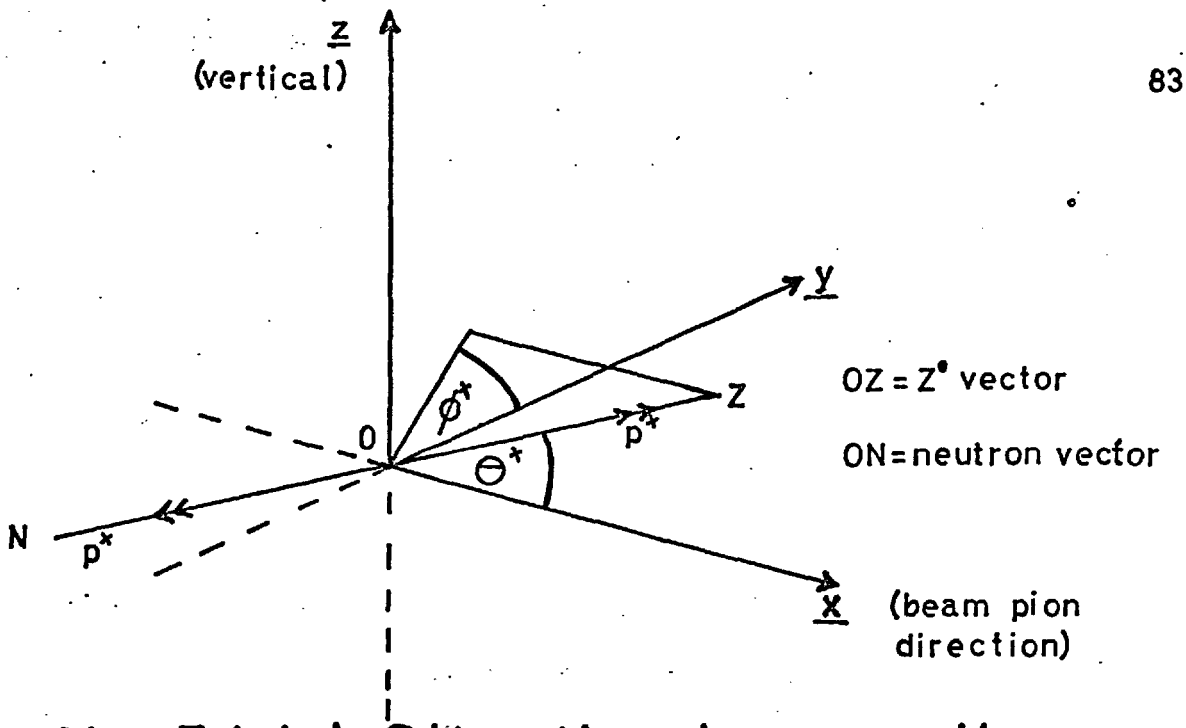

Fig. 5.1. (a) Situation in overall Centre of Mass System

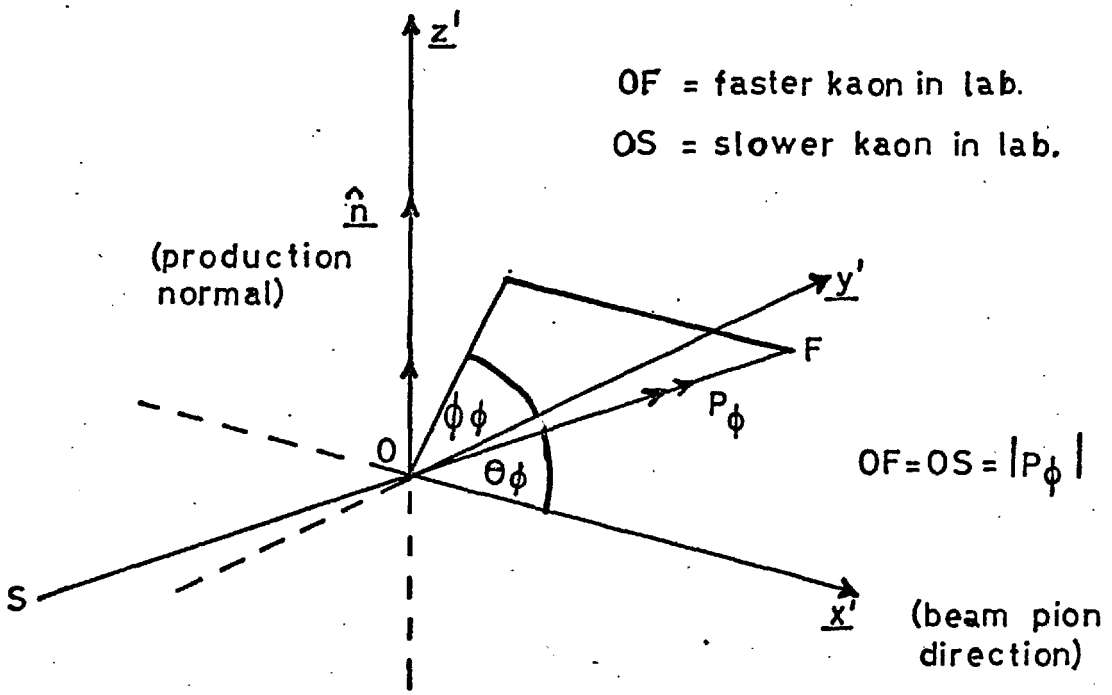

Fig. 5.1. (b) Kaon angles in z^0 rest frame

the $\hat{\underline{n}}$ direction (along the $\underline{z}'$ axis) is the normal to the production plane. The angles θ_ϕ, ϕ_ϕ were then defined by

$$\cos\ \theta_\phi = \frac{\hat{\underline{x}}' \cdot \underline{p_k}}{|p_k|} \qquad \ldots 5.3$$

$$\sin\ \phi_\phi = \frac{(\hat{\underline{x}}' \times \hat{\underline{n}}) \cdot (\hat{\underline{x}}' \times \underline{p_k})}{|\hat{\underline{x}}' \times \underline{p_k}|} \qquad \ldots 5.4$$

$$\cos\ \phi_\phi = \frac{\hat{\underline{n}} \cdot (\hat{\underline{x}}' \times \underline{p_k})}{|\hat{\underline{x}}' \times \underline{p_k}|} \qquad \ldots 5.5$$

These definitions were taken from reference (33). It can be shown that ϕ_ϕ is identical with the Treiman-Yang angle.[33]

The faster kaon was chosen in this definition just because it was necessary to have some way of differentiating between the two kaons; the usual method of distinguishing the kaons by their charge could not be used, as the kaon charge was not detected in this experiment. The faster kaon in the laboratory corresponded to the kaon that went forward in the dikaon rest frame. Therefore the $\cos\theta_\phi$ distribution ran only from $\theta_\phi = 0 \rightarrow \pi/2$, whereas the true range of θ_ϕ allowed for each kaon was $0 \rightarrow \pi$. The faster kaon was

equally likely to be K^+ or K^-, so the distribution obtained for $\cos\theta_\phi$ was effectively a distribution of $\cos\theta_\phi$ running from +1 to -1, which had been 'folded' upon itself about the $\theta_\phi = \pi/2$ point.

In the case where the z^o system decays into a K^+K^- pair via strong interactions, no information is lost as a result of this folding process, as the application of the parity operator P to the strong decay process $z^o \rightarrow K^+ + K^-$ interchanges the directions of the K^+ and K^- i.e. $\cos\theta_\phi \longrightarrow -\cos\theta_\phi$, $\phi_\phi \rightarrow \pi + \phi_\phi$. From parity conservation in the decay one therefore obtains the relation

$$W(\cos\theta_\phi, \phi_\phi) = W(-\cos\theta_\phi, \pi + \phi_\phi) \qquad \ldots 5.6$$

($W(\cos\theta_\phi, \phi_\phi) = \partial\sigma / \partial(\cos\theta_\phi, \phi_\phi)$, is the decay angular distribution).

5.2 The role played by the neutron counters in determining the response of the apparatus

As discussed in Chapter 1, the role played by the neutron counters in this experiment, as in others performed by this group, is of fundamental importance. The neutron counters, together with the beam counters, can be considered to form a 'missing-mass spectrometer' arrangement, since the detection of the pion and neutron from the reaction

$$\pi^- + p \longrightarrow z^o + n$$

by these counters, enables us to study the mass spectrum of the z^0 system. The experiment described here, has gone further, and placed demands on the 'missing-mass' system as well, namely, that it should consist of a K^+K^- pair. However, it turns out that this extra constraint has only a small effect on the basic response of the apparatus due to the neutron counters. This response, and the biases imposed on the experimental (and Monte Carlo) distributions as a result of it, are considered below.

For a given input pion momentum (p_π), and a given mass (M_z) of the z^0 system, the c.m.s. final state momentum (p^*) is completely specified. This can be seen from –

$$E_c^2 = M_p^2 + M_\pi^2 + 2M_p\sqrt{(M_\pi^2 + p_\pi^2)} \qquad \ldots 5.7$$

$$E_c = \sqrt{(M_n^2 + p^{*2})} + \sqrt{(M_z^2 + p^{*2})} \qquad \ldots 5.8$$

where E_c is the c.m.s. energy, and M_p, M_n, M_π are the proton, neutron, and pion masses, respectively.

i.e. $p^* = f(p_\pi, M_z)$ only.

A relation also exists between p^*, θ^*_n, and θ_n, where θ_n is the polar angle of the neutron in the laboratory. A Lorentz transformation of the neutron's momentum vector from the c.m.s. to the laboratory gives –

$$p_n \sin \theta_n = p^* \sin \theta^*_n \qquad \ldots 5.9$$

$$p_n \cos \theta_n = \gamma_c (p^* \cos \theta^*_n + \beta_c E^*) \qquad \ldots 5.10$$

where p_n is the neutron laboratory momentum, β_c is the c.m.s. velocity in the laboratory, and $\gamma_c = 1/\sqrt{(1-\beta_c^2)}$.

Eliminating p_n , we get a relation between θ_n , θ^*_n , and p^*

$$\tan \theta_n = \frac{\sin \theta^*_n}{\gamma_c(\cos \theta^*_n + \beta_c E^*/p^*)} \qquad \ldots 5.11$$

Curves of θ^*_n against p^* for fixed θ_n values are shown in Fig.5.2. The two curves shown are for values of θ_n which correspond to the θ_n values of the inner and outer extremes of the neutron counters (neutron flight path = 4 m.). Only neutrons which fall inside the region bounded by the two curves can be accepted by the neutron counters.

If the production process is assumed isotropic in the c.m.s., then

$$\frac{\partial \sigma}{\partial(\cos \theta^*_n) . \partial \varphi^*_n} = \text{constant} \qquad \ldots 5.12$$

If we then make the approximation of complete azimuthal coverage by the neutron counters, the collection efficiency (ε)

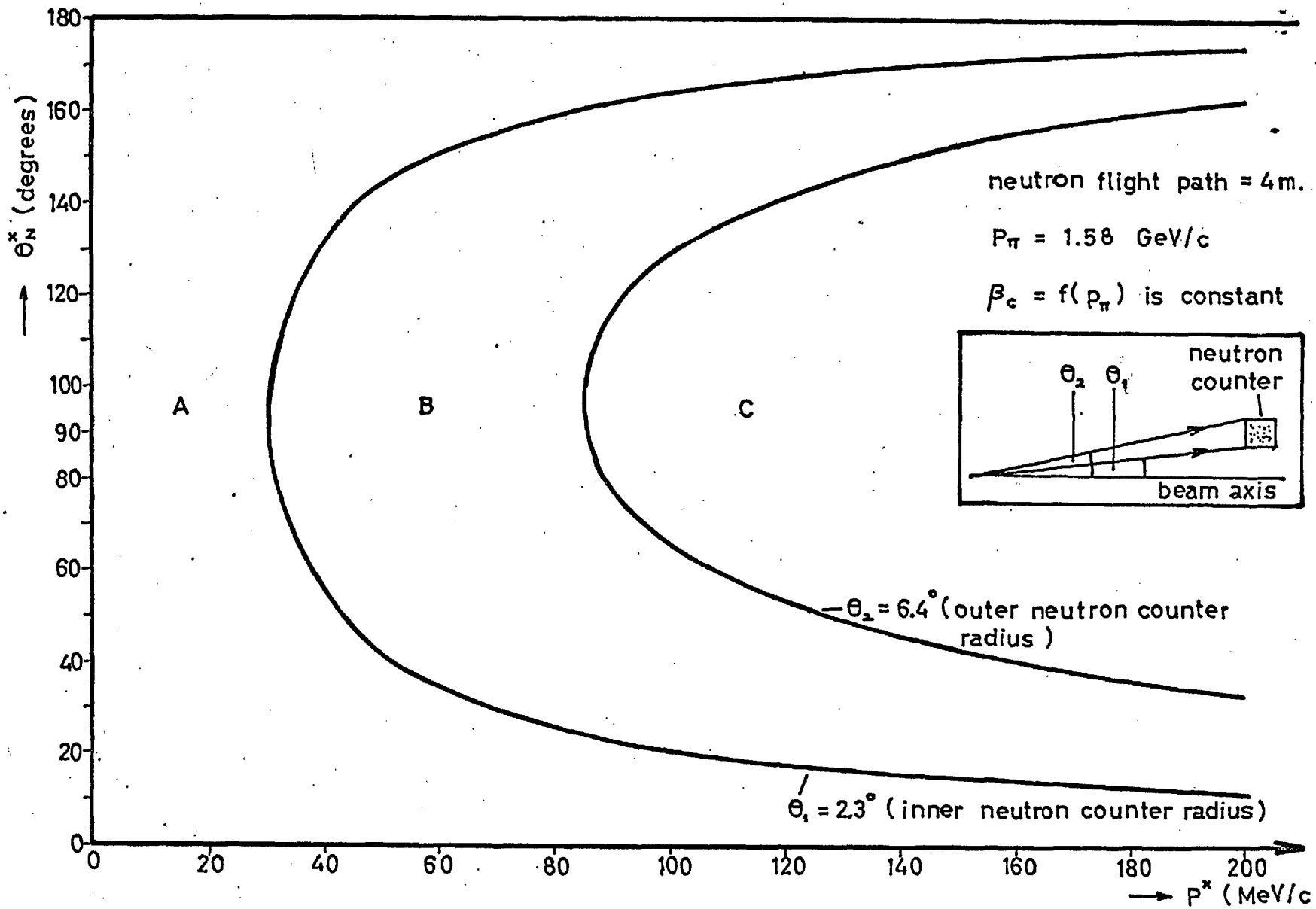

Fig. 5.2. θ_N^* versus P^* plot.

for neutrons of momentum p* depends upon the range of θ^*_n : ($\theta^*_1 < \theta^*_n < \theta^*_2$) collected by the neutron counters at that particular p* value.

$$\varepsilon\,(p^*) = \tfrac{1}{2} \int_{\theta^*_1}^{\theta^*_2} d\,(\cos\ \theta^*_n) \qquad \ldots\ 5.13$$

The collection efficiency as a function of p* is plotted in Fig.5.3(a), using the θ^*_n v p* plots to obtain the allowed θ^*_n range at each p*.

If p_π is fixed, $p^* = f(M_z)$ only. The mass response of the apparatus at that particular p_π value is then defined as the collection efficiency as a function of M_z, $\varepsilon(M_z)$, for that p_π. Curves of $\varepsilon(M_z)$ v M_z for various p_π values are plotted in Fig.5.4.

The actual number of neutrons (dN) associated with z^o masses in the range $M_z \rightarrow M_z + dM_z$ which are collected per beam pion (called the 'yield'), is then related to the production cross-section $d\sigma$ and the mass response by

$$dN \propto \varepsilon(M_z) . \frac{\partial\sigma}{\partial M_z} . dM_z \qquad \ldots\ 5.14$$

Using Fig.5.4, it is instructive to consider now what happens to a <u>fixed mass</u> (or, strictly, an infinitesimal mass range dM_z centred on this fixed mass) as we raise p_π

Fig. 5.3(a). Collection efficiency v. P^*

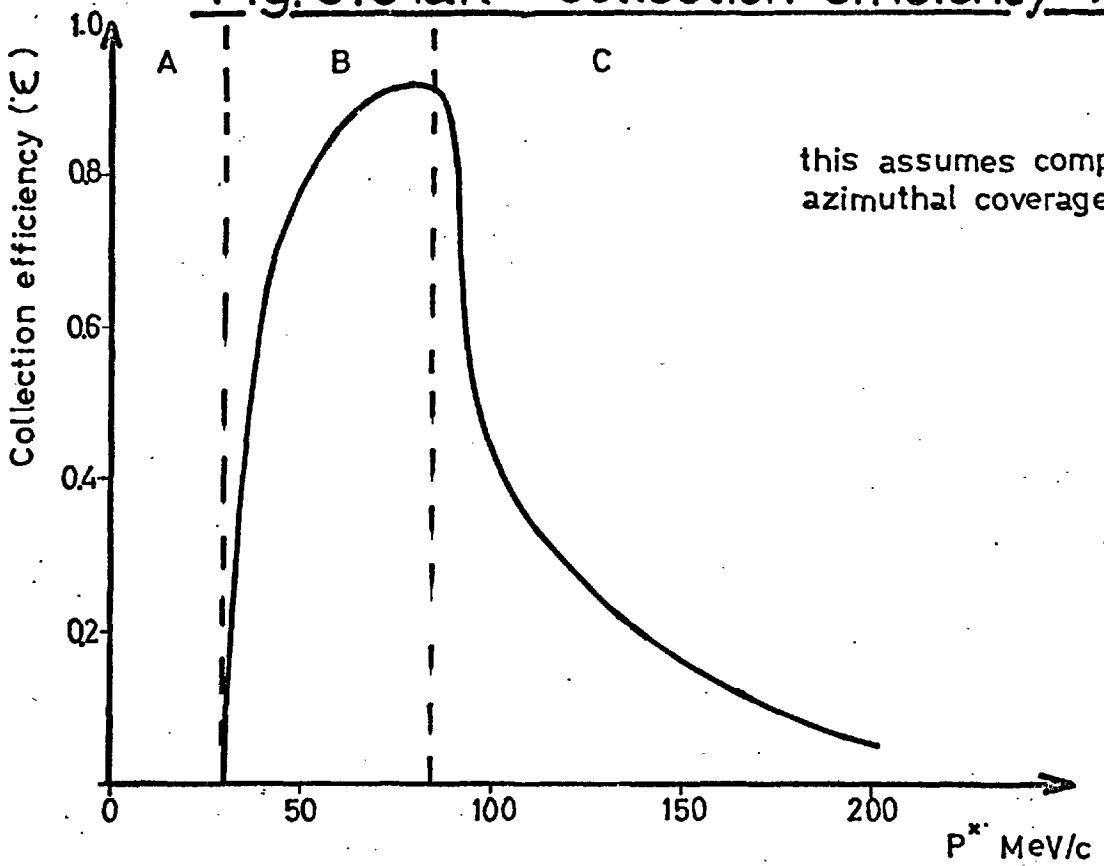

Fig. 5.3(b). Number of neutrons collected per pion, v. P_π.

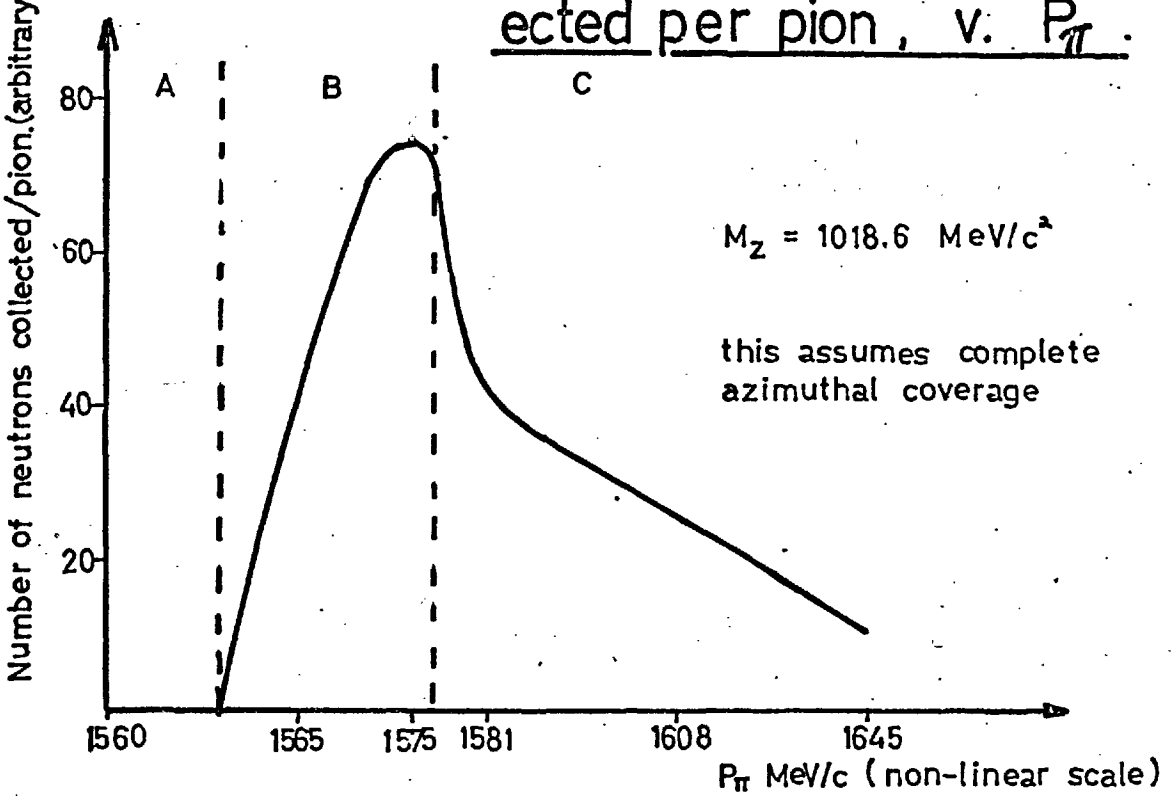

Fig. 5.4. Mass Response curves for different P_π values

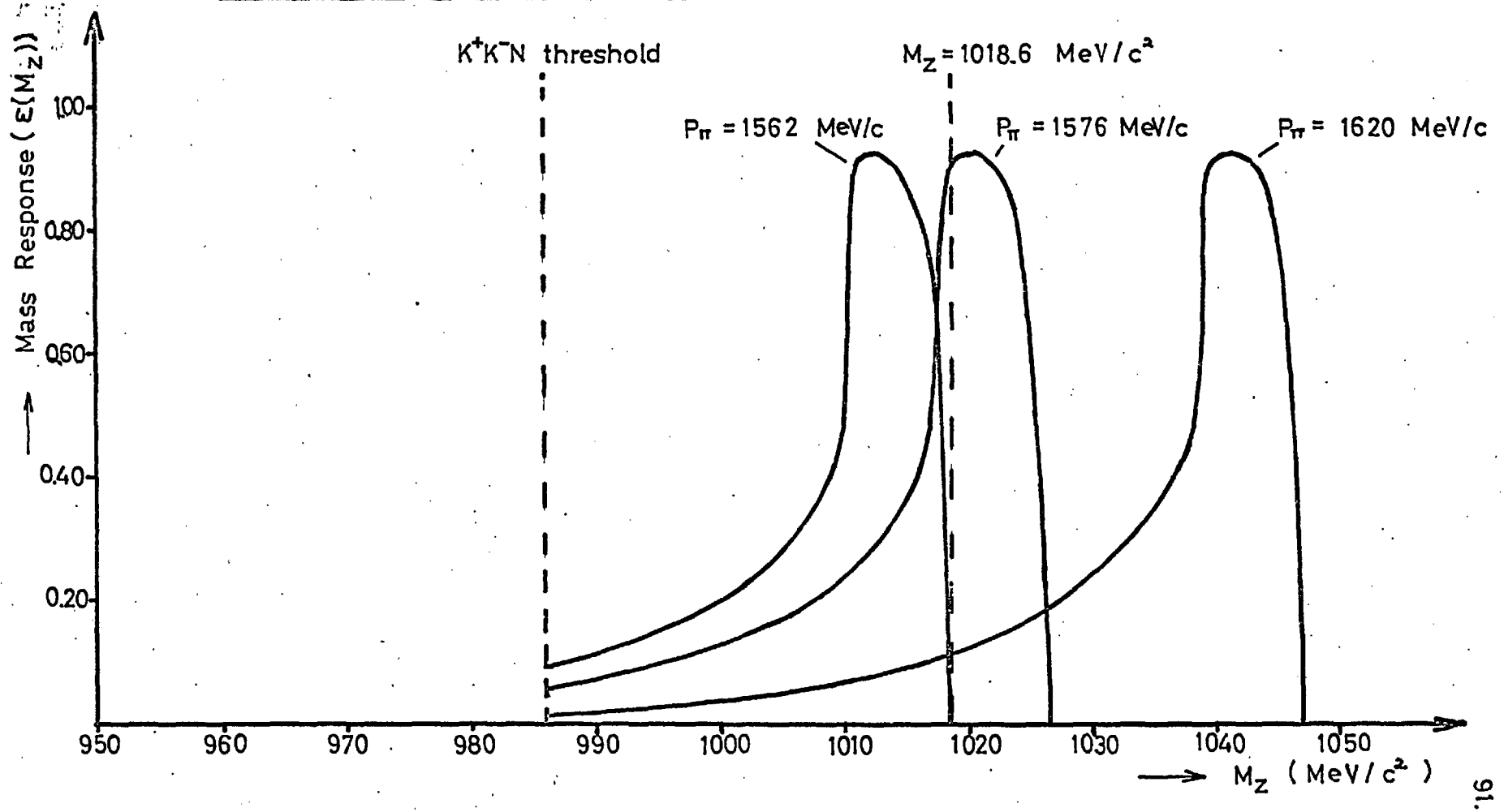

from the threshold value. (In what follows it has been assumed for simplicity that $\partial\sigma/\partial M_z$ is constant over the p_π range considered, so that the yield $dN \propto \varepsilon(M_z).dM_z$ only. In practice it is more likely that $\partial\sigma/\partial M_z = f\ (p_\pi\ ,\ M_z)$, but as $\varepsilon(M_z)$ is generally the more rapidly-varying function of the two over our p* range, the conclusions arrived at below hold qualitatively in general).

For a mass of 1018.6 MeV/c^2, p* is < 30 MeV/c if 1560 MeV/c < p_π < 1562 MeV/c, and we are in region A of the θ^*_n v p* plot of Fig.5.2. None of the neutrons associated with events having this z^o mass has enough transverse momentum to get into the neutron counters, and all neutrons go into the hole at the centre of the neutron counter annulus. The yield of neutrons (dN) is therefore zero in this region. (see curve for p_π = 1562 MeV/c in Fig.5.4).

If we raise p_π we reach region B of the θ^*_n v p* plot (30 MeV/c < p* < 85 MeV/c). In this region, most of the neutrons produced are collected, though those with very high, or very low, θ^*_n values still go into the hole. The observed production angular distribution ($\partial\sigma\ /\partial(\cos\ \theta^*)$) (isotropic but for the biases) therefore appears fairly flat over a wide region here. As seen in the curve for p_π = 1576 MeV/c in Fig.5.4, the yield of neutrons reaches

a maximum in this region, at ~ 1576 MeV/c, ~ 16 MeV/c above threshold ($p_\pi = 1560$ MeV/c) for this mass.

At still higher p_π values ($p_\pi > 1580$ MeV/c, $p^* > 85$ MeV/c) we reach region C. In this region, neutrons with $\theta^*_n \sim \pi/2$ have enough transverse momentum to clear the neutron counters on the outside of the annulus. As a result, the observed production angular distribution splits into two peaks in this region, one composed of neutrons going forwards in the c.m.s., the other composed of neutrons going backwards. This represents a serious bias at high p^* values. As a consequence of the two small ranges of θ^*_n collected, the yield also falls off rapidly in this region (see curve for $p_\pi = 1620$ MeV/c in Fig.5.4).

The above discussion considers the yield associated with a fixed M_z only. However, the <u>total</u> yield of neutrons at any given p_π is given by an integration over the mass response curve for that p_π i.e. $N \propto \int \varepsilon(M_z) . \partial\sigma/\partial M_z . dM_z$. ($\partial\sigma / \partial M_z$ need not necessarily be constant now). The mass response at a particular p_π is seen to be sharply peaked (full width half height ~ 9 MeV/c^2). The mass response over the whole mass range covered can, however, be made (more or less) uniform, by summing together the (normalized) data from adjacent p_π blocks (this technique was used in the

analysis of the present experiment). Any structure which then appears in the plot of total yield as a function of p_π, is then due to structure in the z^o mass spectrum. Examination of the yield v p_π plot is therefore a good way of seeing any (fairly narrow) resonance in the mass range of the z^o system covered. This is illustrated in Fig.5.3(b), where the yield v p_π plot is drawn for the extreme case of a zero width resonance (M_z = 1018.6 MeV/c^2), superimposed on an infinitesimal non-resonant background; the yield as a function of p_π is then just that due to a fixed mass. (Fig.5.3(b) was obtained from Fig.5.3(a), using the fact that $p^* = f(p_\pi)$ only for fixed M_z. Fig. 5.3(b) includes a dependence of the production cross-section on p^* - it assumes $\sigma \propto p^*$, a good approximation near threshold (see section 1.3)).

5.3 Examples of the Monte Carlo distributions

As an illustration of the points discussed in the last section, and in order to introduce some of the distributions used in the analysis, some examples of the Monte Carlo distributions for the ϕ meson (M_ϕ = 1018.5 MeV/c^2, width = 4 MeV/c^2), and for K^+K^-n phase space, are shown in Figs.5.5 and 5.6. The Monte Carlo OKE events were generated, for the ϕ, according to the 'simple' ϕ model discussed in section 4.1, and according

Fig. 5. 5. Monte Carlo distributions for the ϕ

—— = 1576 MeV/c histogram

- - - - = 1620 MeV/c histogram

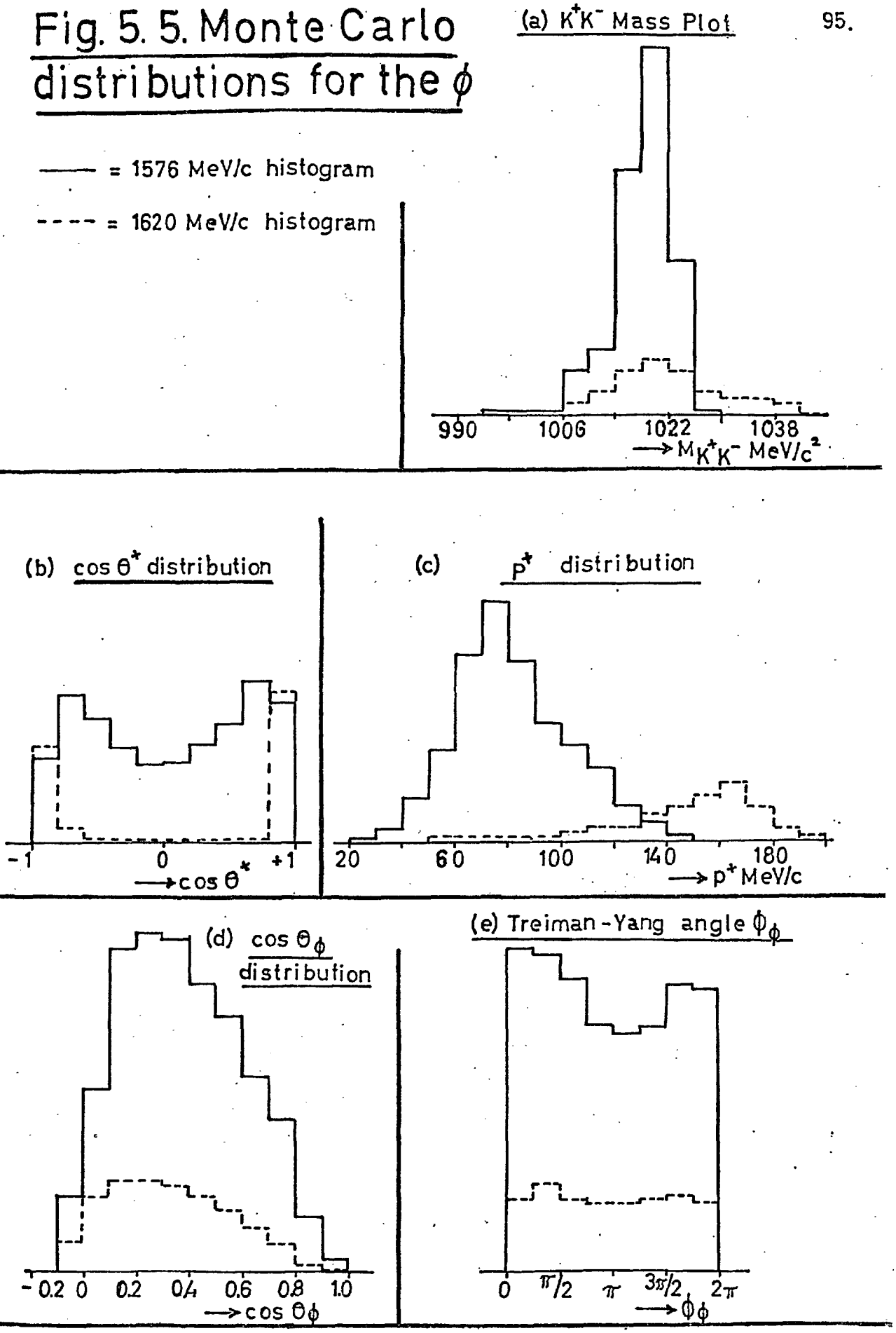

Fig. 5.6. Monte Carlo distributions for K^+K^-n phase space events

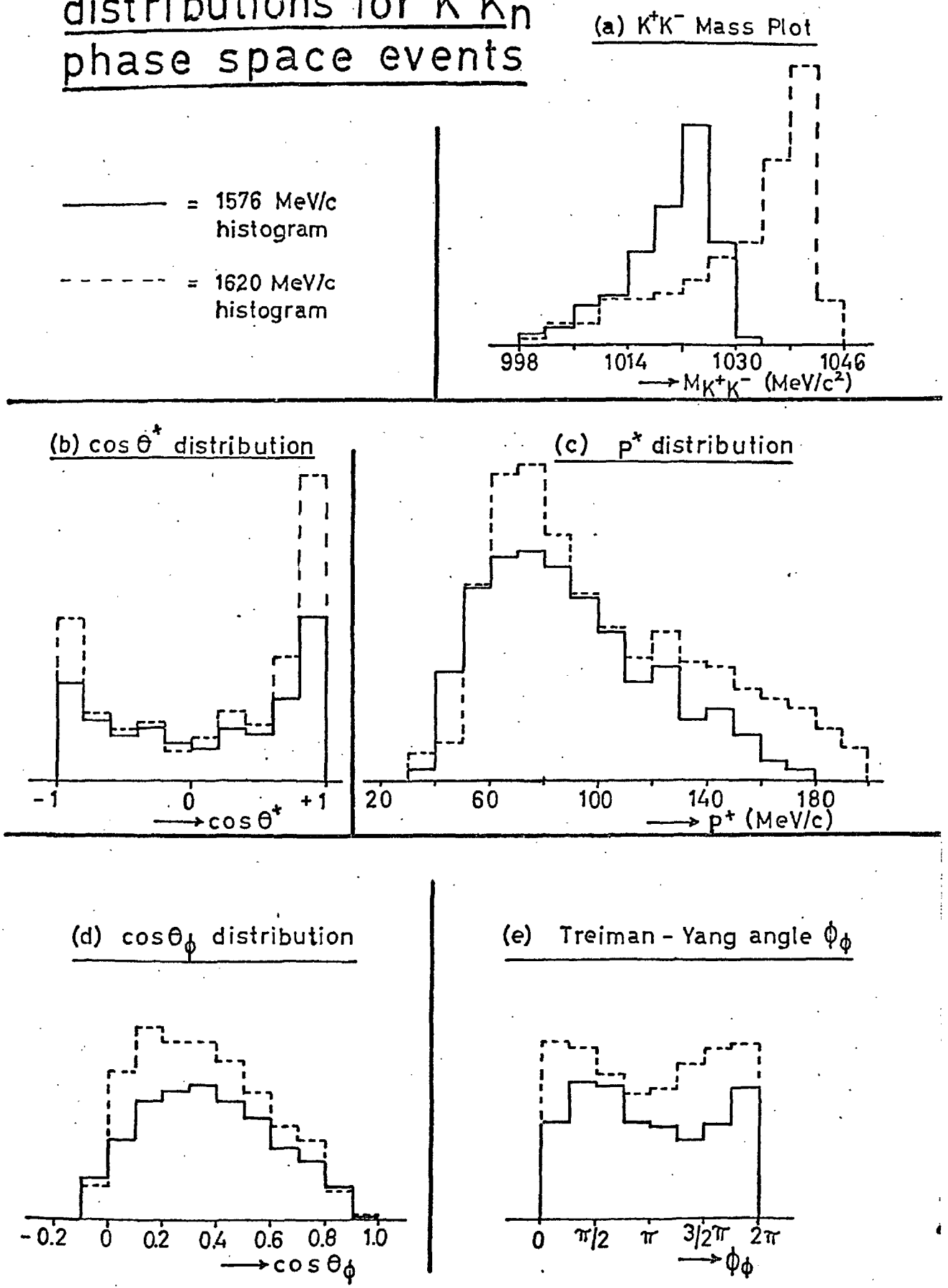

to the phase space model for the K^+K^-n phase space events. All events underwent the process described in section 4.5 to include the resolution of the apparatus, and all histograms were normalized to the same number of (Monte Carlo) beam pions. Two beam momenta, 1576 MeV/c and 1620 MeV/c, are considered, to illustrate how the biases change with beam momentum.

We consider first the distributions concerned with the production processes.

For the ϕ, the main changes that occur in going from p_π = 1576 MeV/c, to p_π = 1620 MeV/c, are, a) the yield falls to about a quarter of its maximum value (occurring at ~ 1576 MeV/c); b) the (observed) production angular distribution, initially fairly flat, splits into two peaks; c) a higher range of p* is collected. These points can be understood from the arguments of the last section, by considering the ϕ to be of zero width, and therefore analogous to the 'fixed mass' example of the last section.

On the other hand, the K^+K^-n phase space corresponds (very approximately) to the case of a uniform mass distribution, and its behaviour can therefore be understood by considering it analogous to a uniform mass distribution (see Fig.5.4, for

example, where $\frac{\partial\sigma}{\partial M_z}$ is constant). Thus, as p_π is raised, the K^+K^- mass plot tends to peak at higher values, but a good proportion of lower mass events is still collected. This accounts for the peaking in the observed production angular distribution at 1620 MeV/c, and the tendency to collect more high p* events here as well. The phase space yield increases as p_π is increased, due to the density of states factor increasing faster than the collection efficiency decreases.

The decay angular distributions (for both ϕ, and K^+K^-n phase space) are seen to have shapes which are rather independent of beam momentum. There is little experimental bias on the ϕ_ϕ angle, but the cos θ_ϕ distribution is strongly biased at cos $\theta_\phi \sim 1$. This is because the slower kaon in the laboratory is now at its slowest, since it is going directly backwards in the K^+K^- rest frame. It therefore has not enough energy to get through the Cerenkov-E-counter system, and the event is lost from the OKE class. This effect becomes particularly serious for the ϕ at 1620 MeV/c, for events in the $\theta^* \sim \pi$ peak in cos θ^*, Here the ϕ is now going relatively slowly in the laboratory, and events are only accepted if cos θ_ϕ is near zero. For events in the $\theta^* \sim 0$ peak in cos θ^*, however, the effect is reversed,

since the ϕ is now travelling fast in the laboratory, and can give both kaons enough energy to traverse the Cerenkov-E-counter system almost irrespective of the θ_ϕ angle. The total $\cos\theta_\phi$ distribution, however, being an integration over $\cos\theta^*$, does not change much with beam momentum over the range considered.

5.4 Resolutions

The resolution of the various parameters describing the production and decay processes could be obtained by comparing the original true values of these parameters, as generated by the Monte Carlo programme for the OKE events, with their corresponding fitted values, obtained after the events had undergone the process of being 'measured' by the apparatus and then fitted by the kinematics programme, as described in section 4.5.

These Monte Carlo resolutions, so estimated, are presented in Table 5.1 below, as the standard deviations of normal distributions (the normality assumption was a fair approximation in most cases).

Table 5.1

Parameter name	Standard deviation σ
Effective mass of dikaon system, $M_{K^+K^-}$	$\pm$ 4 MeV/c^2
$\cos\theta^*$	$\pm$ 0.15
p^*	$\pm$ 12 MeV/c
$\cos\theta_\phi$	$\pm$ 0.18
ϕ_ϕ	$\pm$ 0.15 radian

Each number listed in the table represents an average over the relevant distribution, and also over the total p_π range covered in the experiment. The resolution deteriorated slightly at higher p_π values.

In the experimental analysis, it was assumed that (within the limits of the approximations involved in the Monte Carlo and fitting programmes), the Monte Carlo and experimental resolutions were the same, so that the inclusion of the effects of the resolution into the Monte Carlo and experimental distributions would affect both sets of distributions in the same way. The numbers of Table 5.1 help to justify this assumption, since in general the resolution was good enough to cause little change in the distributions when its effects were included.

CHAPTER 6

Mainly Concerning the Extraction of Data from the Photographs

6.1 Scanning and Measuring of the Events

We proceed now to a description of the scanning and measuring of the events.

The image of the event on the film was projected onto a DMAC measuring table, through a lens system with a magnification ~ x 20 between film and measuring table. The lens system was designed by Dr. D.C. Potter. The overall magnification of either of the two views on the table, with respect to the corresponding projected view in real space, was approximately 0.5. A diagram of the two orthogonal views of an event, as they appeared on the table, is shown in Fig.6.1. View 1 was of the xy projection viewed in the positive z direction, view 2 of the xz projection seen along the negative y direction. The positions, in each view, of the E-counters, C-counter, A_o counter, hydrogen target, and beam axis, relative to the fiducial crosses in that view, were marked on a template. As an initial step in the scanning of an event, the position of the template on the table was adjusted until its fiducials coincided with the corresponding fiducials for the event. This enabled the scanning criteria to be applied to the event.

Fig. 6.1.

Arrangement of orthogonal views in the laboratory

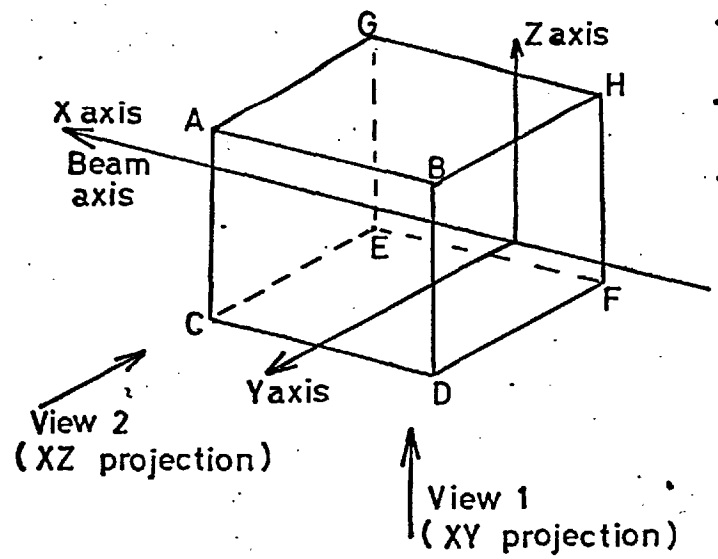

ABCDEFGH = spark chamber volume

ABCD and CDFE are fiducial planes

Arrangement of the two views on the measuring table

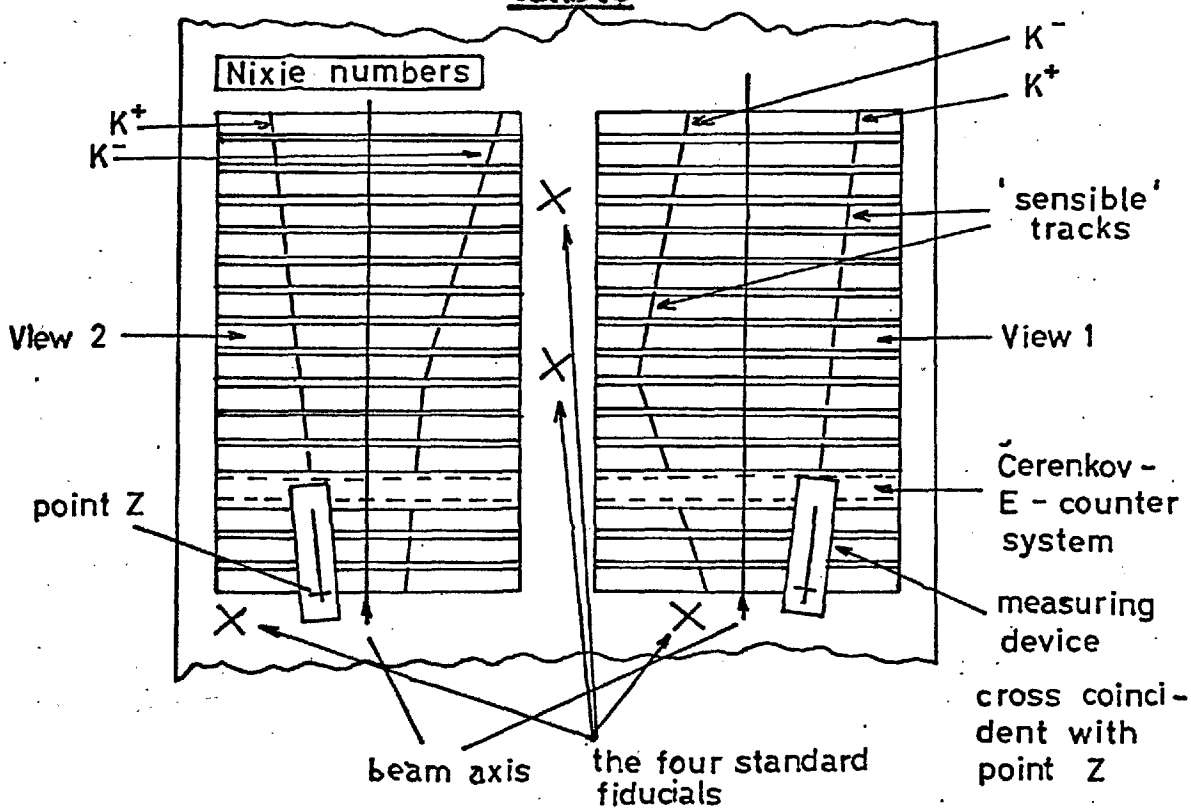

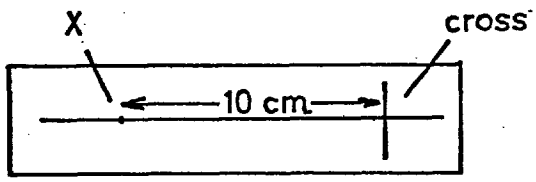

Measuring device

The scanning criteria which an event had to satisfy were as follows.

1. The event had to have a neutron time of flight value lying within the range allowed by the kinematics of the reaction $\pi^- p \rightarrow K^+ K^- n$, and the experimental biases. Accordingly, events lying outside a certain 'gate' in the neutron time of flight spectrum were rejected (this gate was narrower than the gate imposed by the electronic trigger).

2. The event was required to have at least two 'sensible' tracks appearing in the first 3 spark chambers downstream of the target. A 'sensible' track was defined as a track which came from the hydrogen target, and also passed through an E-counter, without going through the veto counter A_o behind the target (see Fig.6.1).

3. Each possible pair of sensible tracks (there was rarely more than one pair for an event) then had to satisfy the conditions:

a) In view 1 (xy projection), the two sensible tracks, and the direction of the neutron (known from the neutron counter which was triggered), had to have values for their projections onto the y axis, which were not all of the same sign (i.e. neither all positive, nor all negative). A similar condition held for the signs of their projections onto the z axis in view 2 (see Fig.6.2). Failure to satisfy the condition in either

Fig. 6.2.

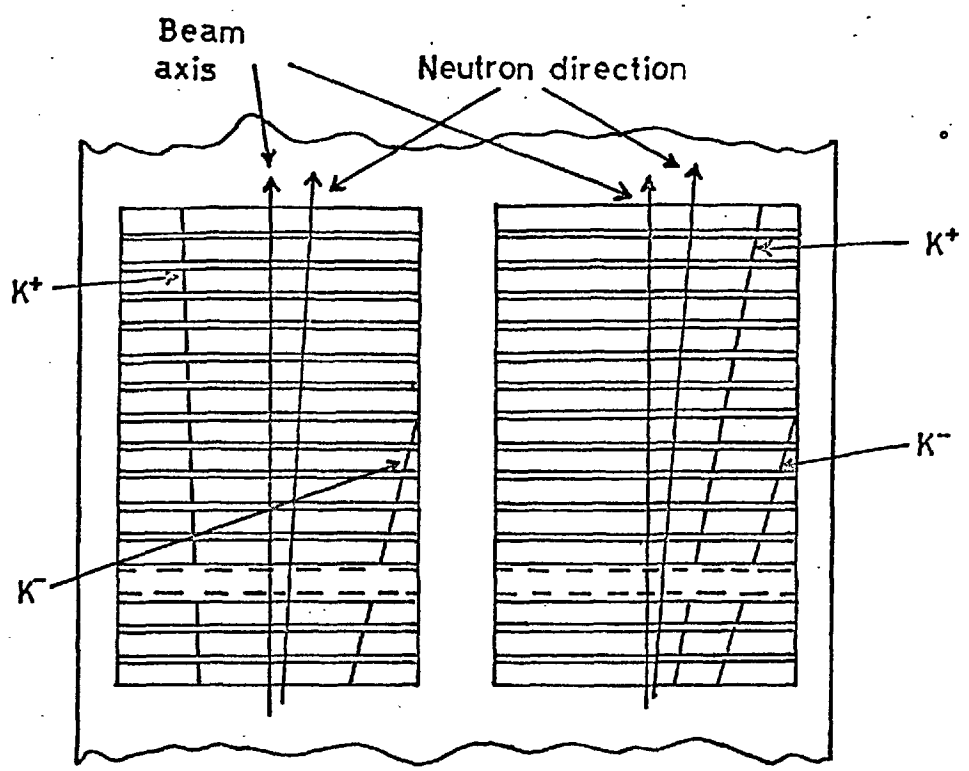

An example of an event rejected under scanning criterion 3a

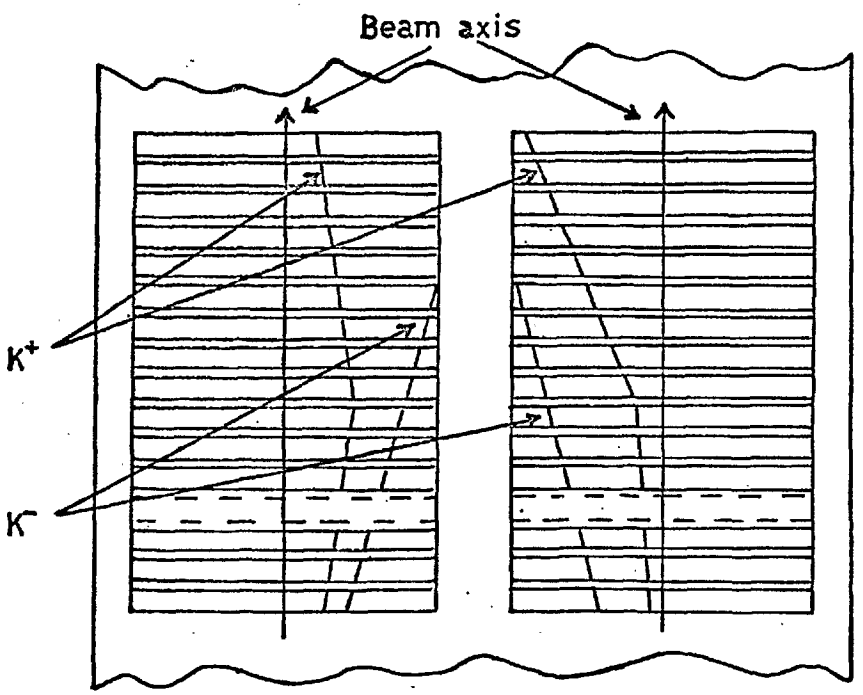

An example of an event rejected under scanning criterion 3b

view lead to rejection. This condition is valid because, if the direction of the input pion is taken as the x axis, it is impossible, with only 3 particles in the final state, to satisfy momentum conservation along the y- or z-axes with such a configuration; an event producing this configuration could only be KKn if the input pion direction was far outside the limits defined by the beam counters, which was very unlikely.

b) Both sensible tracks should not intersect the E-counter plane on the same side of the beam axis in both views. This would mean that they had both gone through the same E-counter, and therefore could not, alone, have triggered the E-counter system (see Fig.6.2).

An event which satisfied these criteria was then measured. The measuring device on the table was a flat rectangular block, 6" x 1" x $\frac{1}{8}$", upon which was marked an elongated cross (see Fig.6.1). In the surface of the table was a sensitive area. This area was mapped out as a two-dimensional Cartesian coordinate system fixed relative to the table surface. The spatial resolution of points along each axis of this system was 0.1 mm. The coordinates of a point in the sensitive area could be obtained in digital form on punched cards, by setting the cross on the measuring device

coincident with the required point, and sending the relevant instruction to the machine. The punched cards were produced by an IBM 1406 Card Punch adapted for use with the DMAC table. The measuring device could be used in two modes. In mode 1, only the coordinates of the cross on the table were produced; in mode 2, the coordinates of the cross, and also the coordinates of the point X on the elongation of the cross (see Fig.6.1) were obtained.

In the measurement of an event, four fiducial points were first measured, using the device in mode 1, and setting the cross coincident with the fiducials (see Fig.6.1). It was necessary to measure these fiducials in order to be able to relate measurements subsequently made on the kaon tracks, to a set of points in the measuring table space whose coordinates were known in laboratory space. The measurements made on each track in each view to provide the information required by the geometry programme were as follows (see Fig.6.1.): the elongated cross was aligned (by eye) along the track projection in view 1, with the cross itself coincident with the projection of some point on the track whose projection in the other view was easily identifiable (point Z in Fig.6.1). The measuring device was now used in mode 2, so that the coordinates of two points on the track in this projection

were obtained. In view 2, a similar procedure was adopted, with the actual cross at the same x position as before (point Z). From this information, the real space direction cosines of the track, and the real space coordinates of point Z on the track, could be calculated.

The digitized neutron time of flight, the number of the neutron counter which had triggered, and the hodoscope momentum channel of the input pion, were also punched onto the cards.

The fate of each 'sensible' track as it passed through the spark chamber system was also recorded, by means of a series of code numbers. These code numbers were used to record any changes in the track, and also to designate where in the chamber volume they occurred. The reason for noting these changes was so that events of the experimental OKE class could be selected by the computer after the event had been successfully fitted by the kinematics programme. Two types of change were usually encountered:

1. A change in the direction of a track by $> 10^{\circ}$. This may have been due, for example, to a decay in flight, or to an elastic scatter in material.

2. Termination of a track, where this was not due to the particle having left the sensitive volume of the chambers.

A kaon may have stopped in the Cerenkov-E-counter system, and no charged reaction product continued into the chambers, for example.

Changes occurred, in general, in the Cerenkov-E-counter system, since the bulk of the material in the chamber volume was here.

6.2 Reconstruction and Kinematic Fitting of the Events

After measurement, the event was processed by the geometry programme. The geometry programme used was written by Dr. W.G. Jones: its basic functions are described below.

The fiducial points for each view were set in a plane perpendicular to the direction of that view (i.e. in planes ABCD, CDEF of Fig.6.1). Measurements made (in measuring table space) on the kaon tracks in each view were actually made on the projections of the tracks in the fiducial plane of the view, since they were made with respect to the fiducial points in the fiducial plane. The programme first calculated the laboratory coordinates of the projected points in the fiducial plane, from their coordinates in the measuring table space, using previously calculated equations relating measuring table and laboratory space coordinates.

The programme then calculated the direction cosines of

each track in the laboratory. For each view a plane was defined, using (from the event measurement) the (laboratory) coordinates of two points on the projection of the track in the fiducial plane of that view (see Fig.6.1), and the effective position of the camera in that view (i.e. the position at which the camera appeared to be, when viewed from the chamber volume through the mirror system for that view). The line of intersection of these two planes (one plane for each view) was then taken to have the direction cosines of the track.

For each track, the laboratory coordinates of the point Z on the track (see Fig.6.1) were also calculated. In each view, a line was constructed which passed through the projection of the point Z in the fiducial plane of that view, and through the effective camera position for that view. Theoretically, the two lines so formed should intersect at the point Z, but in practice they rarely did so because of measurement errors. The best estimate of the position of the point Z was therefore taken as the midpoint of the common perpendicular of the two lines.

Knowing the direction cosines of each track, and the coordinates of a point (Z) on each track, the position of the vertex could now be found as the point of intersection

of the two (extrapolated) tracks. In practice the two tracks rarely intersected, again due to measurement errors and scattering, and the best estimate of the vertex position was taken as the midpoint of the common perpendicular of the two tracks. New direction cosines were then calculated for each track, taking the track to pass through the vertex and the point Z on the track (see sketch below). The amount by which the original estimates of the direction cosines were changed in this procedure was related to the errors on the kaon θ and ϕ angles used in the kinematic fitting process. Using this relationship, and distributions of these corrections to the original direction cosines obtained from a sample of K^+K^-n events, the standard deviation of the kaon θ and ϕ angles was calculated as 0.015 ± 0.003 radian.

There were two criteria in the geometry programme which an event had to satisfy.

a) The corrections to the original estimates of the direction cosines, outlined above, should not be greater than a certain amount. In the sketch below, Z1 and Z2 are the 'Z' points on each track, Z1.A and Z2.B are the extrapolated tracks, AB is their common perpendicular, and V is the vertex position.

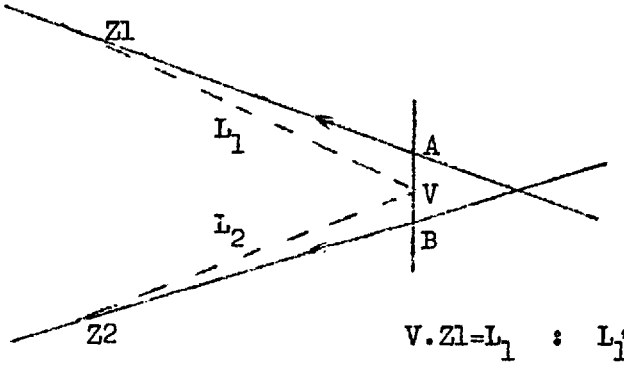

$V.Z1 = L_1$: $L_1 \approx L_2$

$V.Z2 = L_2$: $AV = BV = d$

Then both the angles $\Delta\theta_1 \approx d/L_1$ and $\Delta\theta_2 \approx d/L_2$ ($\Delta\theta_1 \approx \Delta\theta_2$) had to be < 0.045 radians for the event to be accepted.

b) The vertex of the event had to lie within a region defined to be the hydrogen target region. This was taken to be a cylinder with its axis coincident with the beam axis, similar to the physical target, but somewhat longer (50 cm cf. 32.3 cm), and of larger diameter (8 cm cf. 6.5 cm).

Apart from the fraction of KKn events lost due to statistical processes, which could be estimated, KKn events which had been badly or incorrectly measured could also be rejected by these criteria; so a sample of events which failed the geometry criteria were remeasured to ascertain this loss as well. This type of loss could be kept very small due to the application of cross-checks performed on an event in the geometry programme. The loss of KKn events due to these criteria was estimated at about 1%.

An event satisfying the criteria in the geometry programme was then tested against the hypothesis $\pi^- p \rightarrow K^+K^- n$ in the kinematic fitting programme. An event was required to satisfy the following conditions before it was accepted as $\pi^- p \rightarrow K^+K^- n$:

a) An event had first to satisfy the 'coplanarity' requirement. This condition was applied before the fitting process was attempted. The direction cosines of the momentum vector of the dikaon system in the laboratory were first calculated using only momentum conservation applied to the reaction $\pi^- + p \longrightarrow$ neutron + missing mass, employing the measured (but unfitted) momentum vectors of the pion and neutron in the equations. The requirement was that the momentum vector of the $K\bar{K}$ system then had to lie in the plane defined by the two kaon directions in the laboratory, within certain limits governed by the estimated errors on the parameters involved. This was equivalent to demanding that the final state particles should be coplanar in the overall centre of mass system (c.m.s.), and was designed to reduce background of the type involving 4 or more particles in the final state, which in general would not be coplanar in the c.m.s..

b) The fitted events had to satisfy the constraint equations to within certain limits. The four constraint equations,

embodying energy and momentum conservation in the reaction, were not exactly satisfied in practice, since the fitted parameters (m_i) were very close to their final values after only a few iterations; to save computer time, the iterative process continued only until the 3 momentum equations were satisfied to 0.5 MeV/c, and the energy equation to 0.5 MeV. In some cases, however, the fit could not converge to satisfy the equations to these limits, after the maximum number of iterations allowed (ten) had been attempted. This might have occurred if the event had really been $\pi^- + p \rightarrow \pi^+ \pi^- \pi^0 n$ where the π^0 had been missed, and the $\pi^+ \pi^-$ simulated the K^+K^- pair.

c) The value of χ^2 for the event had to be < 10. The mean value of χ^2 for Monte Carlo $\pi p \rightarrow K^+K^-n$ events was about 2, with ~ 1% having $\chi^2 > 10$. Non-KKn events, however, would generally tend to have large χ^2 values, so that these events were again discriminated against by this criterion.

d) The fitted values of both the kaon momenta were required to be > 230 MeV/c. This was because events of the CKE class, which were the ones used in the final analysis, were required to suffer no changes in the Cerenkov-E-counter system, and a kaon with a momentum of < 230 MeV/c was bound to stop in this counter system. This criterion was again

good for eliminating events involving pions rather than kaons.

The Monte Carlo OKE events were also required to satisfy these four criteria in the fitting process. The percentage of Monte Carlo KKn events rejected due to these criteria was between 2% and 3%.

The total fraction of KKn events lost due to all criteria in the geometry and kinematics programmes was taken as $4 \pm 2\%$.

A loss of KKn events would also have occurred during the scanning process. It was therefore necessary to determine the 'scanning efficiency' for K^+K^-n events. We made an estimate of this number by scanning a large sample of the film again, this time using two scanners, whereas only one had been used in the first scan. The efficiency was then defined as

$$E = \frac{N_1}{N_1 + N_{12}} \qquad \ldots 6.1$$

where N_1 was the number of OKE events found in the first scan which eventually fitted $\pi^- p \rightarrow K^+K^-n$, and N_{12} was the number of OKE events found in the second scan, but not in the first, which fitted $\pi p \rightarrow K^+K^-n$. The scanning efficiency, thus defined, was found to be $(93 \pm 6)\%$, and was approximately independent of

the variations in the signal-to-noise ratio encountered over the range of beam momenta covered during the data-taking.

6.3 Ambiguous events

Unfortunately, effects existed which made unambiguous classification of certain events impossible, and weighting procedures had to be adopted for such events. Two types of ambiguity were encountered.

1) The Nixie light displaying which neutron counter (WNC) had been triggered during the event being photographed, sometimes displayed two neutron counter numbers. This was due partly to electronic pickup from the spark chambers in the circuits operating the display lights, and partly to uncorrelated random triggers in other neutron counters coinciding with the true neutron counter triggers. About 30% of the pictures were affected in this way.

Two kinematic fits were attempted on these events, using a different one of the two possible WNC values in successive fits. In general, it was found that the final classifications of the two fits would be the same i.e. both would have $\chi^2 > 10$, both would give good fits, etc., so that the event would be either accepted or rejected as in the normal case. However, a small fraction of such ambiguous WNC events produced

different end-classifications; in events where one WNC value produced a good fit, whilst the other WNC was rejected under one of the criteria, a weighting procedure was necessary. Such an event was weighted with the relative probability of getting a good fit rather than getting the event rejected under the particular rejection criterion concerned using the other WNC of the pair. This probability was found by noting the relative frequency of the two types of classification concerned in the unambiguous events satisfying the geometry criteria.

The proportion of events which had to be weighted due to this type of ambiguity was about 8%. In practice the weighting factor was always close to unity.

Similar ambiguity occurred in the Nixie light indicating which hodoscope channel had fired, but to far less extent.

2) The second type of ambiguity arose when more than two 'sensible' tracks appeared on a picture, and more than one combination of any two of these tracks passed the scanning criteria. In this case, all the accepted possible combinations were tried in a fit. In general the end-classifications of all the fits for the event would not be the same, and when some pairs gave good fits, while others did not, the event was weighted by the factor $\frac{1}{2}$. This was effectively saying that it was

equally probable that the event was either an unambiguous 'good fit' which had become contaminated by uncorrelated random tracks (casuals), or it was a process with more than 3 particles in the final state. This was the simplest form of weighting possible, and no attempt was made to resolve this class into the two sub-classes stated above, since any error introduced into the yield of KKn events per pion at any p_π value as a result of this weighting was always a good deal less than the statistical error. The fraction of events at a p_π setting that needed to be weighted in such a way, did in fact vary with beam conditions, indicating that casual effects were present. This fraction was typically about 10%.

No event which had been classed as ambiguous was used afterwards in the experimental distributions, only in the total yield of KKn per pion at that p_π. No bias should arise in the distributions as a result of this.

6.4 Elimination of systematic errors

After the preliminary fitting of the events had been completed, the data was examined for systematic errors in any of the ten quantities used as known variables in the fit process. The chief systematic errors occurred in the neutron time of flight, and in the absolute value of the p_π setting for a block of 4 hodoscope channels.

1) <u>Neutron time of flight error</u> (see section 3.3)

The time of flight of a neutron was calculated from the time separation between the neutron and the γ peak position, knowing the distance the neutron had travelled, and the velocity of light. This assumed that the time position of neutrons travelling with the velocity of light was the same as that of the γ peak; as γ rays tended to produce bigger photomultiplier pulses than fast neutrons, and thereby triggered the neutron counter discriminator earlier, this assumption could possibly have introduced a systematic error into the neutron time of flight.

To estimate this error, a time of flight spectrum was plotted of the unambiguous events from the 1580 MeV/c data which fitted K^+K^-n. The unfitted time of flight values were used. The yield of ϕ was largest at 1580 MeV/c and it turned out that there was very little KKn background under the ϕ here. Also the time of flight spectrum obtained inside the timing gate imposed in the scanning was contaminated with only a little non-KKn background. A Monte Carlo time of flight spectrum, using unfitted times with the correct random timing error introduced, was also produced. This consisted mainly of ϕ, plus a little phase space, in approximately the right proportions, at the

same momentum. The experimental spectrum was tested against the Monte Carlo spectrum in a least squares fitting process, adjusting the position of the experimental bump on the time axis of the Monte Carlo bump until the χ^2 value minimised. The separation of the γ peak from the position on the Monte Carlo time axis of neutrons travelling at the speed of light then gave the systematic error, which was 1.1 ± 0.3 nsec. This method suffered from the disadvantage that the model assumed in the Monte Carlo programme had to be a good approximation to the truth, so that the two bumps would have the same shape.

2) <u>P_π Error</u>

Data was taken at 3 p_π settings above the KKn threshold, with 4 points being obtained on the curve of yield of KKn per pion against momentum p_π for each setting, since 4 hodoscope channels were used. The error was split into two types a) the absolute value of the, say, central p_π setting could have a systematic error; b) in changing from the central p_π setting to one of the outer settings, hysteresis effects could produce errors in the separation of the two p_π settings, since our only indication of the magnet's field at the time was via its current.

This problem was only partially solved. The systematic

error in the central p_π setting at the nominal value of 1580 MeV/c was estimated, using the known value for the ϕ mass. A KKn mass plot of the unambiguous events at 1580 MeV/c which fitted KKn was compiled, using the fitted masses. An analogous Monte Carlo mass plot was also produced, using as the mass of the resonance the known mass of the ϕ (1018.6 MeV/c^2). In a manner similar to that used to find the time of flight error, the two curves were fitted against each other, adjusting the position of the experimental mass plot on the mass axis of the Monte Carlo plot until χ^2 minimised. The resulting translation of the experimental plot along the mass axis that was necessary could be simply related to a corresponding change in the experimental p_π value, which was then supposed to be the systematic p_π error. The required change in our case was in fact zero. The only uncertainty in the value of the central momentum (± 1 MeV/c) was now due to the uncertainty in the ϕ mass ($\pm$ 0.5 MeV/c^2). The two outer p_π settings had this error combined with their estimated 'separation' errors, making a nett error of ± 2.5 MeV/c. The situation is shown in Fig.7.1.

6.5 Analysis of the fits obtained

After elimination of these systematic errors, the

distributions of the variables parametrizing the kinematic fitting process for the experimental unambiguous KKn events, were compared to the corresponding Monte Carlo distributions. Good agreement between the two sets of results was necessary, to give general confidence in the experimental analysis. The χ^2 distribution for experimental events compared well with the Monte Carlo distribution (Fig.6.3), both having a mean χ^2 of ~ 1.8. The experimental stretch functions (see section 4.4) also compared well with their Monte Carlo counterparts, and were quite symmetrical about zero deviation. These stretch functions were not used in the elimination of the systematic errors, as (for the 2-constraint fit) they appeared less sensitive to these errors than the methods described in the previous section. Finally, the relation (see appendix 2)

$$(G^{-1}_{\text{unfitted}})_{ii} = (G^{-1}_{\text{fitted}})_{ii} + (G^{-1}_{\text{correction}})_{ii} \quad \ldots 6.2$$

was found to be well satisfied by the experimental events.

6.6 The non-K^+K^-n background and its subtraction

To investigate the non-KKn background, pictures of the electronic trigger were taken just below the KKn threshold, at $p_\pi = 1480$ MeV/c (threshold = 1486 MeV/c). We wanted to know how this background would affect the total yield of KKn

Fig. 6.3. χ^2 distributions

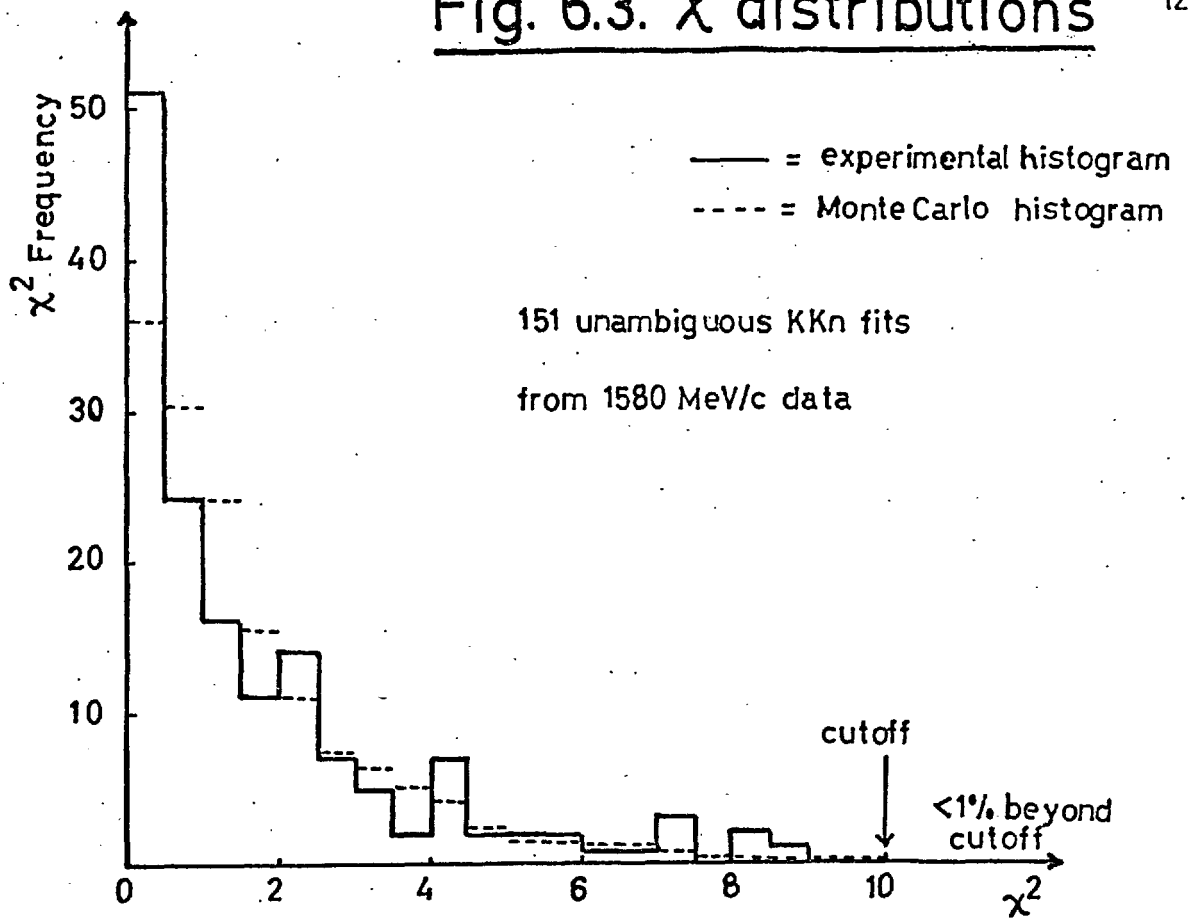

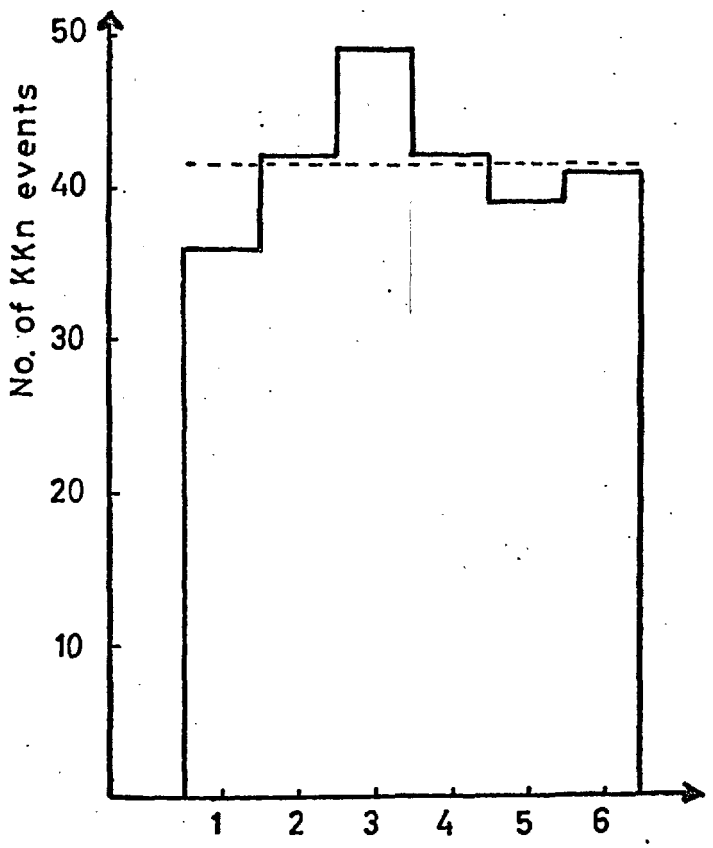

Fig. 6.4.

Histogram of number of KKn triggers versus neutron counter number (all unambiguous KKn data)

- - - - = Monte Carlo
—— = experimental
(error is statistical only)

events per pion and also the experimental distributions, at the 3 values of p_π used for the signal. It turned out that the background was very small compared to the signal at all the 3 p_π values, so that certain assumptions invoked in order to subtract the background, did not need to be rigorously satisfied in practice.

The pictures of the background events were first scanned, and then reconstructed in the geometry programme in the normal way. We then considered only the unambiguous background events that safely passed the criteria fixed by the geometry programme. These were called 'good geometry' events. We defined X as the yield per pion of unambiguous 'good geometry' background events, and Y as the ratio -

$$Y = \frac{\text{unambiguous 'good geometry' background events which fit KKn}}{\text{unambiguous 'good geometry' background events which do not fit KKn}}$$

- at the same p_π. The subtraction method first demanded that the values of Y should be known at the 3 p_π settings above threshold. However, the only 'clean' sample of background events available was produced below the KKn threshold. These 'good geometry' events from below threshold were therefore fitted in the kinematics programme, using as their initial

unfitted p_π value, the value of p_π at which Y was required above threshold, rather than their true p_π value of 1480 MeV/c. The first assumption, then, was that the value of Y obtained for this p_π, using the 1480 MeV/c data in this way, was the same as would be obtained from the true non-KKn background at this p_π, if the KKn events could be removed. $\pi^- p \rightarrow \pi^+ \pi^- \pi^0 n$ was probably a dominant contributor to the background, and for this process at least, this assumption could be justified by Monte Carlo methods. $\pi p \rightarrow \pi^+ \pi^- \pi^0 n$ phase space events were generated, where the two charged pions went into the E-counters, and the fate of the π^0 was ignored. A first class of these events was generated, and fitted to KKn, at 1580 MeV/c; another class of events was generated at 1480 MeV/c, but fitted with a p_π value of 1580 MeV/c. The values of Y obtained in both cases were approximately the same.

In practice, the ratio Y was observed to increase with p_π. Whether or not a background event would fit KKn, seemed to depend upon the range of K^+K^- masses that it was possible to produce with the event's artificial p_π value (allowed to change only a little in the fit). Since the range increased with the artificial p_π value, this observation seemed sensible.

There was also some evidence that the quantity X increased with p_π over the range considered. This could reasonably be expected; for the $\pi^- p \rightarrow \pi^+ \pi^- \pi^o n$ events at least, the $\pi^+ \pi^- \pi^o$ mass spectrum has been found to exhibit either an enhancement(34) or a resonance (Al-mass 1070 MeV/c^2, width 50 MeV/c^2) in this p_π region.

The values of Y had been calculated at a fixed X value, from the 1480 MeV/c data; this necessitated another assumption. It may have happened, that a number of processes contributed to X, but only one of these processes had a contribution to X which varied with p_π ; then unless all the processes (at any given p_π) had the same value for Y, the nett value for Y for the summed processes would vary with p_π simply because the proportions of the member processes of X would change as p_π was increased. Since this type of variation would not have been measured in our measurement of Y as a function of p_π , we had to assume Y was the same for all processes contributing to X, for any p_π in our range. However, X was probably dominated by $\pi p \rightarrow \pi^+ \pi^- \pi^o n$ anyway, so this second assumption needed to be only approximately valid. Under these assumptions the background yield per pion at a p_π above threshold was subtracted from the total yield per pion

to give the signal yield per pion, by the following method.

Suppose that at this p_π there were in the 'good geometry' classification

a unambiguous KKn fits.

b ambiguous KKn fits (total number).

z events giving an ambiguous KKn fit, in which the various possible pairs of sensible tracks were all due to the same reaction in the target (i.e. 4- or more-body final states - called events of type Z).

a' unambiguous rejects.

b' ambiguous rejects (total number).

z' ambiguous type Z events in which all possibilities were rejected.

and there were q pions. (In order to simplify matters, the ambiguous events of type (1) i.e. double WNC events, were included in the unambiguous class, since they were a small class whose weight was close to one anyway. The ambiguous events referred to are thus all of type 2). The number a' would contain some KKn which had been rejected due to the criteria in the kinematics programme. This was approximately Wa, where W was the fraction of Monte Carlo KKn events which were

rejected at this p_π i.e. ~ 4%. The remainder of the unambiguous rejects (a'-Wa), were then supposed to be pure background. The yield per pion of background events (B) which fitted KKn at this p_π, was then found using the ratio Y for this p_π

$$\text{i.e.} \quad B = (a'/q - W\, a/q)\, Y \qquad \ldots 5.3$$

The unambiguous signal yield per pion was then

$$= \frac{a}{q} - \left| \frac{a'}{q} - W\frac{a}{q} \right| Y \qquad \ldots 6.4$$

A similar argument applied for the KKn events contaminated by random tracks that were ambiguous i.e. the type 2 ambiguous events remaining after the z events which were not KKn had been subtracted.

$$\text{Ambiguous signal yield per pion} = \frac{b - z}{q} - \left| \frac{b' - z'}{q} - \frac{W(b - z)}{q} \right| Y \quad \ldots 6.5$$

The nett signal yield per pion was then

$$S = \frac{a}{q} + \frac{b - z}{q} - \left| \frac{a'}{q} - W\frac{a}{q} \right| Y - \left| \frac{b' - z'}{q} - \frac{W(b - z)}{q} \right| Y \qquad \ldots 6.6$$

Now $\frac{b' - z'}{b - z} = \frac{a'}{a}$ since the ambiguous events of this type were due to uncorrelated random tracks.

Also, we have assumed that the ambiguous events of type (2) would be either contaminated unambiguous ones, or ones with more than 3 final state particles, with equal probability,

$$\therefore \quad z = \tfrac{1}{2}b$$

$$\therefore \quad s = \frac{a}{q}\left|1 + \frac{b}{2a}\right| - \left|\frac{a'}{q} - \frac{Wa}{q}\right| Y. \left|1 + \frac{b}{2a}\right| \qquad \ldots 6.7$$

= Total yield per pion − background yield per pion

The actual numbers which were obtained are listed below (Table 6.1). The background has been averaged over the four hodoscope channels at one p_π setting.

Table 6.1

Central $p\pi$ Setting (MeV/c)	a	b	a'	q $\times 10^8$ pions	Y	Background per 10^8 pions	Background / Average signal
1540	31	10	60	18.5	0 ± 0.06	0 ± 0.2	0–10%
1580	160	4	35	7.0	0.12 ± 0.06	0.5 ± 0.2	~ 2%
1620	135	24	55	15.0	0.12 ± 0.06	0.5 ± 0.2	~ 5%

As can be seen from the last column in the table, the background was usually very small compared to the K^+K^-n signal.

It was decided to subtract background only from the total yield per pion, and not from the experimental distributions, at each signal p_π. This was because a) background was so small, b) so few background events could be obtained at 1480 MeV/c, that the distributions obtained for background events were very inaccurate. The background distributions, such as they were, appeared fairly smooth, however.

6.7 Constant factors in the cross-section calculations (see section 4.2)

Before proceeding to a discussion of the later stages of the analysis, it is convenient to end this chapter with a consideration of some correction factors used in the derivation of the ϕ production cross-section.

As stated in section 4.2, the Monte Carlo OKE events had further tests to satisfy before they could be regarded as equivalent to the experimental OKE events. These tests were not included in the Monte Carlo programme because the effects they simulated were taken as independent of the kinematic parameters of the event (e.g. neutron counter efficiency)(in some cases this was an approximation, valid only because the effect was small). Correction factors also had to be applied to the number of effective beam particles (e.g. the percentage of pions in the beam). As all these factors were multiplicative they were all combined into a single factor ($F = \prod_i f_i$) which was arbitrarily regarded as weighting the number of Monte Carlo OKE events. The factors f_i are listed below.

<u>$\phi \rightarrow K^+K^-$ branching ratio:</u> $f_1 = 0.48$ ($\pm$ 7 %)

This number was taken from the current data tables.[21]

<u>Neutron counter efficiency:</u> $f_2 = 0.278$ ($\pm$ 11%)

The range of neutron kinetic energies covered in the experiment was approximately 150 to 450 MeV. We were unable to measure the efficiency of our neutron counters over this energy range, and were not aware of any other measurements having been made in this range. The calculations of neutron counter efficiencies by Kurtz,[35] however, were in good agreement with the measurements of Auld,[36] Gatti,[37] and Wiegand,[38] made at kinetic energies between 20–130 MeV. In particular, the measurements of Auld were made with counters of the same scintillator as ours, and were very similar in shape to ours, being only slightly thinner. It was therefore decided to use the Kurtz calculations at higher energies as the basis of our estimate of the neutron counter efficiency.

In practice, pulses from a neutron counter photomultiplier are generally fed into a discriminator, which will trigger only on pulse heights which are greater than its threshold level. This arrangement is to reduce noise pulses from the photomultiplier. Neutrons producing small pulses are therefore not detected because of this finite 'bias' level of the apparatus, and the neutron detection efficiency is a function of this bias. Rather than define the bias level as a certain

voltage setting on the discriminator, which would depend upon the photomultiplier gain, etc., it is defined in terms of the energy deposited in the scintillator by a proton, brought to rest in the scintillator, which produces a pulse height just enough to trigger the discriminator (in practice, there would be a small spread in pulse heights, but we consider the most probable pulse height of the distribution here, and in what follows).

In our experiment, the bias level for each neutron counter was first found by comparing the pulse height which would just trigger the discriminator, with the pulse height produced when a relativistic beam pion went straight through the 30 cm. of the neutron counter scintillator. Since the pion must have lost approximately 60 MeV in doing so, the bias level could be directly calibrated in terms of the amount of energy a fast pion had to give to the scintillator to just trigger the discriminator. The average bias level was thus found to be 4.8 ± 0.6 MeV for fast pions. However, we wanted the bias level to be in terms of the energy given to the scintillator by stopping protons, and these produce less light than fast pions (or fast electrons) for the same amount of energy lost, due to saturation effects in the scintillator,

which occur when the ionization density is high. The conversion factor to go from the 'electron' scale to the 'proton' scale was taken from the paper of Bellamy.[39] The average bias level for our counters was then 10 ± 1.2 MeV proton energy.

The Kurtz calculations showed that the efficiency was almost independent of neutron kinetic energy between 150 and 260 MeV, and also that the efficiency was not affected much by small changes of bias level around the nominal 10 MeV proton energy. It was therefore assumed that:

a) the efficiency was the same for all counters - they were all identical in construction, and differences in bias levels were small (and anyway would not affect the efficiency much).

b) the efficiency was independent of neutron energy in the range 150 to 450 MeV.

The value taken for the efficiency was then based on the value calculated by Kurtz for the Auld counters, at 200 MeV neutron energy, and at a bias level of 10 MeV proton energy; this value had only to be corrected for the slight difference in counter thicknesses, to go to our counters from the Auld counters.

The assumption (a) was partially justified, using the

unambiguous fitted KKn events, by noting the relative trigger frequency of each neutron counter for $\pi p \rightarrow K^+K^-n$ events. This is shown in Fig.6.4: it is seen that, within the 15% statistical accuracy, the distribution was consistent with being flat (there was virtually no bias on the neutron azimuth angle).

The error in f_2 arises mainly from the 10% error quoted in the Kurtz calculations.

<u>Electronic loss factor</u>: $f_3 = 0.68\ (\pm\ 10\%)$

A significant loss of KKn events occurred due to unavoidable limitations in the electronic logic system. The main loss was due to the fact that any anticounter in the system was capable of vetoeing a KKn event, if it produced an uncorrelated, random pulse, in close time proximity (about 30 nsec. or less) to the KKn event. The chief culprit in this 'occupancy' loss was A_o, the counter immediately behind the E-counters, through which passed much of the beam, and which therefore had a high counting rate. The occupancy of A_o was monitored during the data-taking by measuring the ratio of the counting rates

$$R = \frac{S_2 \cdot \Sigma P_{\pi\ i} \cdot \bar{A}_7 \cdot (A_8 + A_9 + A_{10} + A_{11}) \cdot \bar{A}_o}{S_2 \cdot \Sigma P_{\pi\ i} \cdot \bar{A}_7}$$

i.e. the number of beam particles $(S_2 \Sigma P\pi_i \bar{A}_7)$ which produced an associated pulse in one or more of the four large anti-counters surrounding the target, without producing an associated A_o pulse, per beam particle. This ratio was measured under the data-taking beam conditions, and also under conditions of very low beam, when the counting rate in A_o was low, and the occupancy became negligible. The ratio measured at the data-taking beam conditions had to be corrected for the effect of uncorrelated random coincidences between $S_2 \Sigma P_{\pi i} \cdot \bar{A}_7 \cdot \bar{A}_o$ and $(A_8 + A_9 + A_{10} + A_{11})$.

Comparison of the corrected ratio R at data-taking beam conditions, and the ratio at low rate conditions, indicated that this effect produced a $(21 \pm 8\%)$ loss of KKn events.

The same effect occurred to less extent in the Cerenkov counter, the anticounters surrounding the hydrogen target, and the anticounters in front of the neutron counters. Their summed contribution to the KKn loss was estimated at $(13.5 \pm 4)\%$.

Other small effects contributing to f_3 were due to discriminator 'dead-times' in the logic systems of the E-counters and neutron counters, and also to dead-times in the scalers counting the numbers of 'good' beam particles $(S_2 \cdot P_{\pi i} \cdot \bar{A}_7)$ in a hodoscope channel, which affected the normalization.

There was also a 1% loss due to dead time of the discriminator in the system which measured the neutron time of flight. Although a picture would still be taken if this discriminator was dead, the time of flight on the picture would be zero, so that the picture would be rejected under the first scanning criterion.

Beam composition: $f_4 = 0.78$ ($\pm$ 6%)

This was the fraction of the total beam that consisted of pions (see Chapter 2 for its measurement).

Interactions of neutrons: $f_5 = 0.925$ ($\pm$ 2%)

In general, neutrons had to pass through about 16 cm. of hydrogen, 2 cm. of scintillator in the E-counters (or, if they went into the E-counter centre, 2 cm of A_0), and 4 m. of air, in their passage to the neutron counters. Some neutrons also had to traverse the 5 cm. of water in the Cerenkov counter, though many passed through the hole in the centre. An appreciable loss of signal therefore occurred due to neutron interactions in this matter. KKn events could also be lost if the neutron interacted in the first 7 mm or so of the neutron anticounter (1 cm thick), since this would produce a veto pulse.

Data on total interaction cross-sections for neutrons in carbon, copper, and lead, in our energy range, showed that

the total cross-section was roughly energy-independent over this range.[40] The cross-section was therefore taken as constant, and equal to 50 $A^{1/3}$ mbarn, where A is the atomic number of the relevant material. The value for f_5 given above does not include the contribution of the Cerenkov counter to this loss; this was included in the Monte Carlo programme, since not all neutrons accepted by the neutron counters passed through the Cerenkov counter.

Neutron anticounter effects:

a) $f_6 = 0.97$ ($\pm$ 2%) It was possible that the neutron from a KKn event, when it interacted in the neutron counter, would produce charged particles that went backwards into the anti-counters in front of the neutron counters, thereby vetoeing the KKn event. The number used here is taken from ref.(11), where it was estimated by comparing experimental and Monte Carlo data.

b) $f_7 = 1.01$ ($\pm$ 1%) There was also an effect due to neutrons interacting in the last few mm of the neutron anticounters, where the interaction products went on to produce a signal in the neutron counter, but did not produce enough light in the anticounter for it to veto the event. This was equivalent to an increase of a few mm. in the length of a neutron counter.

<u>δ -ray loss</u>: $f_8 = 0.975$ ($\pm$ 1.5%)

The Cerenkov counter, used in its normal mode, was set so that it vetoed almost the whole range of pulse heights produced at its anode by electrons originating from the photocathode. This arrangement enabled the photography rate to be kept low, without appreciably affecting the KKn signal. However, kaons could veto themselves in the Cerenkov counter by producing δ-rays, which subsequently produced Cerenkov light. Calculations indicated that the mean number of photoelectrons produced at the photocathode per KKn event would be considerably less than one; assuming this number was distributed according to Poisson statistics, the KKn events which did produce photoelectrons at the cathode would therefore in general produce only one photoelectron. This meant that the pulse heights at the Cerenkov counter anode from KKn events lost by δ -ray production, would generally fall within a small voltage range, whose width was governed mainly by the statistics on the mean number of electrons produced at the first dynode of the tube, when only one electron came from the photocathode.

Therefore, by demanding that the electronic logic trigger should have a Cerenkov pulse associated with it whose height lay

in this voltage range, this originally lost class of KKn could be photographed. The lower edge of the voltage range was set to coincide with the upper edge of the pulse height range allowed when the Cerenkov counter was used in its normal mode, whilst the upper edge was set so that, in fact, the range included most of the pulse height spectrum for the case of two photoelectrons from the photocathode as well.

The pictures were taken at 1580 MeV/c, where the KKn yield was at a maximum. They were then scanned for OME events (the kaon does not change direction appreciably when it produces a δ-ray), using the normal scanning criteria. The yield of fitted KKn per pion from these pictures was then compared with the corresponding figure for the normal data at 1580 MeV/c, to find the KKn loss due to this effect. (Non-KKn background was not subtracted from the 'δ-ray' pictures, so that the KKn loss as estimated (5%) was an upper limit; the best estimate of the true loss was then taken as half this upper limit).

<u>Non-hydrogen events:</u> $f_9 = 1.01\ (\pm\ \frac{1}{2}\%)$

Due to the criteria imposed in the geometry programme, only the melinex end-caps of the hydrogen target 'sausage', and the melinex windows of the outer container, could contribute

to this effect. The number of protons in this matter was only 2% of the number in the hydrogen, and not all of these would be effective in producing KKn events.

<u>Loss due to 10° OKE cutoff:</u> $f_{10} = 0.98$ ($\pm$ 1%)

KKn events could be lost during the scanning process, due to kaons having undergone Coulomb scatters of greater than 10°, and thereby being rejected from the OKE class by the scanning criteria. This loss was strictly momentum-dependent, being a 20% effect for kaons which only just managed to pass through the Cerenkov and E-counters, but tending rapidly to zero as the kaon momentum increased. However, since so few events had a kaon which almost stopped in the E-counters, the effect of this loss on the experimental distributions was very small compared with statistical errors, and it was therefore considered as a constant factor, affecting only the total yield.

<u>Degradation of beam along the target length:</u> $f_{11} = 0.98$

The beam intensity was attenuated by 4% in passing through the total target length, due to pions interacting in the hydrogen. The mean attenuation was therefore 2%.

The product of all these terms, $F = 6.05 \times 10^{-2}$ ($\pm$ 18%) .

CHAPTER 7

The Results, and a Comparative Discussion

7.1 Introduction

As stated previously, data were taken at four different momentum settings of the beam: a) at 1480 MeV/c, below the K^+K^- threshold; b) at 1540 MeV/c, just below the ϕ threshold (1560 MeV/c); c) at 1580 MeV/c, where the yield of ϕ was expected to be a maximum; and d) at 1620 MeV/c, to collect ϕ produced at higher p^* values. As far as the ϕ is concerned, the two latter momentum regions correspond to the regions B and C respectively of the efficiency plot of Chapter 5. At each momentum setting, the four hodoscope channels, 4-7 inclusive, were employed in the data taking.

The plot of the number of K^+K^-n events per pion as a function of beam momentum (called the 'yield curve') which was obtained over the momentum range covered above K^+K^- threshold, is shown in Fig.7.1. The presence of the ϕ is indicated on this by the sharp increase in counting rate as the momentum is raised from just below the ϕ threshold to $\sim$ 20 MeV/c above; the presence of the resonance is also

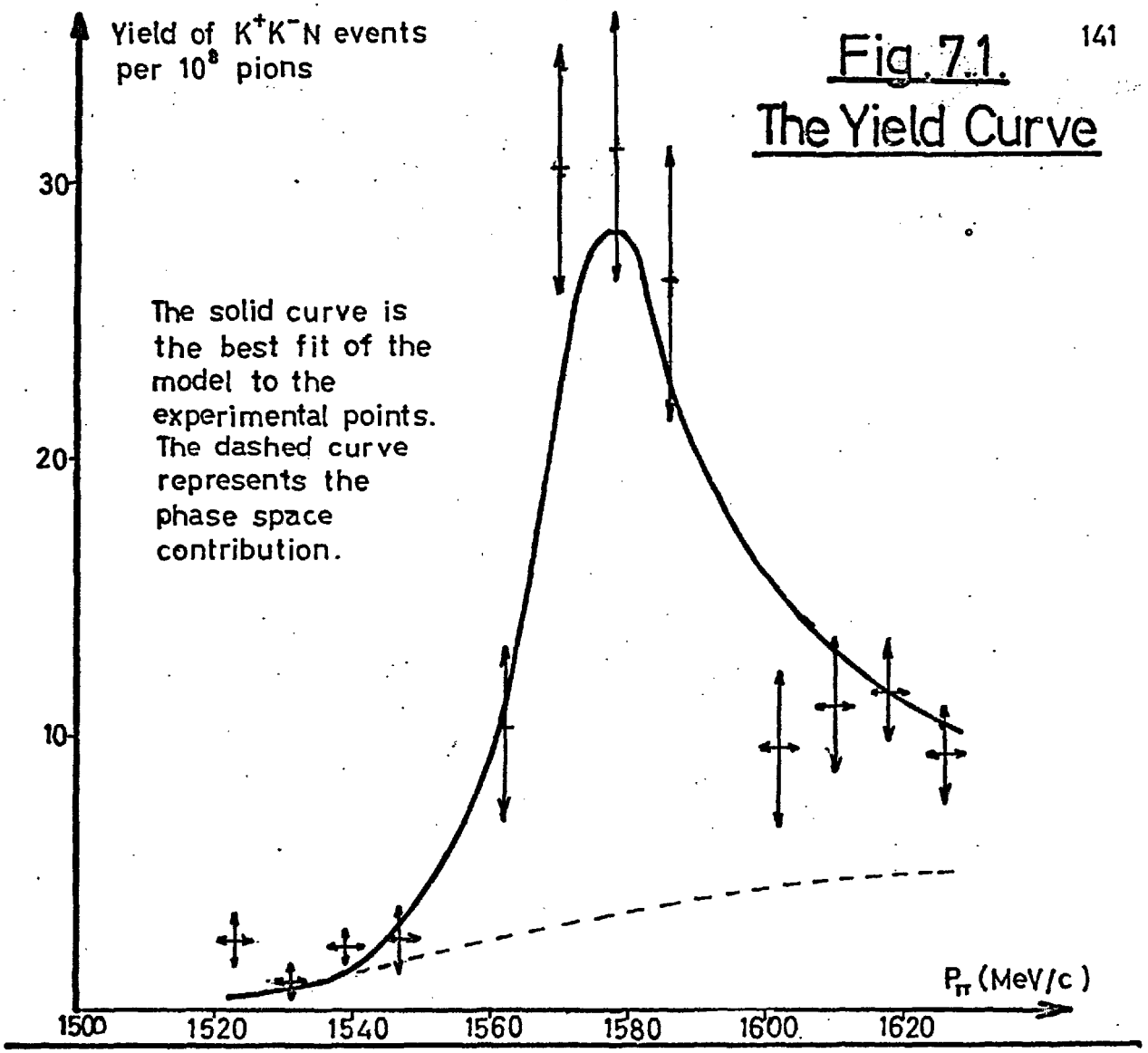

Fig. 7.1. The Yield Curve

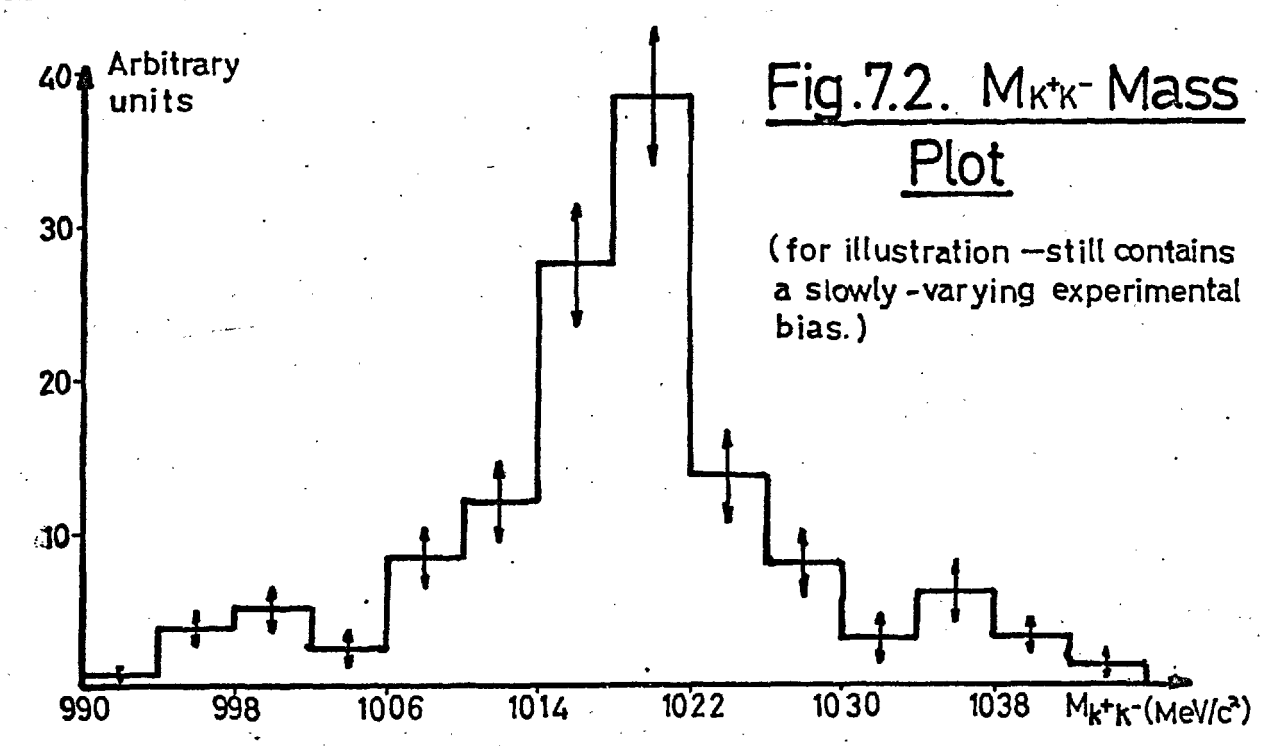

Fig. 7.2. $M_{K^+K^-}$ Mass Plot

(for illustration —still contains a slowly-varying experimental bias.)

illustrated on the more familiar mass plot (Fig.7.2), by the large peak at ~ 1020 MeV/c^2. The counting rate below ϕ threshold is seen to be small compared to that above, indicating a (slowly-varying) K^+K^- background signal smaller than the ϕ signal over the momentum range covered above the ϕ threshold.

The model used to try to describe the behaviour of the experimental data in the mass range covered was that of a Breit-Wigner resonance in the K^+K^- system with the known mass (1018.6$\pm$0.5 MeV/c^2) and width (4$\pm$1 MeV/c^2) of the ϕ, with a production cross-section proportional to p*, and displaying isotropy in production and decay. This resonance was supposed to be superimposed on a slowly-varying K^+K^- background which, since the experimental background outside the ϕ region promised to be small compared to the ϕ, was initially taken as being distributed according to K^+K^-n phase space.

In the procedure adopted for the data analysis, this model was first fitted to the yield curve to obtain estimates of the total amounts of ϕ and phase space background present at each momentum. Until the assumptions implicit in the model were checked, however, these estimates could be regarded only as approximate. The shapes of the theoretical ϕ and phase

space yield curves were known separately from the Monte Carlo computations; in the fit, the relative amount of each was varied until χ^2 minimised.

The fit indicated that the ϕ so dominated the background in the 1580 MeV/c region, that the average contamination of ϕ with background in the 4 hodoscope channels at 1580 MeV/c, was only ~10%. Also, the 1540 MeV/c data, being below ϕ threshold, were almost all K^+K^- background. Data at these two momenta therefore gave almost clean samples of ϕ and K^+K^- background respectively, and only at 1620 MeV/c did the contributions of ϕ and K^+K^- background become comparable. It therefore seemed reasonable to treat these three sets of data separately initially, and to combine them later.

7.2 Comparison of experimental and theoretical distributions

This section describes how the assumptions of the model were checked, using sets of experimental distributions constructed separately from 1540, 1580, and 1620 MeV/c data, for the reasons explained in 7.1. At each of these three momenta, a set of theoretical distributions was also produced. The relevant theoretical and experimental distributions were then compared quantitatively using the goodness of fit test (the significance level being taken as 1%). The number of events used

to construct the theoretical Monte Carlo distributions was, on average, about ten times the number in the corresponding experimental distributions. In the theoretical distributions, ϕ and phase space data were combined at each momentum in the proportions indicated by the fit to the yield curve.

a) 1540 MeV/c data

The data represented an almost pure sample of the K^+K^- background in the mass range 990-1010 MeV/c^2, produced at fairly low p* values (40-140 MeV/c), and consequently covering only a small Δ^2 range (0.3-0.7 GeV^2/c^2) (Δ^2 is the square of the four momentum transfer to the neutron). The distributions obtained are shown in Fig.7.3. Only 21 'unambiguous' K^+K^-n events were obtained at this momentum setting. The distributions of the c.m.s. production cosine, the K^+K^- rest system decay cosine, and the Treiman-Yang angle, were all consistent with the isotropy demanded by the phase space part of the model being tested here. The experimental and theoretical p* plots also agreed well.

b) 1580 MeV/c data

According to the initial fit to the yield curve, the 1580 MeV/c data consisted of almost 90% $\phi \rightarrow K^+K^-$ events. These events were produced mainly in the mass range 1006-1030 MeV/c^2,

Fig.7.3. 1540 MeV/c distributions

(21 events .)

——— = experimental distribution
- - - - = theoretical distribution

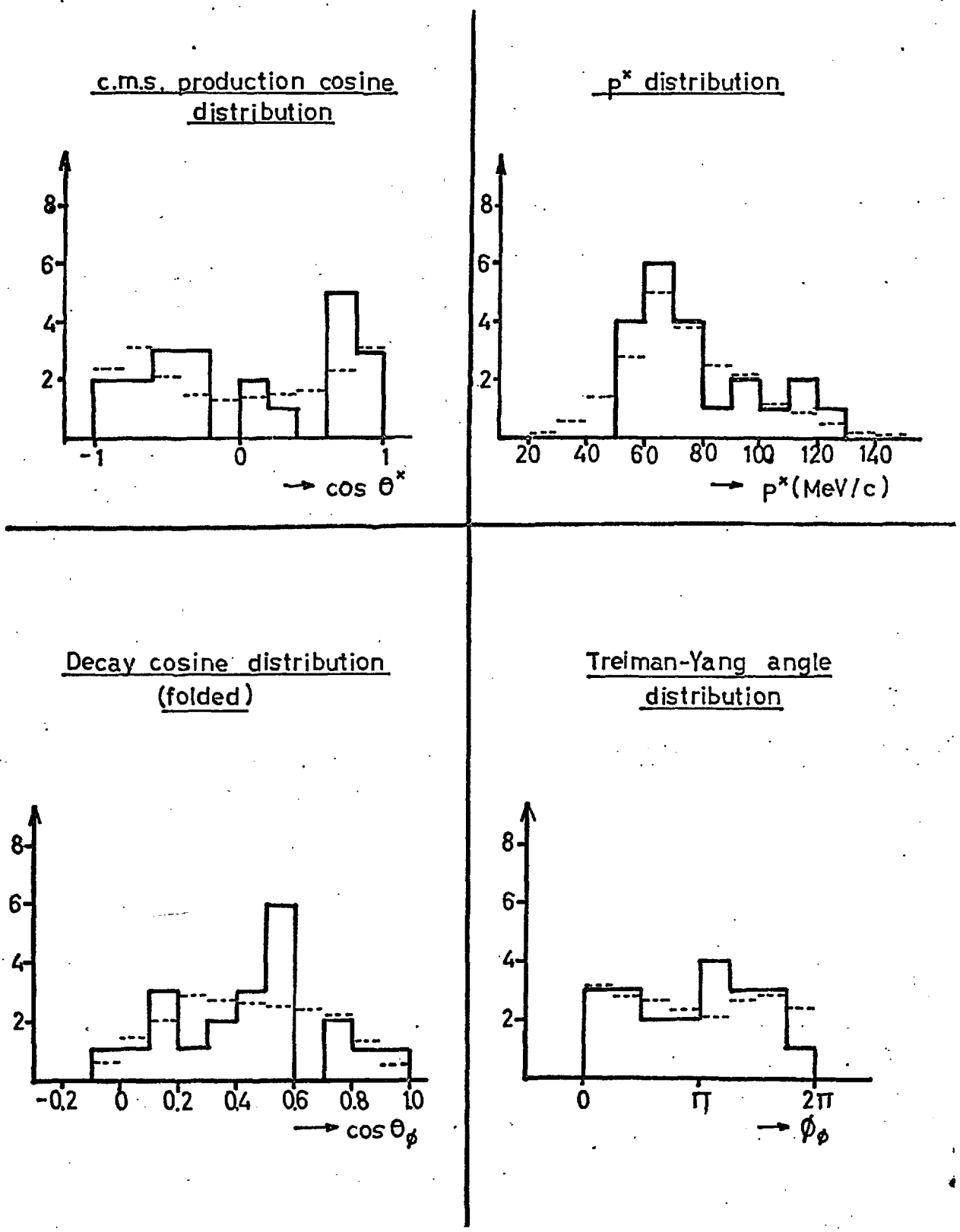

p* range 30–140 MeV/c, and Δ^2 range 0.3–0.7 GeV/c^2. The experimental distributions, containing 151 events, are shown in Fig.7.4. The distributions from the model again agreed well with the experimental distributions, indicating that, in this p* range at least, the model for ϕ production and decay was a good description of the experimental situation.

A histogram of the invariant mass of the system consisting of the neutron and the faster kaon in the laboratory, compiled using the 1580 MeV/c events, also compared well with its theoretical counterpart, and revealed no unexpected structure (Fig.7.4(b)). The mass range of this system covered in the experiment was 1430 to 1470 MeV/c^2, a region seemingly free of any known resonances in the KN system.

e) <u>1620 MeV/c data</u>

The amounts of ϕ and K^+K^- background became comparable at this momentum. The ϕ collected was produced in region C of the efficiency plot of Chapter 5. The apparatus was therefore severely biased against the ϕ; in particular, the cos θ^* distribution had split into the two characteristic peaks, at $\theta^* \sim 0^\circ$ (low $\Delta^2 = 0.2 - 0.4$ GeV^2/c^2), and $\theta^* \sim 180^\circ$ (high $\Delta^2 = 0.7 - 1.0$ GeV^2/c^2). The p* range of the collected ϕ was $\sim$ 100–210 MeV/c. Most of the K^+K^- background consisted of masses higher than the central ϕ mass, produced in region B of

Fig.7.4. 1580 MeV/c distributions (151 events)

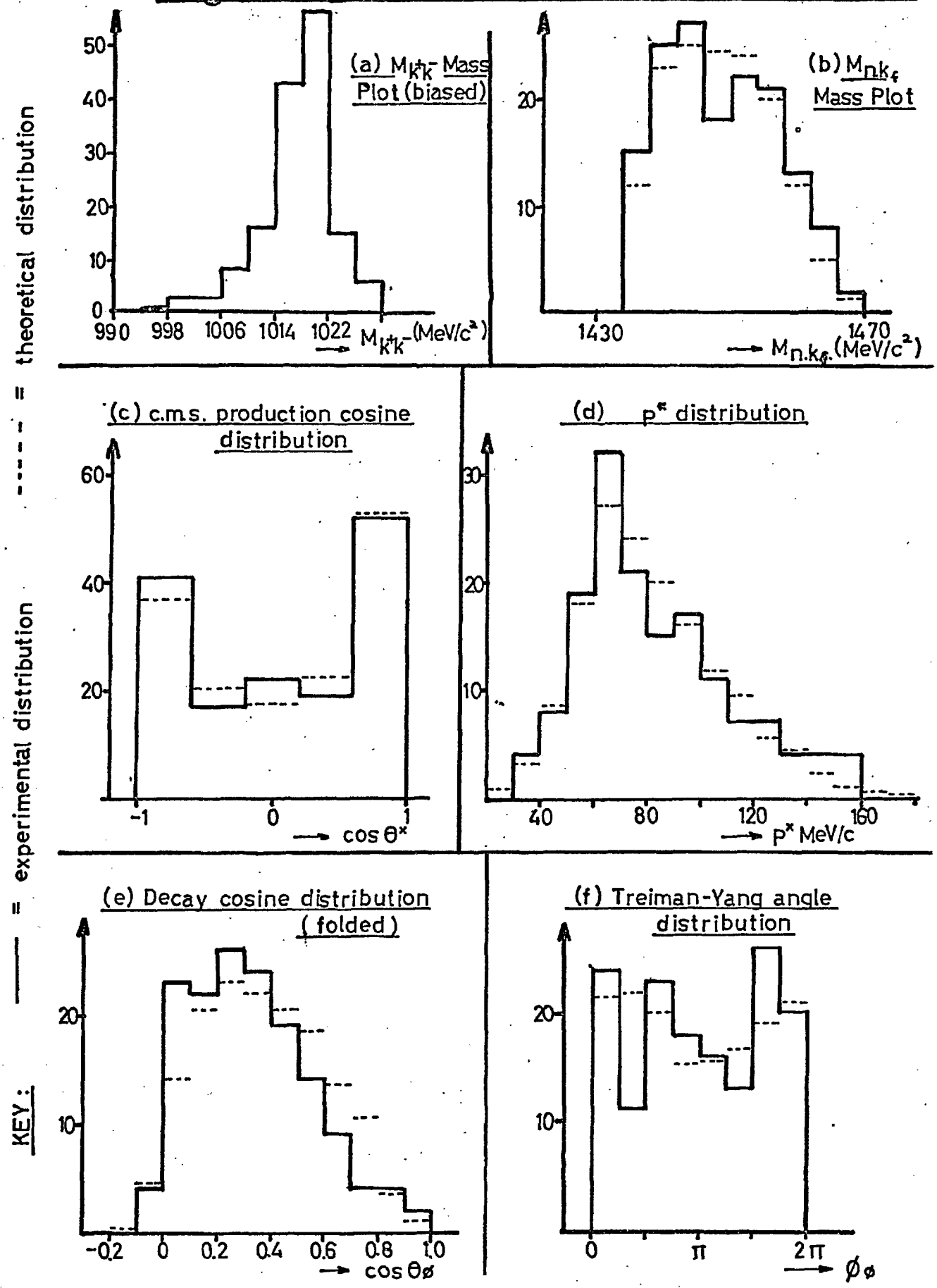

the efficiency plot. These high masses tended to fill up the central part of the cos θ^* plot, away from the two peaks. The bias of the apparatus therefore afforded a partial separation of the background and ϕ events.

The experimental distributions at 1620 MeV/c, containing 72 events, are shown in Fig.7.5; again, theory and experiment agreed quite well. In particular, the cos θ^* plot gave a good fit, indicating that the proportions of ϕ and phase space had been correctly chosen, since the centre of the plot is sensitive to the amount of phase space, while the two peaks at the extremities are sensitive to the amount of ϕ. The only exception to this good agreement was the p* plot, which did not give a very good fit (4% χ^2 probability on 6 degrees of freedom) because of the poor agreement above $p^* = 160$ MeV/c. The small peak of seven events at $p^* > 200$ MeV/c could be partly explained by the fact that the non-K^+K^- background distribution had not been subtracted, for reasons previously explained. From the evidence of the rejected events at 1620 MeV/c, about 1 event with $p^* > 200$ MeV/c might be expected to be non-KK out of the total of 72 events. Individual inspection of the 7 events indicated 3 of them were probably non-KK. Due to this effect, and the poor statistics above $p^* = 160$ MeV/c, it seemed unreasonable to depart from the linearity assumption on the evidence

Fig. 7.5 . 1620 MeV/c distributions.

(72 events)

——— = experimental distribution

- - - - - = theoretical distribution

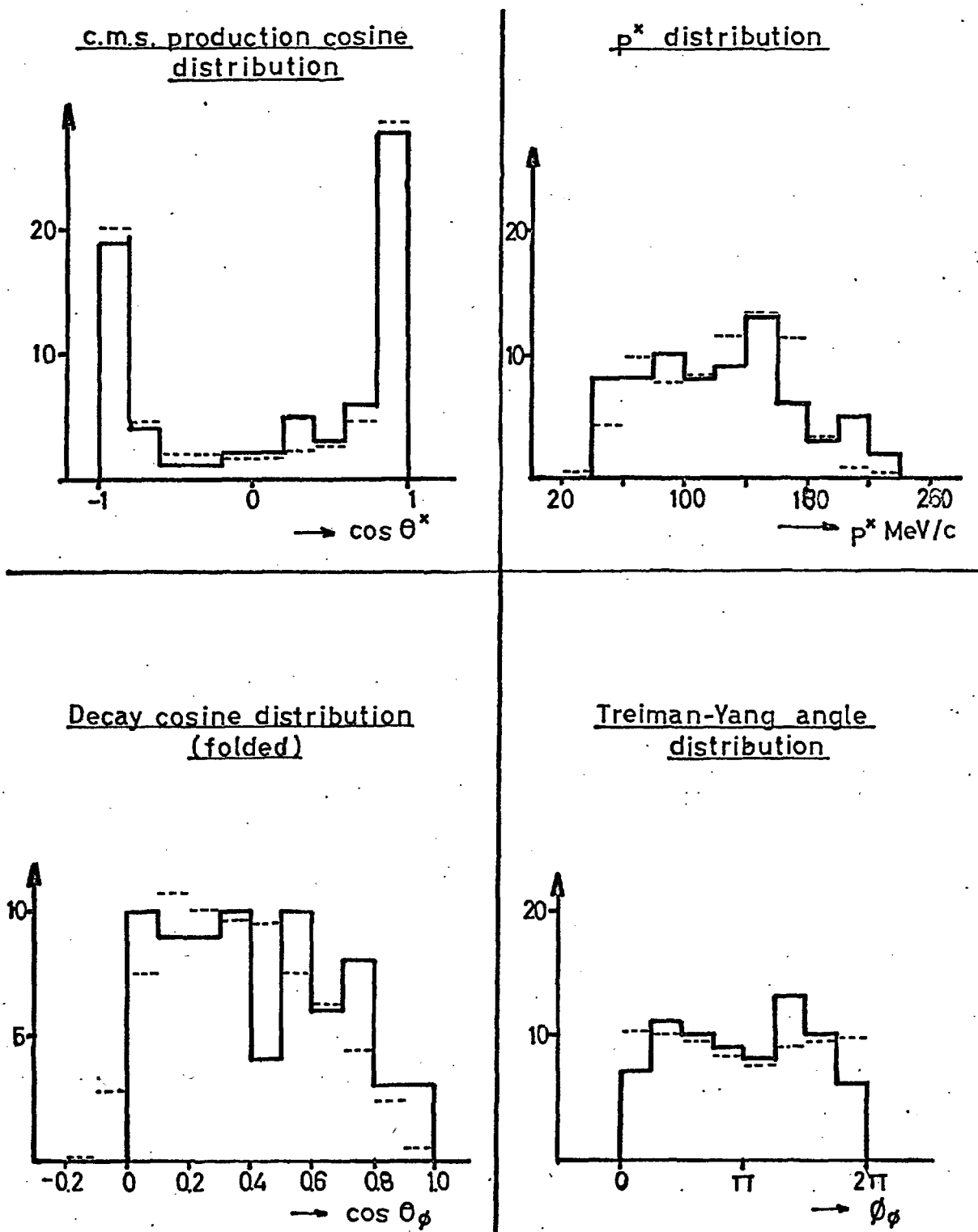

of this distribution. Some clarification on the matter came from further analysis, as will be described, and at this stage the assumption of linearity was maintained.

The K^+K^- phase-space events at 1620 MeV/c were produced in mass and p* regions not investigated in the 1540 MeV/c run. Therefore it was strictly necessary to assume that this background was still phase-space-like at 1620 MeV/c; this assumption, needing to be only loosely satisfied in the 1580 MeV/c data, became more critical here because of the higher proportion of phase space events at 1620 MeV/c. From the agreement obtained above, there seemed no reason to doubt this assumption; however, it was possible to perform at least partial checks on its validity, and this was done. Because of the bias effect explained above, an almost pure sample of K^+K^- background events could be obtained by choosing events lying inside a 'gate' in the cos θ* plot of $-0.6 < \cos\theta^* < 0.8$. These events consisted mainly of masses in the range 1030 - 1045 MeV/c^2. The distributions of 29 such events were found to agree well with the phase space model. The total number of K^+K^-n events per pion inside the gate also agreed well with the predicted number. More quantitatively, when a 'phase space yield curve' was constructed from the data in the three lowest 1540 MeV/c channels, and

from the cos θ * gate data at 1620 MeV/c (with all 4 p_π channels combined to increase statistics), and the four points so formed were fitted with the theoretical phase space yield curve (allowing only the amplitude to vary), the best fit gave an acceptable χ^2 probability of 18% (see Fig.7.10). This last test had the merit of being free of any uncertainties due to the presence of the ϕ.

For the background events in this mass range, at least, the original assumption seemed justified.

7.3 Some other possibilities

Though the data analysed appeared consistent with the model, other possibilities needed to be examined.

The combined data from the 1580 MeV/c and 1620 MeV/c runs were used to further investigate the decay cosine distribution, which might have yielded information on the exchange mechanism operating in the ϕ production process. As discussed in Chapter 1, ϕ production through ρ exchange might lead to a $\sin^2\theta_\phi$ form of distribution.

On examination of the 1580 MeV/c data, a fit of $\sin^2\theta_\phi$ to the decay cosine distribution in fact gave a better fit than the isotropic model had done. However, at 1580 MeV/c there was an unfavourable experimental bias against events with $\cos\theta_\phi > 0.6$, since these events had an associated slow kaon

which tended to stop in the Cerenkov-E-counter system. This range of cos θ_ϕ was just that where differences between a $\sin^2 \theta_\phi$ and isotropic distribution would be expected to show up, so that the 1580 MeV/c data were not very sensitive to this test. The bias could be removed to a large extent for a certain sample of the 1620 MeV/c data, namely those events which had $M_{KK} < 1030$ MeV/c^2 (to give a 75% pure sample of ϕ) and where $0.8 < \cos \theta^* < 1.0$ (so that both kaons generally had enough energy to pass through the Cerenkov-E-counter system). The $\sin^2 \theta_\phi$ hypothesis, tested on a sample of 29 such events, gave $< \frac{1}{2}\%$ χ^2 probability, compared with 45% for the isotropic model, so that for this particular sample of ϕ at least (low Δ^2, 0.2-0.4 GeV^2/c^2), the pure $\sin^2 \theta_\phi$ hypothesis could be rejected. (In fact, the inclusion of any $\sin^2 \theta_\phi$ term in the fit, made the fit worse - the best fit to this sample of a simple $1 + a \sin^2 \theta_\phi$ model for the decay cosine distribution gave a value for $a = -0.5 \pm 0.5$). It seemed unlikely that the decay angular distribution of events not contained in this sample would be radically different from that of those in the sample; more convincing evidence supporting isotropy was supplied by the Hess[41] results, where the decay cosine distribution was found to be consistent with isotropy and not with a $\sin^2 \theta_\phi$ form under what appeared to be less severe biases than ours.

In the subsequent analysis, the decay cosine was therefore taken as being isotropically distributed.

The apparent more or less linear dependence of the production cross-section on p* also needed further examination. Since, at p* > 100 MeV/c or so, the apparatus only collected ϕ which had been produced with cos θ * near 1 or -1, any positive terms in powers of $\cos^2 \theta^*$ in the cos θ * distribution at these higher p*, for instance, were indistinguishable from a cross-section increasing faster than p* (e.g. $\sigma = Ap^* + Bp^{*2}$) here. It was possible that observed linearity was due to a cancellation of two such effects occurring in this p* region e.g. a $\sigma = Ap^* - Bp^{*2}$ production cross-section cancelling with a $1 + b\cos^2\theta^*$ form of angular distribution. Such fortituous cancellation was unlikely, however. Also, if the presence of S and P waves only was assumed, any P-wave producing a $\cos^2\theta^*$ term would have been expected to interfere with the dominant S-wave, producing in general non-zero cos θ * terms.

Examination of the data at 1580 MeV/c and 1620 MeV/c revealed no serious anisotropy, however; a form of cos θ^* distribution $1 + a\cos\theta^* + b\cos^2\theta^*$ fitted to the 1580 MeV/c data gave a best fit $1-(0.07\pm0.10)\cos\theta^* + (0.20\pm0.20)\cos^2\theta^*$;

a form $1 + a \cos \theta^*$ fitted to the 1620 MeV/c ϕ data (in a higher p^* range than the 1580 MeV/c data) gave a best fit $1 - (0.02 \pm 0.15) \cos \theta^*$ (no $\cos^2 \theta^*$ term was necessary here as it was equivalent to isotropy).

7.4 Estimation of the proportionality constant A from the yield curve

At this stage, the experimental yield curve was used to make an estimate of the proportionality constant A governing the ϕ production cross-section. The yield curve itself is very model-dependent, but once the assumptions of the model have been checked, as in this case, fitting theoretical ϕ and phase space yield curves to the experimental yield curve, allowing only the amounts of each to vary, is a useful way of obtaining an accurate estimate of A, since the method makes good use of the available statistics, is convenient, and is sensitive to the value to A (it does not include the smoothing effects of the t_n error and the kaon angle errors, encountered, say, in the determination of A from a mass plot, though it is true these errors have been used in fitting the events before they reach the yield curve).

The preceding analysis indicated that the model was quite consistent with the data, therefore the original fit of

theoretical ϕ and phase space yield curves to the experimental curve still held good (see Fig.7.1). Using this fit, the best value for A was determined from the formula

$$A = \frac{1}{F} \cdot X \cdot A_M \qquad \ldots 7.1$$

Here A_M is the value of the proportionality constant used in the Monte Carlo programme (1 μbarn/MeV/c), F is the correction factor calculated in 6.7, and X is the 'best fit' value of the proportion of experimental ϕ to Monte Carlo ϕ, obtained from the yield curve; in this case X was 1.69×10^{-2} ($\pm$14%). Then

$$A = 0.28 \pm 0.07 \quad \mu\text{barn/MeV/c}$$

This value assumed, however, that the calculation of neutron counter efficiency used (see 6.7) was correct. The error on X was mainly statistical. The contributions to the error on X due to the error in the ϕ width, the p_π errors described in section 6.4, the Monte Carlo errors of section 4.2, and the error on the spread in beam momentum in a hodoscope channel, were all small compared to the statistical error. The error in the momentum spread could be made small as a result of the calculations described in Appendix 1.

However, the χ^2 probability of the original fit to the yield curve used to determine A was only 6%, on 10 degrees of

freedom. No explanation could be found for this other than statistical fluctuation. To see if the fit could be improved using a model for the ϕ production cross-section of $\sigma = Ap^* + Bp^{*2} = \frac{1}{F}(\lambda p^* + Yp^{*2})$, a Monte Carlo yield curve with $\sigma \propto p^{*2}$ for the ϕ was generated, and a new fit to the yield curve attempted, this time with Y as an extra free parameter. The best fit to this gave a χ^2 probability of 8% on 5 degrees of freedom. In the fit, X increased to $(2.60 \pm 0.5) \times 10^{-2}$ μbarn/MeV/c, and Y was $-(1.0 \pm 0.5) \times 10^{-4}$ μbarn/(MeV/c)^2. Since there was negligible improvement in the χ^2 probability using this more sophisticated model, and since there seemed a no more sensitive way of examining the p^* dependence of σ from our data, the original simple linear model was retained.

Uncertainties in the positions of the yield curve points on the p_π axis due to the non-zero p_π errors (derived and explained in 6.4), were also found to have little effect on the χ^2 value, since these errors were smaller than the statistical errors, and were smallest at the most sensitive parts of the curve.

In the previous experiment performed by our group, the yield curve was used to place on upper limit on the width of the

η meson in a manner described in (11, 13), by treating the resonance width and the proportionality constant A as the only unknown quantities in the model used, and adjusting the width in the theoretical yield curve until the best fit to the experimental yield curve was obtained. The analysis of the present experiment was carried out using a width of 4 ± 1 MeV/c^2 for the ϕ, but an attempt was made to improve upon this accuracy by subjecting the data to a similar analysis. Unfortunately our results were not sensitive enough to do this; we could only observe that nothing in our data suggested this width was unreasonable.

From the result of the analysis in section 6.4, it was also possible to make an estimate of the ϕ mass. This was found to be 1018.6 ± 2.5 MeV/c^2, the error coming from the uncertainty in the absolute value of the central p_π momentum of the 1580 MeV/c data; this value is in good agreement with the accepted value.

7.5 The experimental p^* dependence of the ϕ production cross-section

Figure 7.6 and Table 7.1 illustrate the actual experimental dependence of the ϕ production cross-section σ upon p^*. This was unfolded from an experimental histogram of the number

Fig. 7.6. P^* dependence of Ø production cross-section

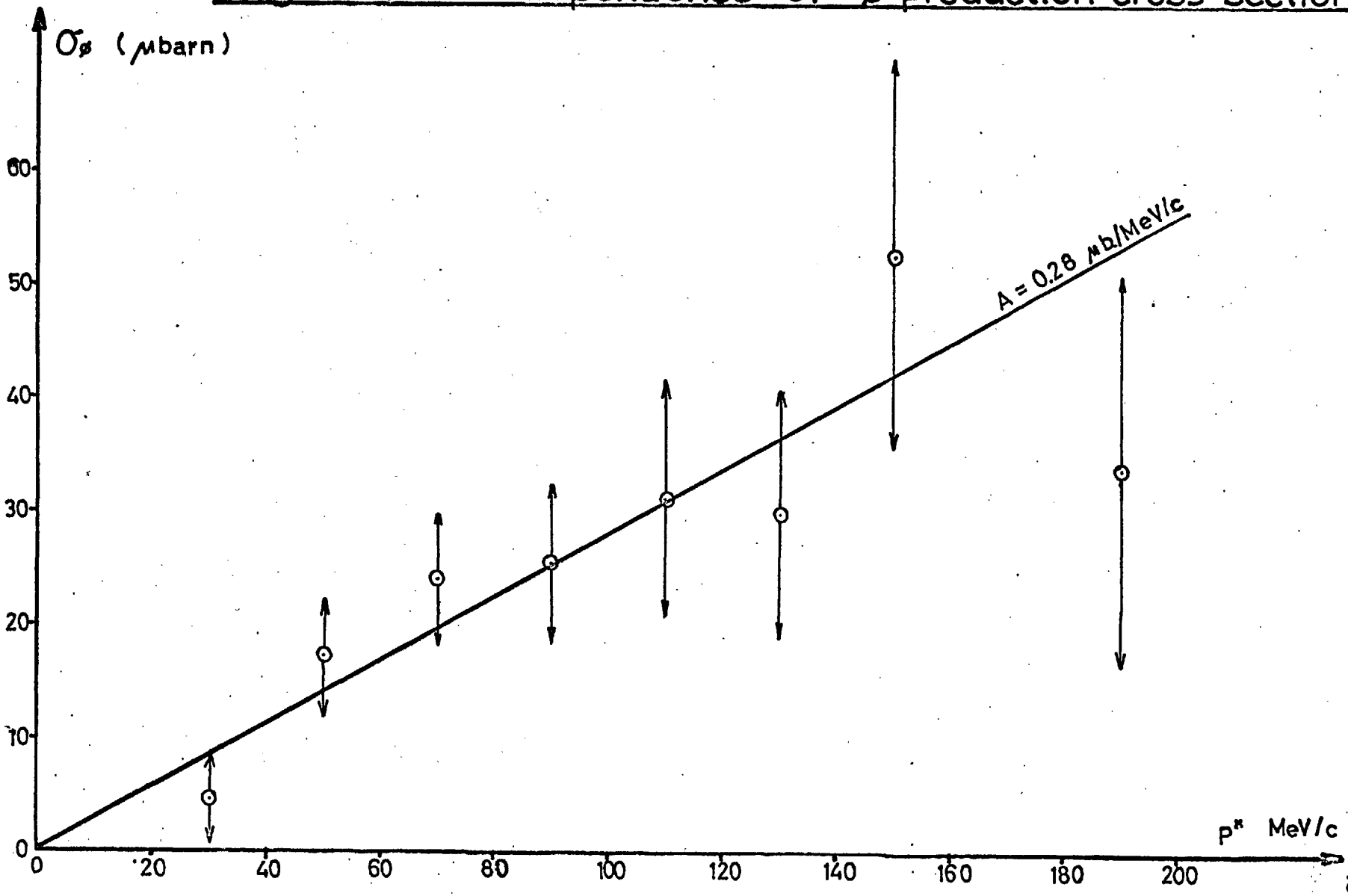

of events per pion per 20 MeV/c p^* bin as a function of p^*, constructed from all the data above ϕ threshold, by subtracting from this histogram a similar but theoretical histogram of phase space data, and then comparing the resulting histogram with a theoretical histogram for the ϕ. The proportions of ϕ and phase space used in the theoretical histograms were taken from the fit to the yield curve (using $\sigma \propto p^*$). Except at the highest p^* points, where the background subtraction errors became comparable, the errors were mainly statistical (the 18% error on the constant factor F has been included). Since each p^* bin of the theoretical ϕ plot had a value of σ associated with it ($\sigma = Ap^*$), comparison of theoretical and experimental numbers in the same p* bin gave a value for the experimental cross-section at that p*. Strictly speaking, the resolution of the apparatus should have been removed from both the theoretical and experimental curves before the comparison was made, but it turned out that the resolution had hardly any effect, so this step was omitted. Due to poor statistics, the data above p* = 160 MeV/c was grouped under a single point. The solid straight line represents the slope 0.28 μ barn /MeV/c for comparison.

Table 7.1

p*(MeV/c) at centre of 20 MeV/c bin	ϕ production cross-section (μbarn)	Total error (μbarn)
30	4.7	$\pm$ 3.8
50	17.4	$\pm$ 5.0
70	24.1	$\pm$ 5.7
90	25.8	$\pm$ 7.1
110	31.2	$\pm$ 10.3
130	30.0	$\pm$ 10.8
150	52.8	$\pm$ 17.1
190	33.8	$\pm$ 17.0

7.6 Comparison and discussion

The first indication of ϕ production in $\pi^- p$ interactions came from Lee et al.,[42] who studied the reaction $\pi^- p \rightarrow \pi^- p K^+ K^-$ at 3.5 GeV/c, and produced an upper limit for the ratio

$$\frac{(\pi^- p \rightarrow \pi^- p \phi)}{(\pi^- p \rightarrow \pi^- p \omega)} \leqslant 0.012$$

at that energy.

Abolins et al.[43] have investigated ϕ production in the charge symmetric reaction $\pi^+ n \rightarrow \phi p$ at beam momenta < 2.3 GeV/c, using a deuterium bubble chamber. On the basis of 38 events ($\phi \rightarrow K^+K^-$ or $K_1^0 K_2^0$), containing an estimated 20% unsubtracted

background, they found a ϕ production angular distribution consistent with being isotropic, but do not show decay distributions.

The experiment of Hess et al.[41] seems to be the only previous study of the reaction $\pi^- p \rightarrow \phi n$. They investigated $\pi^- p \rightarrow K^+ K^- n$ in a hydrogen bubble chamber at beam momenta < 2.3 GeV/c , over a somewhat larger $\Delta^2(n)$ range than ours. Their results are summarized in Fig.7.7, and in general compare well with ours. The production cosine (Δ^2 distribution), decay cosine, and Treiman-Yang angle for 42 events in the mass range 1005-1035 MeV/c^2 were all consistent with isotropic production and decay (though they say a better fit to the decay cosine distribution was obtained when linear and quadratic terms were included). They did not, however, observe the $\sin^2\theta_\phi$ form of decay cosine distribution that might be expected from ϕ production through ρ exchange, but point out that it has been shown that absorptive effects could modify this distribution significantly.[44] For our results, it is possible that the absorption model would not be applicable because of the low beam momentum, which limits the number of partial waves produced.

Hess observes that his production and decay distributions are similar to those reported by Kraemer et al.[45] for

Fig. 7.7. Results of Hess et al.

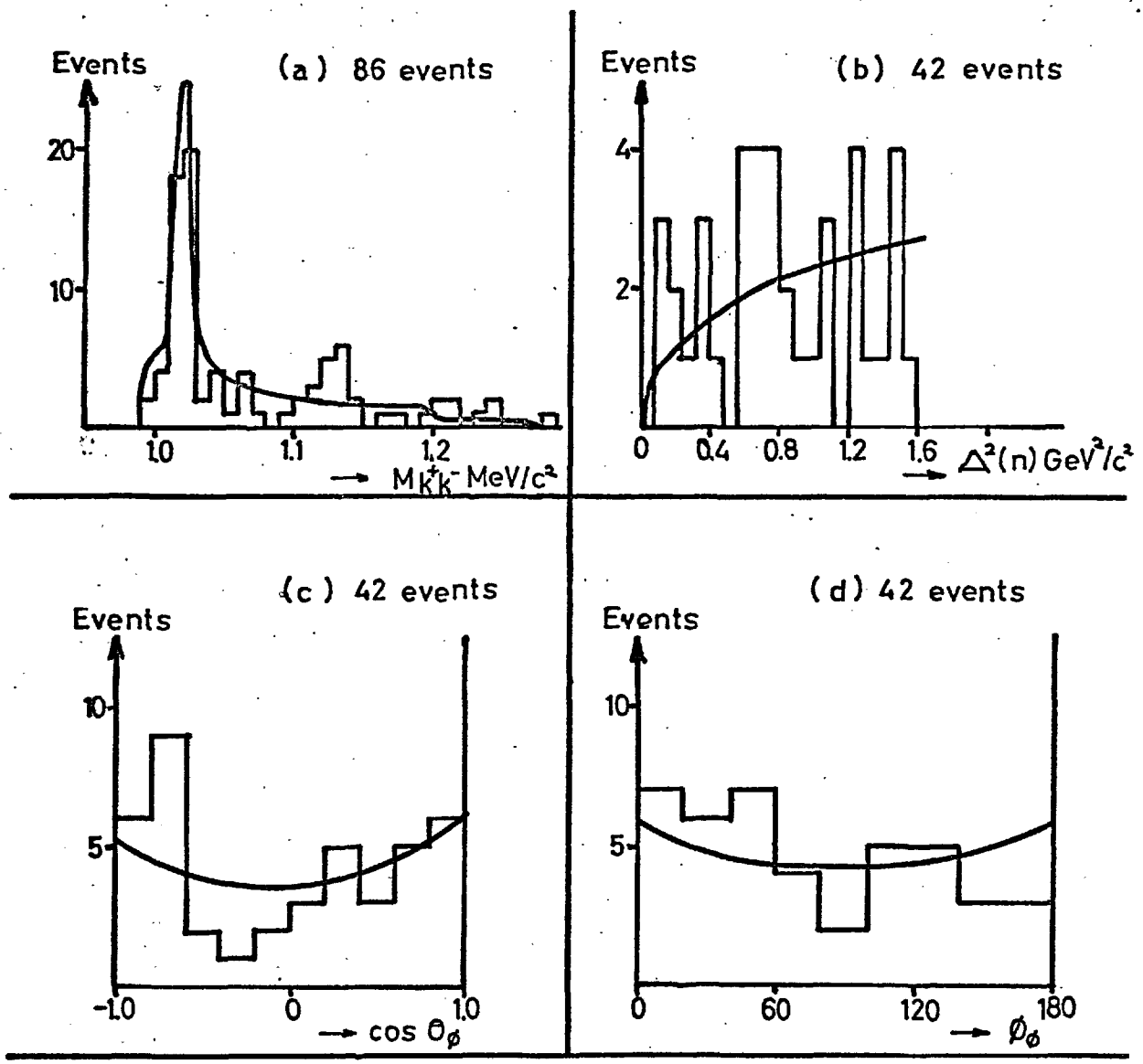

Data from K^+K^-N final states at beam momenta below 2.3 GeV/c . (a) K^+K^- effective mass distribution . The curve is for 40 % ϕ production , 40 % phase space , and 20% threshold enhancement . (b), (c),(d) : histograms of (b) $\Delta^2(n)$ (c) decay cosine , and (d) Treiman-Yang angle for events with $1005 \leqslant M_{K^+K^-} \leqslant 1035$ MeV/c^2 . Curves for (b),(c),(d), are Monte Carlo distributions for isotropic production and decay angular distributions .

$\pi^+ n \rightarrow \omega p$ at 1.23 GeV/c. Kraemer et al. also do not find a decay cosine distribution of a $\sin^2\theta_\phi$ form (ρ exchange is the only single meson exchange allowed in the latter reaction also). Liu and Singer,[46] in a study of $\pi^+ n \rightarrow \omega p$ near threshold, have shown that important contributions to this production process might be expected from a nucleon pole diagram . It is possible that a similar explanation for ϕ production just above threshold might be correct.

The results of Hess on the p^* dependence of the ϕ production cross-section have been combined with ours in Fig. 7.8. The only Hess point to lie within our p* range (20-200 MeV/c) does not appear incompatible with our results. On the basis of 14 $\phi \rightarrow K^+K^-$ events, Abolins et al. quote a ϕ production cross-section of 23 ± 10 μbarn, but this has been averaged over the p* range 0-650 MeV/c.

Cross sections for $\pi^+ n \rightarrow \omega p$ and $\pi^- p \rightarrow \phi n$ may be related through SU(3) and charge symmetry. Hess et al. have compared their data with the available data on $\pi^+ n \rightarrow \omega p$.[45,47] This is illustrated in Fig.7.9. (taken from ref.(41)). They find that the energy dependences correspond roughly when the ordinate for $\pi^- p \rightarrow \phi n$ is increased by ~ 50 (they observe that other experiments [42,48,18] suggest the ratio of cross-sections for

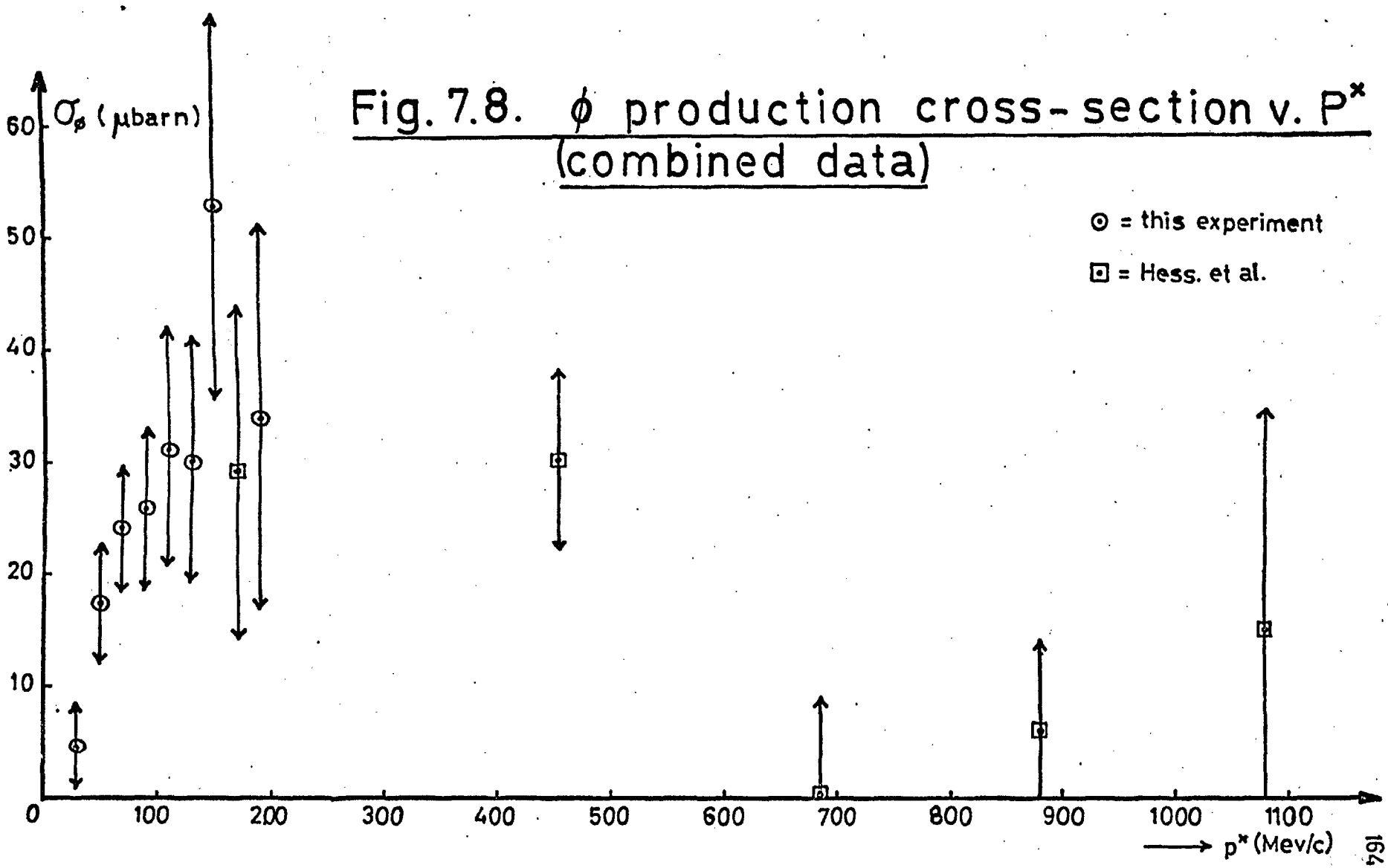

Fig. 7.8. ϕ production cross-section v. P^* (combined data)

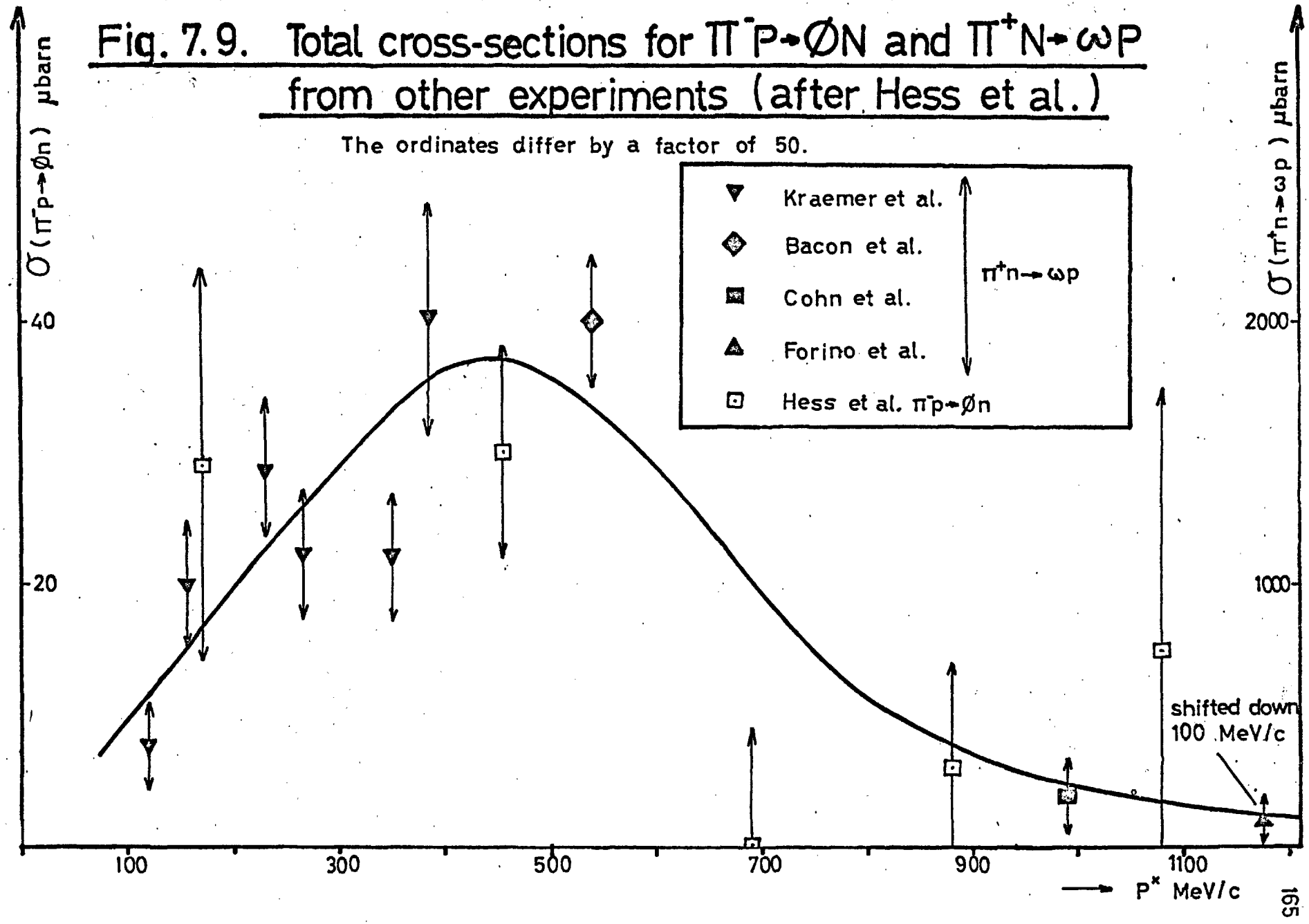

Fig. 7.9. Total cross-sections for $\pi^- p \to \emptyset N$ and $\pi^+ N \to \omega P$ from other experiments (after Hess et al.)
The ordinates differ by a factor of 50.
Kraemer et al.
Bacon et al.
Cohn et al.
Forino et al.
Hess et al. $\pi^- p \to \emptyset n$
$\pi^+ n \to \omega p$
$\sigma(\pi^- p \to \emptyset n)$ μbarn
$\sigma(\pi^+ n \to \omega p)$ μbarn
40
20
2000
1000
shifted down 100 MeV/c
100
300
500
700
900
1100
P^* MeV/c

$\pi^+p \longrightarrow \omega N^{*++}$ and $\pi^+p \rightarrow \phi N^{*++}$ is ~ 70). The agreement seems somewhat worse if our points are included in the comparison, however; there is some hint that the peak in the cross-section for $\pi^-p \rightarrow \phi n$ occurs at a lower p* value than that for $\pi^+n \rightarrow \omega p$. The ordinate for our data must be increased by ~ 20 to correspond to the initial rise of the Kraemer data. (Inclusion of the more recent $\pi^+n \rightarrow \omega p$ data of Abolins et al.[43] into the Hess curve does not alter these conclusions significantly).

7.7 K^+K^- background analysis

This last section describes attempts made to find a non-phase-space-like structure in the K^+K^- background. This had previously been treated quite successfully using a phase space model, deviations from the model having been considered small enough to be neglected in the ϕ analysis.

As stated in Chapter 1, there is evidence of a broad enhancement in the $K_1^oK_1^o$ mass spectrum just above threshold, which should also appear in the K^+K^- mode. Some observers,[41,24] working near our energy, have explained this using a one-pion-exchange model with strong S-wave scattering in the $K\bar{K}$ system. Chew and Low[49] have shown that the double-differential cross-section for this is dominated in the limit $\Delta^2 \rightarrow -M_\pi^2$ by

the term

$$\frac{d^2}{d\Delta^2 dM^2} = \frac{f^2}{2\pi} \cdot \frac{M.k_\pi}{M_\pi^{\,2} p_\pi^{\,2}} \cdot \frac{\Delta^2}{(\Delta^2 + M_\pi^{\,2})^2} \cdot \sigma(\pi\pi \longrightarrow K\bar{K}) \quad \ldots 7.2$$

where M is the effective mass of the $K\bar{K}$ system, f is the π -N coupling constant ($x2^{\frac{1}{2}}$ for π^+ exchange), k_π (or k_K) is the momentum of either pion (or either kaon) in the $\pi\pi$ c.m. system, p_π is the beam momentum, and $\sigma(\pi\pi \longrightarrow K\bar{K})$ is the $K\bar{K}$ production cross-section at energy M.

Using the zero effective range approximation and taking into account only the channels $K\bar{K} \longleftrightarrow K\bar{K}$ and $K\bar{K} \longleftrightarrow \pi\pi$ the S-wave $K\bar{K}$ production cross-section for pure I = 0 initial and final states can be written as -

$$\sigma_o(\pi\pi \longrightarrow K\bar{K}) = 4\pi \frac{k_K}{k_\pi^{\,2}} \cdot \frac{2b_o}{(1 + b_o k_K)^2 + a_o^2 k_K^2} \quad \ldots 7.3$$

where $A_o = a_o + ib_o$ is the I = 0, S wave, $K\bar{K}$ scattering length. Taking into account the isotopic composition of the initial $\pi^-\ \pi^+$ state, and saying (from the final charge state) that half the events will lead to the K^+K^- state[50], we obtain:

$$\sigma(\pi^-\ \pi^+ \longrightarrow K^+K^-) = \frac{1}{3} \cdot \frac{1}{2} \cdot \sigma_o(\pi\pi \longrightarrow K\bar{K}) \quad \ldots 7.4$$

Alexander et al.[24] found an adequate fit to their data using

$A_o = \pm$ (4 to 6) + ($\sim$i.0) fermi, and Hess et al.[41] (using no form factor) obtained adequate fits with $A_o = \pm$(1.5 to 10) + ($\sim$i.0) fermi also.

Other experimenters,[51] however, (chiefly working at higher energies), have explained the enhancement in terms of an S-wave Breit-Wigner resonance ($I^G(J^P) = 0^+(0^+)$) of mass near 1050 MeV/c^2, and width $\sim$ 50 MeV/c^2 (this has been called the S^* meson.

An attempt was made to analyse our background data in terms of both models (though the one-pion-exchange mechanism may not be dominant so near threshold) to see which model gave a better description of the data. The available data were necessarily rather scanty since the mass range covered was so small, and the background was swamped by ϕ over much of the range. Quantitative comparison was made with a yield curve comprised of the yields in the three lowest momentum channels at 1540 MeV/c, and the yield in the 1620 MeV/c cos θ^* gate (summed over all 4 p_π channels to increase statistics). This data contained very little ϕ. Monte Carlo yield curves were generated for the case of both the resonance and scattering length models. For the latter, the value of a_o was fixed at 5 fermi, and b_o was left as a parameter to be determined from the fit (the fit was not very sensitive to small changes in a_o about the 5 fermi value). The Monte Carlo

yield curves showed that the scattering length model had the effect of raising the 1540 MeV/c group of points relative to the 1620 MeV/c point, compared to the phase space curve, while the resonance model produced the opposite effect (see Fig.7.10). Thus simple deviations from phase space could be described using a mixture of one of these models and phase space (this is irrespective of whether or not the models had physical significance).

In the fitting process, the background was treated as a mixture of enhancement and phase space: that this was fair was borne out by the results of Hess (the solid curve of Fig.7.7(a) is 40% ϕ, 40% phase space, and 20% enhancement due to a large scattering length), and also by the results of fits to the data of a pure scattering length model (8% χ^2 probability) and a pure resonance model (4% χ^2 probability), compared to an 18% χ^2 probability for a pure phase space yield curve (all these on 3 degrees of freedom). The mixture was then fitted to the background yield curve. If the enhancement was treated as being due to a large scattering length, the best fit for the mixture had a χ^2 probability of 14% on 2 degrees of freedom, with the best value of $b = 0.15 \pm 0.20$ fermi. This was consistent with previous results. If the enhancement was

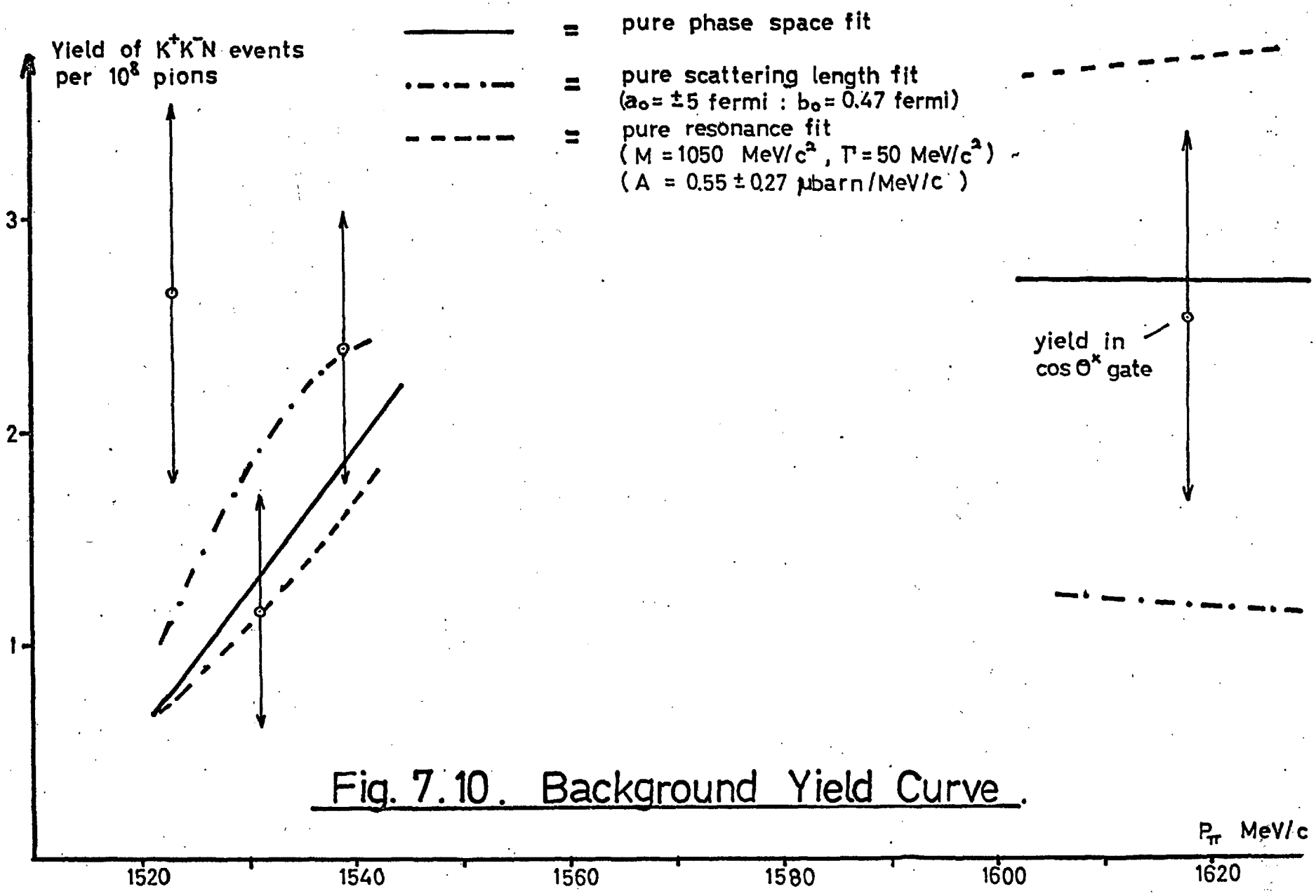

Fig. 7.10. Background Yield Curve.

treated as a resonance, the χ^2 probability was still 14% on 2 degrees of freedom, but the value of the parameter A governing the (assumed $\sigma = Ap^*$) resonance production cross-section was $A = -0.14 \pm 0.21$ μ barn/MeV/c i.e. though the error was consistent with a positive value for A, the fit had tried to subtract the resonance from the phase space. The most accurate measurement near our p* range (that of Hess), would indicate a cross section for the enhancement in the K^+K^- mode of ~ 15 μ barn at $p_\pi = 1.8$–2.2 GeV/c (this assumes $\sigma_{TE}(K^+K^-)/\sigma_{TE}(K_1^oK_1^o) = 2$, from the final $|K\bar{K}>$ charge state, but neglects differences in Q values). Both fits tried to raise the 1540 MeV/c theoretical points and lower the 1620 MeV/c point, compared to the phase space theoretical points.

Little information regarding the validity of the assumptions about the angular distributions made in the models describing the enhancement part of the mixture could be obtained from the experimental angular distributions, though no inconsistencies were apparent. At 1540 MeV/c, the Δ^2 range was so small that the $\cos\theta^*$ distributions predicted by the models were almost isotropic (and quite consistent with the data), and at 1620 MeV/c the ϕ dominated the distributions. The decay distributions for the S-wave enhancement could be expected to be isotropic, and therefore compatible with the observed distributions.

We could only conclude that the K^+K^- background in our data was adequately represented by a phase space model. However, it was possible that some enhancement was also present: of the two (assumed applicable) models proposed to describe this enhancement, the strong S-wave $K\bar{K}$ scattering model was favoured, though we could not reject the possibility of resonance formation.

APPENDIX 1

The Momentum Distribution in a Hodoscope Channel

It turned out that a knowledge of the momentum distribution in a particular hodoscope channel (i.e. the relative yield of particles in the channel as a function of their momentum) was of importance in any analysis of the experimental results. Consequently, calculations were made, using the IPSO FACTO programme, to determine what form deviations from a simple 'ideal' model could take. In this 'ideal' model, the assumptions made could be grouped into two categories. It was assumed -

a) the G-counters and their corresponding H-counters in a particular hodoscope channel, were at conjugate points of the triplet lens system for all momenta (i.e. no chromatic aberration): the G-counters were exactly matched in size (horizontally, by the triplet magnification) to the corresponding H-counters: BM2 was a perfect bending magnet.

b) all the G-counters in the channel emitted particles of all momenta uniformly and isotropically across their surface.

In this ideal case, the momentum distribution would have had the shape of an isoceles triangle, whose full width at half height (FWHH) would have been determined only by BM2 dispersion,

and the width of the hodoscope counters. For our arrangement, the FWHH of the triangle would have been 0.5% in momentum, with 0.5% momentum separation between the peaks of neighbouring channels.

In practice, many effects upset these assumptions. Factors affecting the assumptions in group (a) arose physically along the beam line after the G-counters. Thus the chief of these seemed to be (1) chromatic aberration in the triplet; (2) errors in the values of the triplet currents for a horizontal focus at the hydrogen target, mainly arising from the 'floating wire' calibration (called triplet current mis-setting); (3) other triplet aberrations; (4) staggering of the G- and H-counters along the beam axis; (5) scattering of beam particles in the S_2 counter (see Fig.3.1) and in the air between BM2 and the H-counters; and (6) non-uniformity of the flux linkage along the various paths allowed for particles traversing BM2, which would cause some particles to bend more or less than others of the same momentum, depending on which part of the magnet they traversed.

Factors affecting the (b) assumption arose before the G-counters. The most important of them was that (7) the horizontal width of the image of the target for one momentum

at the G's (2.5 cm) was not large compared with the width of the individual G-counters (0.8 cm). Thus the outside G-counter G (+2) (Fig.2.5). in channel 6 was only partly illuminated by the image of p_o particles, and, because of the momentum dispersion at the G's, even less (and eventually never) illuminated by images of higher momenta, so that the G (+2) H (-2) momentum distribution was strongly biased towards lower momenta, compared with the more or less fully illuminated inner GH combinations. This bias was balanced by an opposite bias from G (-2) H (+2), caused by the same effect, so that the summed distribution in channel 6 was not strongly biased, but no such compensation occurred in the outer hodoscope channels.

A possible consequence of the finite image width was that (8) the momentum distribution might have changed if BM1, normally optimized by equalizing the counting rates in hodoscope channels 5 and 7 on either side of the central channel, had been mis-set. In this case, G (-1), G (+1), G (+2), might have received all the p_o image, and G (-2) none at all. Again, for the small change of this example, a compensating effect would have occurred, since G (+2) would have got more p_o particles while G (-2) got less; but there should be less compensation for larger changes, or in outer hodoscope channels.

Lastly, (9), the machine target might not have been uniformly illuminated with protons over its horizontal width, in which case the pion illumination would have varied over the width of the target image. Factors such as chromatic aberration or misfocus of the doublet, machine field aberrations, and shift of target image during the pulse due to the machine field increasing slightly over the pulse length (a few mm's, at the G-counters), would serve chiefly to smear out the monochromatic images at the G-counters, and would thereby tend to satisfy assumption (b) more.

In the calculations, the central momentum was assumed to be exactly fixed by the BM2 current. This would not be true in practice, due to BM2 hysteresis and calibration errors; however, any error in the central momentum due to 'misdefinition' by BM2 can be regarded as equivalent to a current mis-setting in all other beam-line elements, and has been so treated here. This mis-setting was in fact small compared to mis-settings due to other causes.

IPSO FACTO calculations were made first on the 'correct' beam, which was defined as having only the assumption-violating factors (1), (7), and doublet chromatic aberration, present in it. Further calculations were then made, in which the factors

(2), (8), (9), were included, separately, in the 'correct' beam. The momentum distributions obtained were approximated to isoceles triangles, because deviations from this shape were generally small, and the shape was convenient mathematically for the experimental analysis. The free parameters for the 'fit' (by eye) of the triangle were its FWHH (δ), and its position on the momentum scale (C). Calculations were made for the central channel (channel 6), and for the extreme channel used in the experiment (channel 4).

For triplet current mis-setting, Q3 and Q5 currents were reduced by 1%, and Q4 current raised by 1%, so that the triplet underfocussed horizontally. A change of ~3% in Q4 current alone, would produce the same shift of the horizontal focus position. From the floating wire results, the r.m.s. error in the Q4 current value for the focus was $\pm$ 0.6%. However, it was possible to regard the effect of factors (3), (4), (5), (6) as being equivalent to a small Q4 current mis-setting. Factors (3)-(6) produced a finite image size at the H-counters, of a point object at the G-counters; this could be related to a change in Q4 current by finding the Q4 current change (from the focus condition) that caused the same horizontal image size. By this method, the effect of (5)

was found to be equivalent to an 0.8% change in Q4 current, the effect of (4) equivalent to an 0.6% change, and the combined effect of (3) and (6) equivalent to an 0.5% change. The combined effect of (3) and (6) was found by examining the image sizes obtained during the floating-wire measurements. If all these effects were added quadratically, the nett equivalent Q4 current mis-setting was 1.3%; this particular example was therefore a 2-2.5 standard deviation one.

For BM1 mis-setting, BM1 field was decreased 1%; a larger decrease would probably have been noticed during the data-taking, since the hodoscope channel counting rates were monitored to some extent.

For non-uniform proton illumination, the proton intensity distribution along the horizontal axis was assumed to be a gaussian intensity distribution of standard deviation 0.8 cm, centred 0.8 cm from the target centre. The intensity distribution along the vertical axis was taken as uniform. This was probably rather an extreme case of non-uniform illumination, considered owing to the difficulty of estimating the magnitude of non-uniformity, and the numbers come from the crude assumption that the protons are normally distributed across a proton beam about 3 cm wide, with the target situated where the intensity variation is a maximum.

The distributions obtained are shown in Figs. A1.1 and A1.2. It can be seen that, for the 'correct' beam, channel 6 had the FWHH δ of the ideal model ($\delta = 0.5 \pm 0.02\%$), while channel 4 was $\sim 8\%$ wider ($\delta = 0.54 \pm 0.02\%$). Factors (2)-(6) inclusive, treated as described above, caused a widening of $8 \pm 3\%$ in channel 6 ($\delta = 0.54 \pm 0.015\%$), and $4 \pm 3\%$ (and $\sim 5\%$ shift) in channel 4 ($\delta = 0.56 \pm 0.015\%$) (this assumes linearity for small changes in Q4 current). However, the non-uniform target illumination, and the 1% BM1 mis-setting, caused hardly any widening in either channel. It was assumed that these conclusions would not be affected if the above changes were made in the opposite direction.

As a result of this analysis, a value for the FWHH of $0.55 \pm 0.02\%$ was chosen for use in the experimental analysis. This was considered a reasonable compromise for the four hodoscope channels concerned.

Fig. A1.1. Channel 6.

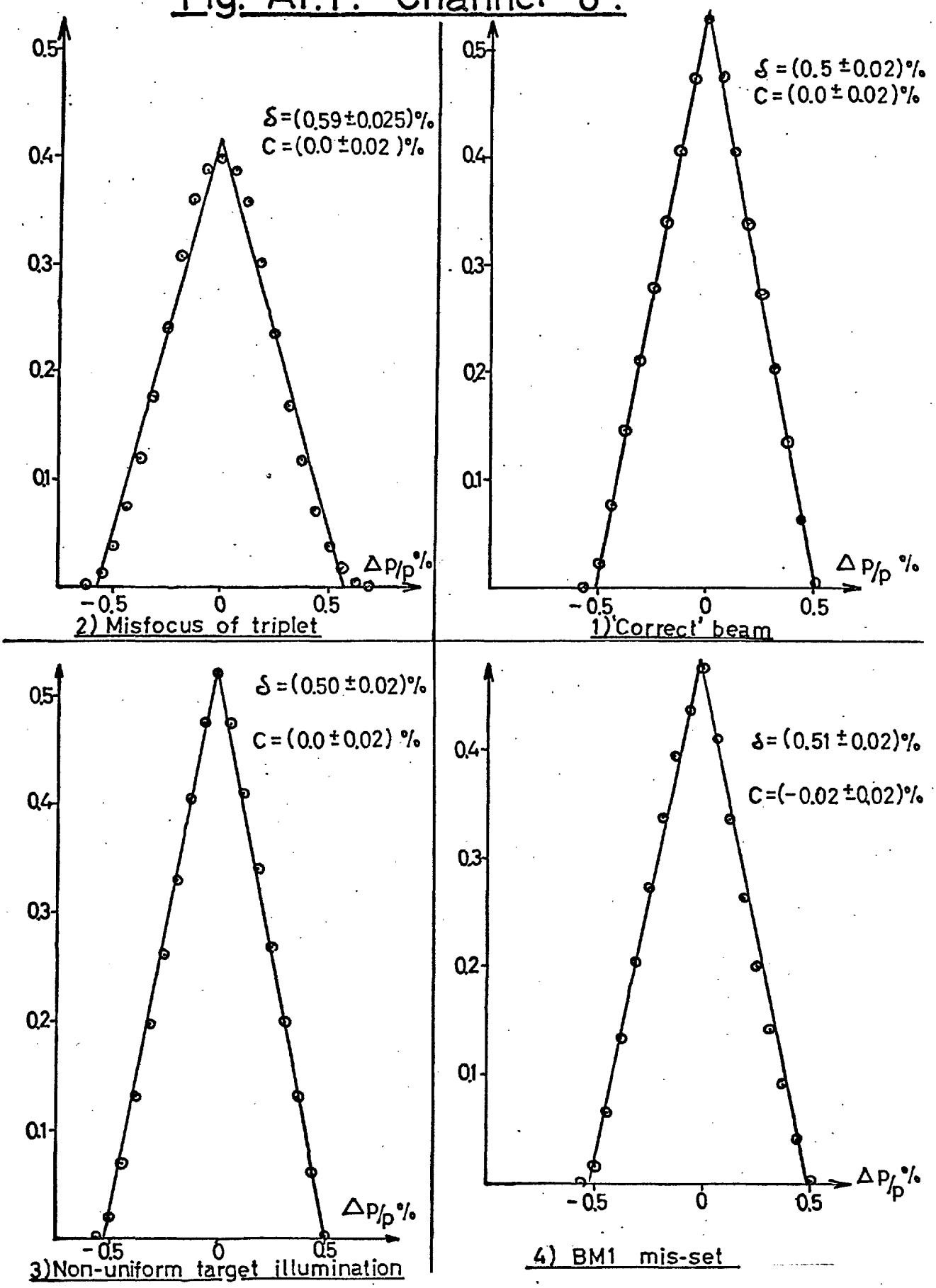

Fig. A1.2.: Channel 4

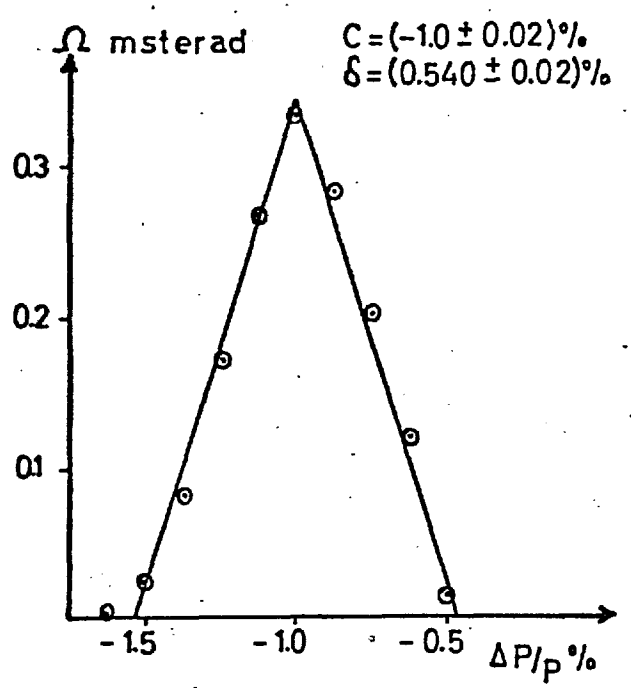

1) 'Correct' Beam

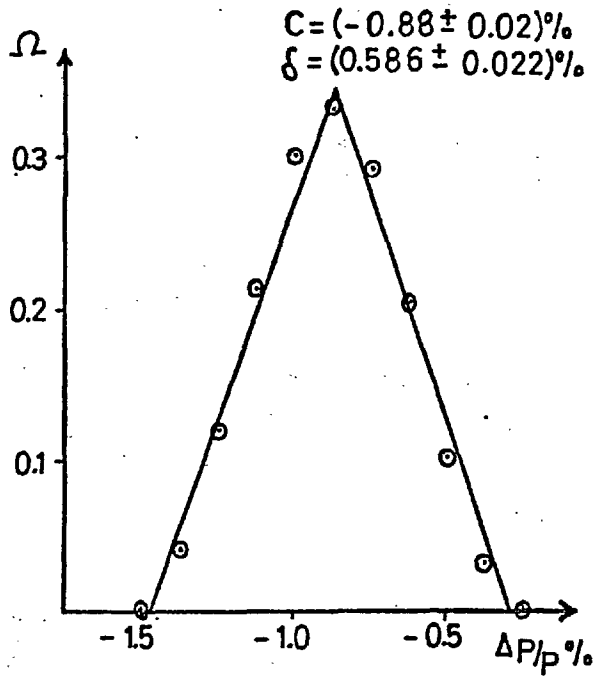

2) Misfocus of triplet

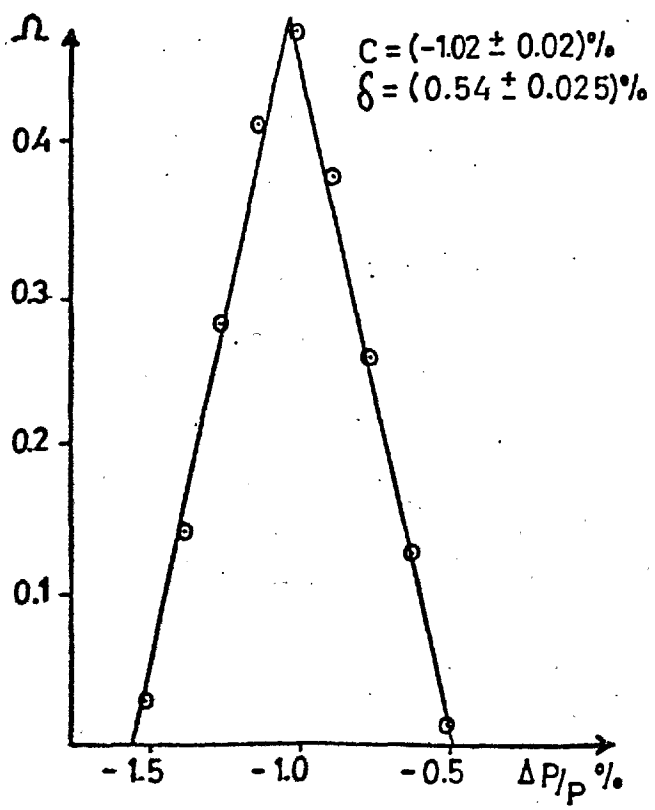

3) Non-uniform target illumination

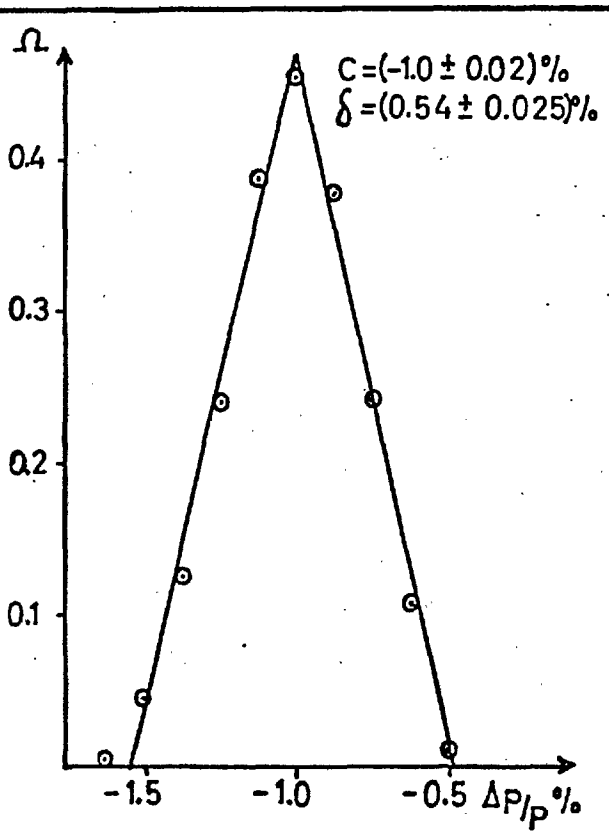

4) BM1 Mis-set

APPENDIX 2

The Method of Least Squares

This appendix describes the mathematics of the method of least squares used in the kinematic fitting programme. A more detailed account is to be found in reference (32). Matrix notations are used throughout. We first define some variables -

m = matrix of measured variables: the superscript o refers to unfitted quantities.

x = matrix of unknown variables.

$f(x,m)$ = matrix of constraint equations ($f(x,m) = 0$).

G_m^{-1} = error matrix of measured variables; $(G_m^{-1})_{ii}$ is the variance of the element m_i , and $(G_m^{-1})_{ij(i\neq j)}$ is the covariance of elements m_i and m_j .

α = matrix of Lagrangian multipliers.

f_m = $f(x,m)/\partial m$

f_x = $f(x,m)/\partial x$

The method of least squares is based on the assumption of normally distributed variables and states that the best set of variables is that for which the function

$$\chi^2 = (m - m^o)^T G_m (m - m^o) \qquad (T = \text{matrix transpose})$$

has a minimum, and where the variables fulfil the equations

$$f\ (x,m) \quad = \quad 0$$

The method of Lagrangian multipliers is usually used to perform the minimisation; the expression to be minimised is then –

$$\chi^2\ (m,x,\alpha\ ) \quad = \quad (m - m^o)^T\ G_m(m - m^o) + 2\,\alpha^T\ f(x,m) \qquad \ldots A2.1$$

which means the following set of equations has to be solved –

$$\frac{\partial\chi^2}{\partial m} \quad = \quad 2\ \left(\ (m - m^o)^T\ G_m + \quad \alpha^T\ f_m\ \right) \quad = 0 \qquad \ldots\ A2.2$$

$$\frac{\partial\chi^2}{\partial x} \quad = \quad 2\ \alpha^T\ f_x \quad = \quad 0 \qquad \ldots\ A2.3$$

$$\frac{\partial\chi^2}{\partial\alpha} \quad = \quad 2\ f\ (x,m) \quad = \quad 0 \qquad \ldots\ A2.4$$

The constraint equations are in general non-linear, so that the calculations given below must be repeated to give successively better solutions, until the equations A2.2–4 are satisfied within certain specified limits. A superscript V means that this value has been derived in the V-th iteration. Assume that we have passed the V-th iterative step and have to go at least one step more. From A2.2 we have –

$$m^{V+1} \quad = \quad m^o \quad - \quad G_m^{-1}\ f_m^{VT}\ \alpha^{\ V+1} \qquad \ldots\ A2.5$$

The constraint equations can be expanded in the following way –

$$f^V + f_m^V (m^{V+1} - m^V) + f_x^V (x^{V+1} - x^V) = 0 \qquad \ldots \text{A2.6}$$

Eliminating m^{V+1} from A2.5, A2.6, and putting

$$S = f^V_m G_m^{-1} f_m^{VT} \qquad \ldots \text{A2.7}$$

$$R = f^V + f_m^V (m^o - m^V) \qquad \ldots \text{A2.8}$$

we obtain

$$\alpha^{V+1} = S^{-1} (R + f_x^V (x^{V+1} - x^V)) \qquad \ldots \text{A2.9}$$

We introduce α^{V+1} into equation A2.3, and find

$$x^{V+1} = x^V - (f_x^{VT} S^{-1} f_x^V)^{-1} . f_x^{VT} . S^{-1} . R \qquad \ldots \text{A2.10}$$

From the new set of x^{V+1} values we calculate α^{V+1}, from A2.9, and then m^{V+1}, from A2.5. Then

$$\chi^2 = (\alpha^{V+1})^T (R + f_x (x^{V+1} - x^V)) \qquad \ldots \text{A2.11}$$

The iterative process then continues until the chosen criteria are satisfied.

Calculation of errors

From equations A2.5, A2.8, A2.9, A2.10 above, we see that m^{V+1} and x^{V+1} can be expressed as explicit functions of m^o. We can linearize these equations and write -

$$m^{V+1} = g\,(m^{o})$$
$$x^{V+1} = h\,(m^{o}) \qquad \ldots \text{ A2.12}$$

The error matrices are then obtained from the formulae -

$$G_m^{-1\ V+1} = \frac{dg}{dm^{o}}\ G_m^{-1} \left|\frac{dg}{dm^{o}}\right|^{T} \qquad \ldots \text{ A2.13}$$

$$G_x^{-1\ V+1} = \frac{dh}{dm^{o}}\ G_m^{-1} \left|\frac{dh}{dm^{o}}\right|^{T} \qquad \ldots \text{ A2.14}$$

and the correlation between measured and unmeasured variables from

$$C_{(mx)}^{V+1} = \frac{dg}{dm^{o}}\ G_m^{-1} \left|\frac{dh}{dm^{o}}\right|^{T} \qquad \ldots \text{ A2.15}$$

The two derivatives needed above, dg/dm^{o} and dh/dm^{o} are obtained in the following way -

$$\frac{dg}{dm^{o}} = 1 - G_m^{-1} f_m^{T} \frac{d\alpha}{dm^{o}}$$

$$= 1 - G^{-1}{}_m f_m^T S^{-1} \left(\frac{dR}{dm^{o}} + f_x \frac{d\,(x^{V+1} - x^{V})}{dm^{o}} \right)$$

$$= 1 - G^{-1}{}_m f_m^T S^{-1} \left(\frac{dR}{dm^{o}} - f_x\,(f_x^T S^{-1} f_x)^{-1} f_x^T S^{-1} \frac{dR}{dm^{o}} \right)$$

$$= 1 - G^{-1}{}_m f_m^T S^{-1} \left(f_m - f_x\,(f_x^T S^{-1} f_x)^{-1} f_x^T S^{-1} f_m \right) \qquad \ldots \text{ A2.16}$$

$$\frac{dh}{dm^o} = (f_x^T S^{-1} f_x)^{-1} f_x^T S^{-1} f_m \qquad \ldots \text{ A2.17}$$

Introducing these expressions into A2.13-15, and simplifying, we obtain -

$$G_m^{-1V+1} = G_m^{-1} - G_m^{-1} f_m^T S^{-1} f_m G_m^{-1} + G_m^{-1} f_m^T S^{-1} f_x (f_x S^{-1} f_x)^{-1} f_x^T S^{-1} f_m G_m^{-1} \qquad \ldots \text{ A2.18}$$

$$G_x^{-1V+1} = (f_x^T S^{-1} f_x)^{-1} \qquad \ldots \text{ A2.19}$$

$$C_{(mx)}^{V+1} = - G_m^{-1} f_m^T S^{-1} f_x (f_x^T S^{-1} f_x)^{-1} \qquad \ldots \text{ A2.20}$$

One can see from equation A2.18 that the errors in the measured quantities are reduced in the least squares solution, and that there are correlations between fitted variables even when the measured quantities are uncorrelated.

It is also worth noting that, if the matrix of corrections to the fitted variables c is introduced -

$$c^{V+1} = m^{V+1} - m^o = - G^{-1} f_m^V \alpha^{V+1}$$

we can define -

$$G_c^{-1V+1} = \frac{\partial c}{\partial m^o} G_m^{-1} \left|\frac{\partial c}{\partial m^o}\right|^T$$

$G_c^{-1}{}_{V+1}$ is the error matrix of corrections to the m_i ,

and this must satisfy the relation -

$$G_m^{-1}{}_{V+1} = G_m^{-1} - G_c^{-1}{}_{V+1} \qquad \ldots \text{A2.21}$$

ACKNOWLEDGEMENTS

I wish to thank Professor C.C. Butler for the opportunity of carrying out research as a member of the High Energy Physics group at Imperial College.

It has been a great pleasure to have had Dr. D.M. Binnie as my supervisor. His guidance and encouragement, throughout all stages of my work, is most gratefully acknowledged. I am also very largely indebted to the late Mr. J.A. Newth, for much help during the initial stages of this work.

I am extremely grateful to my colleagues Mr. A. Duane, Mr. J.P. Horsey, Dr. W.G. Jones, Mr. M.E. Kay, Mr. P.J. Nicholson, Mr. Ijaz-ur-Rahman, Dr. J. Walters, and Mr. J.G. Wilson, at Imperial College, and Professor N. Horowitz and Dr. P. Palit at the Rutherford Laboratory. Their large and essential contributions to every phase of the experiment cannot be too strongly emphasised.

I should like to thank Dr. D.A. Garbutt and Dr. D.M. Websdale for useful discussions.

Thanks are also due to Mr. R.F. Hobbs and Mr. D. Scholes for their careful construction of much of the apparatus, to Mr. D. Miller and Mr. R. Gray, and to the many people at the Rutherford Laboratory who contributed to the experiment.

For financial support during the period 1963-1966 I thank the Science Research Council.

Finally, I am indebted to Miss D. Koch for help in the preparation of this thesis.

REFERENCES

1. M.R. Jane. Ph.D. Thesis (1965).
2. F.M. Pipkin. Proc.Int.Conf.on Elem.Part., Oxford (1965).
3. G.L. Kane and R.A. Zdanis. Phys.Rev., 151, 1239 (1966).
4. The Eightfold Way. M. Gellmann and Y. Ne'eman. (1964).
5. R.F. Dashen and D.H. Sharp. Phys.Rev., 133, B1585 (1964).
6. S. Coleman and H.J. Schnitzer. Phys.Rev., 134, B863 (1964).
7. N.M. Kroll, T.D. Lee, B. Zumino. Phys.Rev., 157, 1376 (1967).
8. J.J. Sakurai. Proceedings of the 'Enrico Fermi' School at Varenna (1963).
9. E.D. Zhizkin and V.V. Solov'ev. Soviet Physics JETP., 16, 192 (1963).
10. J.B. Bronzan and F.E. Low. Phys.Rev.Letts., 12, 522 (1964).
11. W.G. Jones. Ph.D. Thesis (1966).
12. D.M. Binnie et al. Phys.Lett., 18, 348 (1965).
13. W.G. Jones et al. Phys.Lett., 23, 597 (1966).
14. B. Maglic and C. Costa. Phys.Lett., 18, 185 (1965).

    W. Kienzle et al. Phys.Lett., 19, 438 (1965).

    F. Lefelvres et al. Phys.Lett., 19, 434 (1965).

    H. Blieden et al. Phys.Lett., 19, 444 (1965).

    J. Seguinot et al. Phys.Lett., 19, 712 (1966).

    G. Chikovani et al. Phys.Lett., 22, 233 (1966).

15. R.H. Dalitz. Proc.Int.Conf.on Elem.Part., Oxford (1965).

16. V.V. Barmin et al. JETP, 45, 2082 (1963).

J.J. Murray et al. Phys.Lett., 7, 358 (1963).

A. Bezaguet et al. Phys.Lett., 12, 70 (1964).

R.A. Zdanis et al. Phys.Rev.Lett., 14, 721 (1965).

17. N. Gelfand et al. Phys.Rev.Lett., 11, 438 (1963).

18. M. Abolins et al. Phys.Rev.Lett., 11, 381 (1963).

19. L. Bertanza et al. Phys.Rev.Lett., 9, 180 (1962a).

20. P. Connolly et al. Phys.Rev.Lett., 10, 371 (1963a).

P. Schlein et al. Phys.Rev.Lett., 10, 368 (1963).

21. A.H. Rosenfeld et al. Lawrence Radiation Laboratory Report, UCRL - 8030 (rev. Jan. 1967).

22. S.L. Glashow. Phys.Rev.Lett., 11, 48 (1963).

23. A. Katz and H.J. Lipkin. Phys.Lett., 7, 44 (1963).

24. G. Alexander et al. Phys.Rev.Lett., 9, 460 (1962).

A.R. Erwin et al. Phys.Rev.Lett., 9, 34 (1962).

25. D. Whiteside. Rutherford Laboratory Report. NIRL/R/47.

26. High Energy and Nuclear Physics Handbook. Rutherford Laboratory (1962).

27. J.W. Gardner and D. Whiteside. Rutherford Laboratory Report. NIRL/M/21.

N.M. King and P.W. Simpson. Rutherford Laboratory Report. RHEL/R 103.

28. I.U. Rahman. Ph.D. Thesis (1968).

29. A.R. Faruqi. Ph.D. Thesis (1964).

30. W.P. Trower. Lawrence Radiation Laboratory Report. UCRL - 2426. Vol.II (1966 rev).

31. L.T. Kerth et al. Phys.Rev., 109, 1784 (1958).
E. Lohrmann et al. Nuovo Cimento, 7, 163 (1958).
P.B. Jones. Phys.Rev.Lett., 4, 35 (1960).
D.V. Bugg et al. Rutherford Laboratory Preprint. RPD/H/16 (1966).

32. R. Böck. CERN yellow report 60-30. (1960).
B. Ronne. Proceedings of the 1964 CERN School for physicists.

33. J.D. Jackson. Nuovo Cimento, 34, 1644 (1964).

34. H.O. Cohn et al. Nuclear Physics, B1, 57 (1967).

35. R.J. Kurtz. Lawrence Radiation Laboratory Report. UCRL-11339 (1964).

36. D.G. Crabb, J.G. McEwen, E.G. Auld, A. Langsford. Nucl. Instr.and Methods, 48, 87 (1967).

37. G. Gatti et al. Nucl.Instr.and Methods, 29, 77 (1964).

38. C.E. Wiegand et al. Rev. Sci.Instr., 33, 526 (1962).

39. H.C. Evans and E.H. Bellamy. Proc.Phys.Soc., 74, 483 (1959).

40. J.H. Atkinson et al. Phys.Rev.Lett., 2, 168 (1958).
A.E. Glassgold et al. Phys.Rev.Lett., 2, 169 (1958).

41. R.I. Hess et al. Phys.Rev.Lett., 17, 1109 (1966).

42. Y.Y. Lee et al. Phys.Rev.Lett., 11, 508 (1963).

43. M.A. Abolins et al. Proc.Int.Conf.on Elem.Part., Heidelberg (1967).

44. J.D. Jackson et al. Phys.Rev., 139, B428 (1965).

45. R. Kraemer et al. Phys.Rev., 136, B496 (1964).

46. L. Liu and P. Singer. Phys.Rev., 135, B1017 (1964).

47. T. Bacon et al. Proc.Conf.on Resonant Particles, Athens. (June 1965). p.129.

H.O. Cohn et al. Phys.Lett., 15, 344 (1965).

A. Forino et al. Phys.Lett., 19, 68 (1965).

48. G. Trilling et al. Phys.Lett., 19, 427 (1965).

49. G.F. Chew and F.E. Low. Phys.Rev., 113, 1640 (1959).

50. M. Goldhaber et al. Phys.Rev., 112, 1796 (1958).

51. D. Crennell et al. Phys.Rev.Lett., 16, 1025 (1966).

W. Beutsch et al. Proc.Int.Conf.on High Energy Phys., Berkeley. (1966).